

Development of a High Speed Solid Rotor Asynchronous Drive fed by a Frequency Converter System

Dem Fachbereich Elektrotechnik und Informationstechnik
der Technischen Universität Darmstadt
zur Erlangung des akademischen Grades eines
Doktor-Ingenieurs (Dr.-Ing.)
genehmigte Dissertation

von

Dipl. -Ing. Yoseph Gessese Mekuria
geboren am 3. April 1970 in Addis Ababa, Ethiopia

Referent: Prof. Dr.-Ing. habil. Dr.h.c. A. Binder (TU Darmstadt)

Korreferent: Prof. Dr.-Ing. Dr.-Ing. habil. S. Kulig (TU Dortmund)

Tag der Einreichung: 08.10.2012

Tag der mündlichen Prüfung: 01.02.2013

Dedication

This dissertation work is fully dedicated to my parents.

*To my mother **Abebech Tessema** and
to my father **Gessese Bekure** for their unconditional
support, encouragement and constant love throughout
all my walks of life!*

Acknowledgements

I am indebted to many people who helped me in one or other ways for the completion of this dissertation work. In the following, some of them are gratefully acknowledged.

First and foremost, I am very much grateful to my PhD academic advisor Prof. Dr.-Ing. habil. Dr.h.c. Andreas Binder for his enormous guidance, tireless consultations and supervisions during the entire work and to Prof. Dr.-Ing. Dr.-Ing. habil. Stefan Kulig for accepting to co-advise and for a very fruitful discussion we made in Dortmund. Secondly, I would like to give my gratitude to the German Catholic Academic Exchange Service (KAAD) scholarship program for financing my PhD study. I am also very thankful for *Johannes Hübner Fabrik elektrischer Maschinen GmbH*, in Gieße (Dipl.-Ing Dieter Wulkow & Dipl.-Ing Ewald Ohl) for the financial support to secure the converter system for the test bench and performing the stator windings of the prototype motors

For the realization of this project work, the help and encouragement of all current and former colleagues of the Institute for Electrical Energy Conversion, Darmstadt University of Technology, was enormous, for which I am very much grateful in deed. Saying that, I have to mention some personalities, with out them, my PhD study stay in Germany could have been difficult: Tadesse Tilahun (from Addis Ababa), Mesfin Eshetu (from Bonn), Dipl.-Theologe Mattihas Klöppinger (from KHG Darmstadt), Dr.med Denisa Ionascu (from Darmstadt), Lisa & Hartwig Looft (from Harpstedt), my sister (Alemshet) and my brothers (Ababu, Dereje and Ermias). I have to extend my gratitude to all of them.

At this very moment, I have to extend my very thanks for my lovelies: to my wife Eyerusalem (Jerry) and to our beloved kids Hasset, Kidus and Aaron for their love, encouragement and patience. They had to spend a lot of evenings and week ends without me during my intensive research work.

At the end, I would like to thank the Almighty God for giving me the endurance to realize and accomplish the dissertation work.

Yoseph Gessese

Abstract

This work deals with design, construction and testing of high speed solid rotor induction motors fed by a frequency converter system. In high speed applications, like in the compressor technology, for distributed power generators (micro gas turbines), in industry (machine power tools) and in the automotive technology (turbochargers, hybrid drives), the mechanical strength of the solid rotor induction motor (SRIM) is recognized as a significant benefit. The performance characteristics of 3-phase, 4- & 2-poles, 24000 /min, axially slitted, radially grooved solid rotor induction motors with copper end rings (*GLIDCOP AL-15*) at sinusoidal voltage supply are designed and optimized using 2D, non linear, finite element method (FEM) analysis. Although the calculation of the solid rotor is a complex three dimensional eddy current problem, the characteristics of the rotors are well estimated using 2D FEM tools. The rotor end currents and the three dimensionality of the rotor geometry are considered by equivalent end effect factors. A prototype drive system is developed and tested, which confirms the validity of the simulation results. The current harmonics, caused by the inverter supplied modulated voltage, are well damped by a low pass LC sine filter, which gives an almost sinusoidal current supply to the motor terminals. Furthermore, quantitative performance comparisons with alternative high speed motors (squirrel-cage and permanent magnet motors), which were developed and tested in previous doctoral works, have been done, showing their superior performance in higher power density and lower steady state temperature rise at the expense of a less robust rotor system.

Zusammenfassung

Diese Arbeit behandelt den Entwurf, den Bau und die Erprobung hochtouriger Massivläufer-Asynchronmotoren mit Umrichterspeisung. Im Bereich der High-Speed-Anwendungen, wie z. B. in der Kompressortechnik, bei der verteilten Energieerzeugung (Mikrogasturbinen), bei Industrieantrieben (Werkzeugmaschinen), und in der Automobiltechnik (Turbolader, Hybridantriebe) ist die mechanische Festigkeit des Massivläufers ein wesentlicher Vorteil gegenüber dem Käfigläufer-Asynchron-Motor (ASM) und dem permanenterrregten Synchron-Motor (PMSM). Ein 4- und ein 2-poliger, 3-phasiger Massivläufer-Asynchronmotor mit einer Nenndrehzahl von 24000 /min wurden in dieser Arbeit ausgelegt und erprobt. Die Massivläufer sind zum einen gekennzeichnet durch axiale Nuten und zum anderen durch radiale Rillen in der Läuferoberfläche in Verbindung mit einem massiven Kurzschlussendring aus speziellem Kupfer (*GLIDCOP AL-15*). Die analytische Auslegung wurde durch die Verwendung der nichtlinearen 2D-Finite-Element-Methode (FEM) verbessert. Da die Berechnung des Massivläufers ein komplexes dreidimensionales Wirbelstromproblem darstellt, wurde die Betriebskennlinie mit Einbeziehung eines äquivalenten Endeffekt-Faktors in der FE-Berechnung nur näherungsweise bestimmt. Der Äquivalent-Endeffekt-Faktor beschreibt den Einfluss der Querströme an den Läuferenden und den Einfluss der radialen Rillen auf die Wirbelstromverteilung. Ein Prototyp-Antriebssystem wurde entwickelt, getestet und mit Simulationsergebnissen verglichen. Die Stromüberschwingungen, bedingt durch die Umrichterspeisung, wurden durch den Einsatz eines LC- Tiefpassfilters verringert. Ein qualitativer Vergleich mit alternativen High-Speed-Antrieben (Käfigläufer-Asynchron- und permanentmagneterregtem Synchron-Motor), die in den vorangegangenen Dissertationen am Institut entwickelt worden sind, schließt diese Arbeit ab.

Motivation

In recent years, at the Institute for Electrical Energy Conversion of the Darmstadt University of Technology, several researches and dissertations [24], [33] were conducted on squirrel-cage induction and permanent magnet synchronous motors for high speed applications. Moreover, the studies were backed by experimental tests on the test bench (for 24000 /min, 30 kW). This allowed a comparison of these two types, with same constructional size and identical measuring methods, to identify their advantages and disadvantages objectively. As a continuation of these works, in this project a high speed solid rotor induction motor (SRIM), fed by a frequency converter voltage supply, has to be designed, constructed and tested at the same test bench. The main advantage of solid rotor induction motors is their robust construction; however their rotor resistance is high, which causes a poor rotor current flow. This leads to a relatively low power factor, but allows an extremely robust and rugged rotor design, which is suitable for very high speed applications. Its performance characteristics have to be compared quantitatively with the former high speed motor types computationally and experimentally in order to judge a perspective use at high speed applications.

Aufgabenstellung

Am Institut für Elektrische Energiewandlung der TU Darmstadt wurden in den letzten Jahren mehrere Dissertationen und Forschungsarbeiten [29], [40] zu Asynchronmotoren mit Käfigläufer (ASM) und permanenterregten Synchronmotoren (24000/min, 30 kW) für High-Speed-Anwendungen durchgeführt. Diese Motoren wurden auf einem Prüfstand experimentell untersucht. Dabei konnten bei gleichem Bauvolumen und identischer Messtechnik beide Konzepte verglichen sowie Vor- und Nachteile objektiv herausgestellt werden. Zur Fortführung dieser Arbeiten soll nun ein etwa baugleicher Massivläufer-Asynchronmotor (SRIM) mit Umrichterspeisung entworfen und auf demselben Prüfstand experimentell untersucht werden. Dem Vorteil der extremen Robustheit des Läufers, der eine hohe Fliehkraft und folglich eine hohe Drehzahl erlaubt, stehen die Nachteile der geringen Leistungsdichte und des geringeren Leistungsfaktors ($\cos \varphi$) gegenüber. Der geringe Leistungsfaktor ist bedingt durch den erhöhten Rotorwiderstand des Läufers und die schlechtere Stromführung im Läufer. Die Vor- und Nachteile sowie die Eigenschaften des Massivläufer-Asynchronmotors sollen mit den o.g. Motortypen rechnerisch und experimentell verglichen werden. Anhand dieses Vergleichs soll bewertet werden, ob der Einsatz der SRIM für bestimmte Hochdrehzahl-Anwendungen Perspektiven aufweist.

Contents

List of Symbols and Abbreviations.....	v
1 Introduction.....	1
1.1 Motivation and Background.....	1
1.2 Applications of High Speed Machines.....	3
1.3 Solid Rotor Constructions in High-Speed Induction Machines.....	6
1.4 Objective of the Work.....	8
1.5 Scientific Relevance of the Project.....	8
1.6 Structure of the Thesis.....	10
2 Electromagnetic Design and Analysis of a 4-pole SRIM.....	11
2.1 Electromagnetic Fields in Electrical Machines.....	11
2.2 FEM Calculation of SRIM Characteristics.....	13
2.2.1 Background.....	14
2.2.2 Field and Winding Equations.....	14
2.2.3 Finite Element Modeling.....	17
2.2.4 Rotor End Effects.....	23
2.3 Steady-State AC Magnetic Analysis.....	24
2.4 Calculation of Rotor Geometry.....	26
2.4.1 Slit-Depth Optimization.....	26
2.4.2 Slit-Width Optimization.....	30
2.4.3 End-Ring Thickness Calculation.....	33
2.5 Time Stepping (Magneto-Transient) Analysis of SRIM.....	36
2.5.1 FEM Model for Transient Analysis.....	36
2.5.2 Time Stepping Computation Results.....	36

3	Losses in Solid Rotor Machines.....	39
3.1	Electrical Losses.....	40
3.2	Magnetic Losses.....	45
3.2.1	Stator Core Losses.....	45
3.2.2	Rotor Eddy Current Losses.....	50
3.3	Rotor Radial Grooves.....	55
3.4	Rotor End-Rings Copper Losses.....	60
3.5	Mechanical Losses.....	61
3.5.1	Air Friction Losses.....	61
3.5.2	Bearing Friction Losses.....	63
4	Electromagnetic Design and Analysis of a 2-Pole SRIM.....	67
4.1	Two-pole SRIM contra 4-pole SRIM.....	67
4.2	Electromagnetic Design of a 2-pole SRIM.....	68
4.2.1	Stator Core Design.....	68
4.2.2	Stator Winding Design.....	69
4.3	FEM Computation and Analysis.....	70
4.3.1	FEM Model of 2-pole SRIM.....	70
4.3.2	Transient Simulation Results.....	71
4.4	Comparison of Computed Results of the 4- and 2-pole SRIM.....	78
4.4.1	Comparison of Simulations.....	78
4.4.2	Losses for different U/f-operations.....	82
4.4.3	Performance Characteristics of the SRIM.....	85
4.5	Comparison of Performance Characteristics of High Speed Machines.....	90

5	Construction of Prototype Solid Rotor Motors.....	93
5.1	Stator Construction.....	93
5.1.1	Stator Frame.....	94
5.1.2	Stator Core.....	94
5.2	Stator Windings Design and Construction.....	96
5.3	Solid Rotor Technology.....	101
5.3.1	Rotor Core Material.....	103
5.3.2	Rotor End-Rings.....	105
5.3.3	Rotor Balancing and Over-speed Test.....	108
5.4	Rotor Temperature Measurement Setup.....	109
5.5	High Speed Spindle Bearings.....	111
6	Testing of Solid Rotor Prototype Motors.....	113
6.1	Test Bench Overview.....	113
6.2	Converter System Voltage Supply.....	115
6.3	LC- Sine Filter.....	119
6.4	Test Results.....	124
6.4.1	Four-pole Motor Test Results.....	125
6.4.2	Two-pole Motor Test Results.....	130
6.5	Comparisons of Results.....	139
6.5.1	Comparison of 4- and 2-pole Motors Test Results.....	140
6.5.2	Comparison of Measured and Calculated Results.....	143

7 Conclusions and Recommendations.....	147
Appendix	149
Appendix A: Stator Frame and Stator Core Details.....	149
Appendix B: Rotor Constructions.....	152
Appendix C: Torque Sensor.....	153
References.....	157

Applied Symbols and Abbreviations

a	-	number of parallel paths
a_T	-	wire numbers lying side by side in a slot width
\bar{A}	Vs/m	magnetic vector potential
A	A/m	current layer
A	m ²	area
b_b	m	bearing width
b_Q	m	slot width
b_{sh}	m	iron sheet thickness
b_T	m	equivalent conductor width
\bar{B}	T	magnetic flux density
B_δ	T	air-gap magnetic flux density
c_f	-	friction coefficient
C_0	N	bearing static load
C_f	F	filter capacitance
C_T	-	torque coefficient
d_b	m	bearing diameter
d_E	m	penetration depth
d_{ri}	m	inner rotor diameter
d_{ra}	m	outer rotor diameter
d_{si}	m	inner stator diameter
d_{sa}	m	outer stator diameter
\bar{D}	As/m ²	electric flux density
\bar{E}	V/m	electric field strength
\bar{e}_z	-	unit vector in z -direction

f	Hz	electric frequency
f_T	Hz	switching frequency
f_{res}	Hz	resonance frequency
F	N	force
F_a	N	axial bearing load
F_r	N	radial bearing load
g	-	integer number for calculation of ordinal numbers
h	m	height
h_L	m	conductor height
\vec{H}	A/m	magnetic field strength
i	A	electric current
I	A	electric current (RMS)
j	-	imaginary unit $\sqrt{-1}$
\vec{J}	A/mm ²	electric current density
k_1	-	rotor roughness coefficient
k_d	-	distribution factor
k_e	-	General equivalent end effect factor
k_p	-	pitch factor
k_w	-	winding factor
k_h	$\frac{\text{W.s}}{\text{T}^2 \cdot \text{m}^3}$	hysteresis loss coefficient
k_{ex}	$\frac{\text{W}}{\text{m}^3} \cdot \left(\frac{\text{T}}{\text{S}}\right)^{1.5}$	excess loss coefficient
k_{Fe}	-	iron stack fill factor
$k_{\text{Fe}}, k_{\text{Hy}}$	-	iron loss factors
$k_{\text{R}, \nu=1}$	-	<i>Russell</i> end-effect factor for fundamental field
$k_{\text{R}, \nu}$	-	<i>Russell</i> end-effect factor for harmonic field

l	m	axial length
L	H	self inductance
L_f	H	filter inductance
L_{ew}	H	end-winding self inductance
L	m	overall length
m	-	number of phases
m	kg	mass
m_T	-	number of coil sides one over the other in a slot height
M	Nm	torque
M	H	mutual inductance
M_{em}	Nm	electromagnetic torque
M_s	Nm	shaft torque
n	1/s	rotational speed
N_c	-	number of turns per coil
N_s	-	number of turns per phase
p	-	number of pole pairs
p	W/m ³	power density
P	W	power
$P_{Cu,Ft,a}$	W	current displacement loss (2 nd order)
$P_{Cu,Ft,b}$	W	current displacement loss (1 st order)
P_δ	W	air-gap power
q	-	number of slots per pole and phase
Q	-	number of slots
R	Ω	electric resistance
R_{20°	Ω	electric resistance at 20 °C
R_e	-	<i>Reynolds</i> number
s	-	slip
s_Q	m	slot opening

t	s	time
T	s	time period
u	V	time variable electric voltage
U	V	electric voltage (RMS)
v	m/s	velocity
V	A	magnetic voltage (magneto-motive force), MMF
V	m ³	volume
W_{co}	J	magnetic co-energy
x	m	circumference co-ordinate
X	Ω	reactance
z	-	total number of conductors
Z	Ω	impedance
δ	m	air-gap width
ε	As/(Vm)	permittivity
ε	K ⁻¹	temperature coefficient of resistance of rotor core material
φ	rad	phase angle
κ	S/m	electric conductivity
μ	-	ordinal number of rotor space harmonic
μ	Vs/(Am)	magnetic permeability
μ_r	-	magnetic relative permeability
μ_0	Vs/(Am)	magnetic permeability of free space ($4 \cdot \pi \cdot 10^{-7}$ Vs/(Am))
ρ	Ωm	resistivity
ρ	kg/m ³	material mass density
ν	-	ordinal number of stator space harmonic
ξ	-	'reduced' conductor height
η	-	efficiency
ϑ	°C	temperature
θ	°	mechanical degrees
σ_t	N/m ²	tangential stress

τ_Q	m	slot pitch
τ_p	m	pole pitch
τ_s	N/m ²	shear stress
ϕ	V	electric scalar potential
ψ	Wb	magnetic flux linkage
ω	1/s	electric angular frequency
ω_m	1/s	mechanical angular frequency
Ω	1/s	electric angular speed
Ω_m	1/s	mechanical angular speed

Subscripts

a	outer
ad	additional
av	average
amb	ambient
b	winding overhang (<i>bobinage</i>)
Cu	copper
d	dissipation, dental (tooth)
el	electric
e	electromagnetic
Fe	iron
fr	friction
Ft	<i>Foucault</i> losses (eddy current losses)
h	main
HO1	Harmonic order 1 (fundamental harmonic)
Hy	hysteresis
i	inner
in	input
m	mechanical, magnetising
mag	magnetic

max	maximum
N	nominal
out	output
p	pole, pitch
puls	pulsation
ph	phase value
Q	slot
r	rotor
s	stator, shaft
sh	sheet
syn	synchronous
Y	yoke
w	windage
∞	infinite
δ	air gap
σ	leakage
Y	star connection

Abbreviations

SRIM	Solid Rotor Induction Motor
PMSM	Permanent Magnet Synchronous Machine
ASM	Asynchronous Machine
PWM	Pulse Width Modulation
MOSFET	Metal-Oxide-Silicon Field-Effect-Transistor
IGBT	Insulated Gate Bipolar Transistor

1 Introduction

1.1 Motivation and Background

In many manufacturing, transportation and process industries the technology advancement is often closely associated with an increase in optimal speed of operation. In this regard, high speed direct (gearless) electrical drives are becoming very popular due to the reduction of the drive constructional volume for a given power. To achieve a high speed performance, high frequency operated machines are always the preferable choice. High frequency of the input current reduces the constructional volume of the electrical machines, as the developed electromagnetic torque, which determines the size, is proportional to the air gap power and the number of poles and inversely proportional to the frequency [37].

In recent years, the remarkable development of relatively cost effective, fast switching and compact frequency converters with a high rated power up to 1MW with an output operating frequency of 1-2 kHz opens the dynamic worldwide market for high speed drives [1], [25], [42].

Due to brush contact and commutator segments related mechanical problems, dc drives are less suitable for high speed applications. First of all, brush wear at high speed becomes very high and it adversely affects the commutation process. Secondly, the structure is not favourable for large centrifugal stresses. But, as high speed drives there are different types of ac motor concepts [30]: Laminated/solid asynchronous, permanent magnet synchronous, homopolar synchronous and switched reluctance synchronous motors.

Laminated squirrel-cage / Solid rotor -asynchronous motors: These motors are able to operate in the field weakening control easily at constant power operation, so the inverter power can be limited.

Permanent magnet synchronous motors (PMSM): With the excitation nature of the rotor field “without current”, it is possible to minimize additional rotor losses which are relatively high in high speed applications. In surface mounted magnet constructions, the carbon fiber is needed in order to fix the magnets which reduces its mechanical strength. In rotors, with buried construction, the magnets are fixed by themselves in the rotor cores. Field weakening is easier in these rotor types than that of the surface mounted types but the mechanical strength of the iron wedges is often lower than that of the carbon fiber which makes them not so useful for high speed applications [12].

Homo-polar synchronous motors: These motors allow a variable dc excitation in the stator winding and hence field weakening is easy to accomplish. The construction of the rotor without winding makes it very robust, but generally its electromagnetic utilization is less than that of the other motor types.

Switched reluctance motors: These motors are also having a robust no-winding rotor construction and best field weakening possibilities. However, a special inverter is needed for their operation. Like homo-polar synchronous motors, their rotor is constructed as “gear” so that it reacts against the pump-effect friction at high rotational speeds.

Solid rotor induction motors (SRIM), as the name implies, are of unconventional construction, having a massive rotor machined from a round iron bar, and are mechanically very robust. However, the electromagnetic properties of such rotors are poor, as the operating slip of the rotor tends to be large, which increases the rotor losses and results in a lower power factor, whereas permanent magnet synchronous machines (PMSM) offer better efficiency and a higher torque density

[8], [33]. On the other hand, the solid rotor is very rugged and can be operated without a speed sensor. The simplest solid rotor is a smooth steel cylinder, which is easy to manufacture and has the best mechanical and fluid-dynamical properties for low air friction [59], [60], [61]. The torque of the solid rotor induction motor can be increased by copper end-rings, as the rotor current flow in the solid iron then tends to be more aligned into the axis-parallel direction, which increases the *Lorentz* force. According to [25], a two pole smooth solid rotor equipped with copper end-rings produces twice as much torque at a certain slip as the same rotor without end-rings. A further performance improvement is achieved by axially slitting the cross-section of the rotor in such a way that a better flux penetration into the rotor is enabled [17], [18], [43]. Slitting the rotor decreases the low frequency impedance of the rotor, thus producing more torque at a very low slip, but less torque at a higher slip [64]. It increases the high-frequency surface impedance of the rotor, thereby decreasing the rotor eddy current losses due to stator slotting and inverter current ripples. The disadvantage of the axial slitting is that the ruggedness of the solid rotor is partly lost, and at very high speed the friction between the rotating rotor and the air increases remarkably. On the other hand the slitting intensifies the cooling of the rotor thanks to the increased cooling surface of the rotor [47]. The other possibility of reducing the rotor eddy current losses, which cause a sharp temperature rise, is making thin radial grooves on the rotor surfaces and thereby cutting the path of high frequency rotor harmonic currents [28], [40], [67].

1.2 Applications of High Speed Machines

Nowadays, high speed direct drives with a speed range between 20000 min^{-1} and 60000 min^{-1} at a power class of between 30-100 kW are intensively used, where the high rotational speed gives an advantage for the working machine to improve the work process as explained in the following applications:

Compressors, pumps and fans: Resulting in small dimension of the compressor wheels and the driven system. Typical speeds range between $40000 \dots 60000 \text{ min}^{-1}$

at a power of 50 to 500 kW and give a better operating performance, as illustrated in Fig. 1.1 [2], [8].

Lath, turning and milling machines: They enable the process to be done at high speeds (High-Speed-Cutting), which allows an improved cutting quality with minimum processing time. Typical speeds of 15000...80000 min^{-1} at a typical cutting power of 100 kW are required.

Starting generators in air-craft engines: Optimal adjustment of the machine speed is possible with the speed of the engine.

Exhaust gas turbochargers: The replacement of the turbine is possible with a high efficiency high-speed motor.

Micro-gas turbines: These are currently taken as intensive decentralized energy supply systems, where the high turbine speed requires a special high speed generator [3], [12], [36].

For all these applications no gear-box is necessary between the motor and the working machine, when a high speed drive is used. Thus, it is possible to avoid gearbox noise, maintenance work for oil lubrication, mechanical wear of the gears and the cost of the gearbox itself. Furthermore the complete drive unit can be designed to result in a smaller size, because not only the gearbox is missing, but also the coupling is avoided. The motor itself at high speed and given power is much smaller than a low speed machine, resulting in a very compact drive system [32].

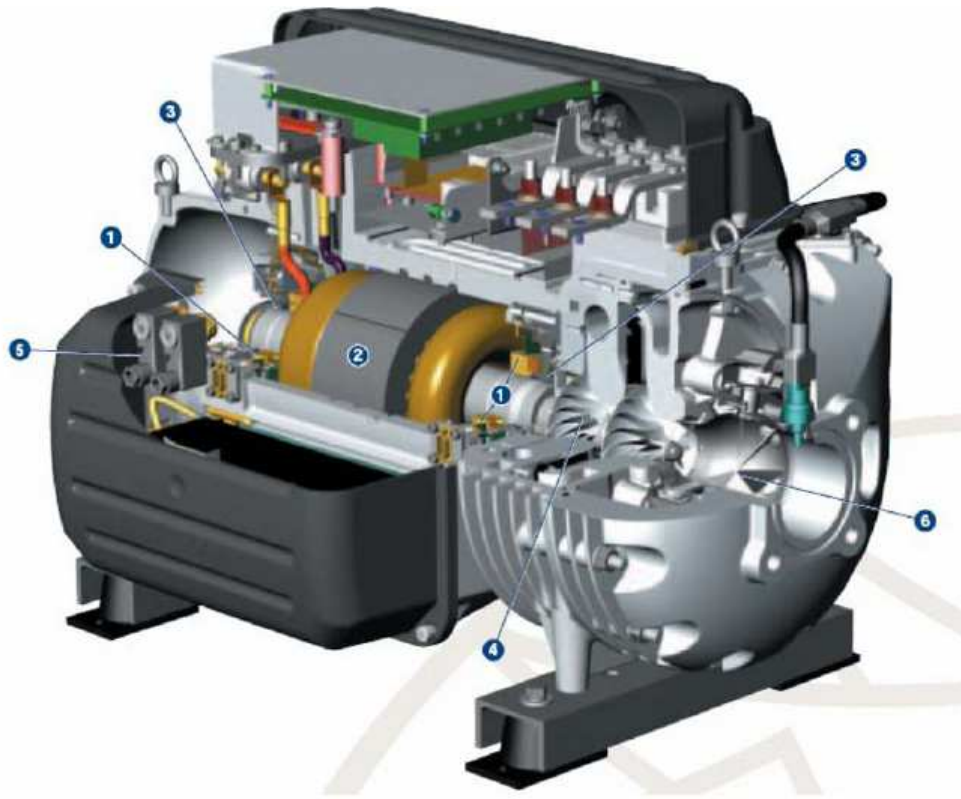


Figure 1.1: High speed compressor with PM motor: 1- magnetic bearing, 2- PM motor, 3- touchdown bearing (when the compressor is not energized), 4- shaft and impellers, 5- compressor cooling, 6- inlet guide vane assembly. *Source: Danfoss Turbocor Compressors*

The main advantages of high speed drives are summarized as follows:

- No gear box: Elimination of the gearbox costs, no oil leakage or oil changes, no wear operation, elimination of the gearbox losses, lower noise and higher overloading capability,
- Small motor size: High power output can be achieved even with small torque, using high speed operation. Since the torque determines the motor size, a relatively small motor can be used still to attain for high power output ("Power from speed"), which leads to a compact construction.

- Possibility to design integrated drives: The compact, volume-saving design facilitates an integration of the motor with the working machine. This is supported by reduced components (no gear) and allows saving of the masses of the couplings. The integration of the drive itself creates new design scope possibilities for mechanical engineering.
- Increased dynamic performance: The elimination of mechanical couplings creates a rigid mechanical drive, which in turn enables a better controllability (dynamic control).

1.3 Solid Rotor Constructions in High Speed Induction Machines

Solid-rotor induction motors are built with the rotor made of a single piece of ferromagnetic material. For high speed application, centrifugal forces play an important role to decide the construction type. The rotor should have sufficient strength to withstand these forces. The spatial air-gap field and PWM inverter time harmonics cause increased vibrations and noise.

A solid rotor with smooth homogeneous surface offers the best solution to minimize parasitic effects of mechanical nature, but has the worst electromagnetic output characteristics. Practically, solid rotors are constructed in one of the following ways as illustrated in Fig. 1.2 [25], [32], [55]. In this work, the axially slitted homogeneous solid rotor induction motor with copper end-rings (Fig.1.2c) is considered and studied extensively.

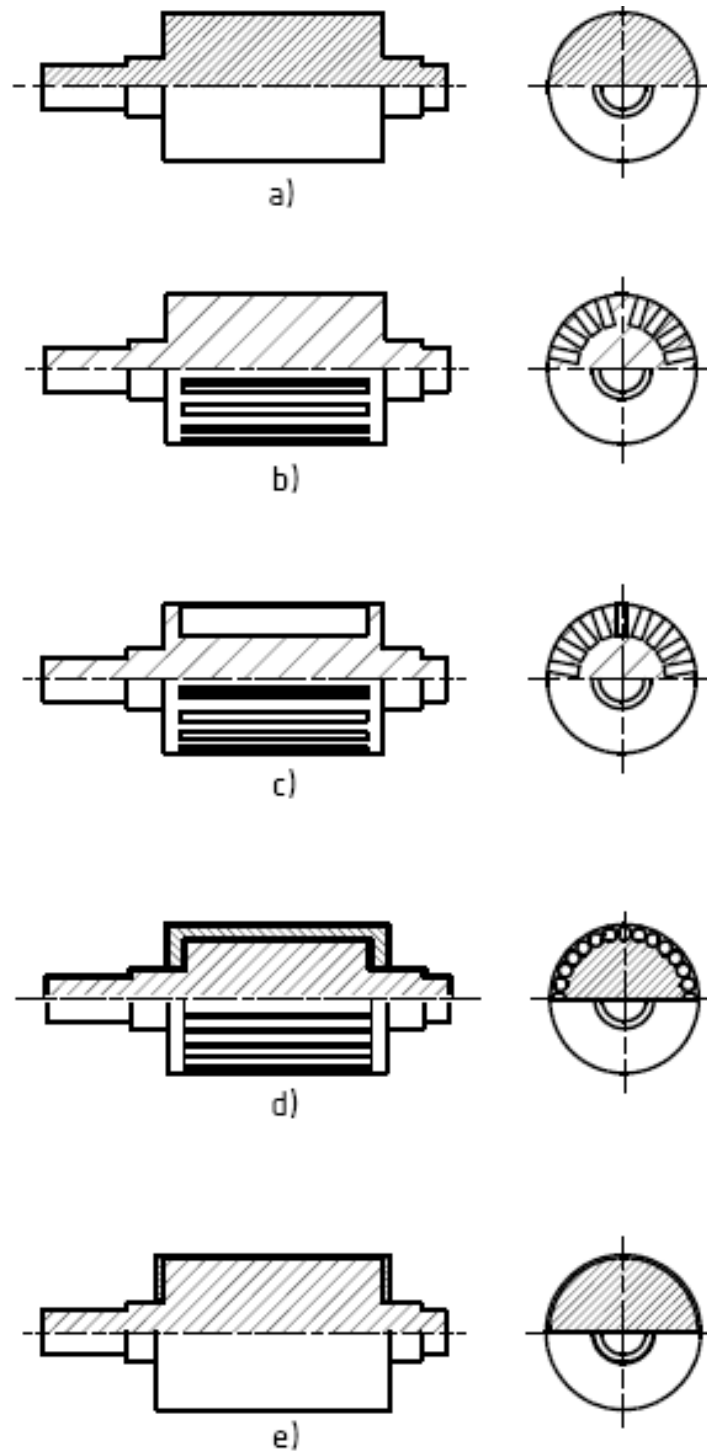


Figure 1.2: Solid-rotor constructions: a) smooth solid rotor, b) slitted solid rotor, c) slitted solid rotor with end rings, d) squirrel-cage solid rotor, and e) coated smooth solid rotor [25], [55].

1.4 Objective of the Work

This project work has the following objectives:

- To design and compute high speed solid rotor induction motors numerically, using a 2D FEM tool.
- To optimize the rotor geometry and find the solution, which results in relatively minimum rotor eddy current losses, which affects the rotor heating.
- To construct and test a prototype solid rotor asynchronous drive with a frequency converter system to validate the simulation results.
- To quantitatively compare the performance characteristics of the solid rotor with the already available results of high speed squirrel cage and permanent magnet synchronous motors of Table 1.1.

1.5 Scientific Relevance of the Project

Solid rotors are challenging electric energy converters to model and solve mathematically. The non-linear material magnetization characteristic of the iron core and the three dimensional (3D) distribution of the rotor currents make the analytical approach complicated and hence can be done only approximately [14], [15]. The establishment of eddy currents in the moving rotor parts can be estimated well numerically in 3D simulation with a complex calculation and higher computation time. In addition, the stator air-gap field, which causes the rotor eddy currents, has a non-sinusoidal space distribution because of the slot openings, which results in additional rotor harmonic currents. These harmonic currents are not involved in the production of the driving electromagnetic torque, but rather cause additional rotor eddy current losses, which adversely affect the rotor heating. Due to

the skin effect the penetration depth of the currents is low, and the apparent rotor resistance is high. The increase in rotor resistance decreases the output torque at a given slip. Here, by optimizing the rotor geometry and its cooling condition a possible optimized solution can be investigated. Similarly, by using the copper end rings, it is possible to influence the distribution of the rotor currents to be more axial, which increases the motor torque at a given slip. All these optimizations require a substantial sum of calculations numerically, using the Finite Element Method (FEM) [23], [62]. With inverter operation the current higher harmonic ripple in the stator windings causes additional eddy current losses also in the rotor via the fluctuating air-gap field. This ripple can be damped by using a low pass sinusoidal *LC*-filter as in [21], [54].

Table 1.1: Output performance parameters of high speed squirrel cage and permanent magnet synchronous motors [29], [40]

Motor	Asynchronous with squirrel cage rotor	PM Synchronous, $\text{Sm}_2\text{Co}_{17}$ -magnets
Rated voltage	330 V	311 V
Rated current	72.8 A	62.2 A
Rated power factor	0.77	0.95
Rated frequency	800 Hz	800 Hz
Connection of stator winding	Y	Y
Rated speed	23821 /min	24000 /min
Rated slip	0.008	0
Rated output power	30 kW	30 kW
Efficiency	93.7 %	95.1%

1.6 Structure of the Thesis

In the thesis, 4- & 2-pole axially slitted, radially grooved solid rotor induction motors with copper end rings are analysed, constructed and tested in order to devise the perspective implementation for high speed applications.

Chapter 2 describes the Finite Element Method (FEM) design and analysis of the high speed 4-pole solid rotor induction motor, where the machine geometrical parameters are optimized and performance characteristics are calculated numerically. Chapter 3 deals with the description of various losses that occur in solid rotor induction motors at high speed operation. Furthermore, methods of minimizing the losses are explained, which were applied in the analysed motor. Chapter 4 explains the electromagnetic design and analysis of a 2-pole high speed solid rotor induction motor as a better candidate for high speed performance. Chapter 5 is dedicated to explain the constructing technology of the motors i.e. stator core, cooling system, stator windings, rotor core, axial slits, radial grooves and end rings. The mechanical capability of the rotor material is checked numerically and analytically. Chapter 6 shows the test results of the motors and comparisons with the simulation results for validation. In addition, the comparison with the existing high speed machines of the same constructional volume at the *Institute of Electrical Energy Conversion, Darmstadt University of Technology* is presented.

Finally, the conclusions and the possible recommendations of the thesis are presented in Chapter 7.

2 Electromagnetic Design and Analysis of a 4-pole SRIM

In the numerical design and analysis of an electrical machine using a Finite Element Method (FEM) with impressed currents, the magnetic field is excited by the current in the exciting coils. However, in this study the coupling circuit is modelled as a voltage source, which leads to the combined solution of the field and circuit equations.

2.1 Electromagnetic Fields in Electrical Machines

The electromagnetic phenomena in rotating electrical machines rely fundamentally on the four *Maxwell's* equations.

$$\nabla \times \vec{H} = \vec{J} + \frac{\partial \vec{D}}{\partial t} \quad (2.1)$$

$$\nabla \times \vec{E} = -\frac{\partial \vec{B}}{\partial t} \quad (2.2)$$

$$\nabla \cdot \vec{B} = 0 \quad (2.3)$$

$$\nabla \cdot \vec{D} = \rho \quad (2.4)$$

In the magneto-quasistatic condition, which is also the case of electrical machines, where fields are varying slowly with time, the displacement currents $\partial \vec{D} / \partial t$ are neglected as in (2.5) [40].

$$\nabla \times \vec{H} = \vec{J} \quad (2.5)$$

The constituent relations, which depend on the electromagnetic medium (materials),

are given below:

$$\vec{J} = \kappa \cdot \vec{E}, \quad (2.6)$$

$$\vec{B} = \mu \cdot \vec{H}, \quad (2.7)$$

$$\vec{D} = \varepsilon \cdot \vec{E}, \quad (2.8)$$

where μ is the magnetic permeability, ε is the permittivity and κ is the electrical conductivity of the materials. The conductors are assumed to be isotropic with a constant electric conductivity, whereas $\mu = \mu(H)$ describes the assumed isotropic magnetic non-linearity of ferromagnetic mediums. *Ampere's* law states that the magnetic field strength H is related to the electrical current density J and the changing of the electric flux density $\partial \vec{D} / \partial t$ (2.1). *Faraday's* law of electromagnetic induction shows the connection between the electric field strength E and the varying magnetic flux density B (2.2).

The electric field \vec{E} is expressed in electrostatic arrangements as the gradient of a scalar potential function as

$$\vec{E} = -\nabla \phi, \quad (2.9)$$

but in coupled electromagnetic problem it is given by (2.12), because there is no general scalar potential for the magnetic field \vec{B} . It can be expressed as a *Curl* vector function as in (2.10).

$$\vec{B} = \nabla \times \vec{A} \quad (2.10)$$

The function \vec{A} is known as the 'magnetic vector potential'. In case of the quasi-static field problems, the divergence of the magnetic vector potential is often put to zero everywhere in the space studied, which is called *Coulomb's gauge* condition.

$$\nabla \cdot \vec{A} = 0 \quad (2.11)$$

2.2 FEM Calculation of SRIM Characteristics

In this section, a 4-pole axially slitted solid rotor induction motor with rotor copper end rings is calculated numerically, using a 2D FEM analysis [65]. The basic design data of the motor are given in Table. 2.1. The stator core and slot geometry are adopted from the previous built reference high speed squirrel cage induction and permanent magnet synchronous machines [24], [33] as shown on the Fig (2.1). The integer slot winding with $q=3$ slots per pole per phase has for parallel branches $a=4$. It has a two-layer winding. All four poles of the stator winding are connected in parallel giving with $N_c=8$ turns per coil $N_s = 2p \cdot q \cdot N_c / a = 4 \cdot 3 \cdot 8 / 4 = 24$ turns per phase. By having the maximum possible number of parallel branches $a=4$, the number of turns per coil $N_c=8$ is also maximum, yielding the minimum cross section area of the coil conductors to minimize current displacement effects in the stator winding due the higher stator frequency of 800 Hz for 24000 min^{-1} at $2p=4$.

Table 2.1: Basic Design Data of a 30 kW SRIM, 330V, Y

Machine	$2p = 4$
Stator frequency (Hz)	800
Stator outer / inner diameter (mm)	150 / 90
Air gap / stator slot opening (mm)	0.6 / 2.3
Stack length (mm)	90
Number of stator slots / rotor slits	36 / 28
Stator turns per coil / turns per phase	8 / 24

2.2.1 Background

The basic design and performance characteristics of induction machines are normally calculated analytically, using an equivalent circuit approach with some approximate adjustments to circuit parameters to allow the consideration of saturation.

The method satisfies for steady-state operation at the low slip operating region for classical squirrel cage or wound rotor induction motors, supplied by a pure sinusoidal voltage. But it is not directly applicable to the analysis of inverter fed high speed solid rotor induction motors, which have no windings on the rotor. In this type of motors the rotor impedance parameters are highly depending on the real field distribution at the given operating slip [35]. The rotor induced eddy currents, which are necessary for the production of the electromagnetic torque, are three-dimensionally distributed in the core [50]. Hence, in order to predict the performance characteristics of solid rotor induction motors with a better accuracy, it is necessary to use the numerical finite element method [19], [23], [39], [49].

2.2.2 Field and Winding Equations

Using the magnetic vector potential A , the electric potential ϕ and *Maxwell's* equations (2.1), (2.5), it is obtained that

$$\vec{E} = -\frac{\partial \bar{A}}{\partial t} - \nabla \phi \quad (2.12)$$

$$\vec{J} = \nabla \times \left(\frac{1}{\mu} \nabla \times \bar{A} \right) \quad (2.13)$$

Since $\nabla \times \nabla \phi = 0$, adding a scalar potential as expressed in (2.12), does not affect the induction law (2.2).

The current density, which depends on the electric field strength, is given by:

$$\vec{J} = \kappa \cdot \vec{E} = -\kappa \cdot \frac{\partial \vec{A}}{\partial t} - \kappa \cdot \nabla \phi \quad (2.14)$$

Then substituting expression (2.14) in (2.13) gives:

$$\nabla \times \left(\frac{1}{\mu} \nabla \times \vec{A} \right) + \kappa \cdot \frac{\partial \vec{A}}{\partial t} + \kappa \cdot \nabla \phi = 0 \quad (2.15)$$

Equation (2.13) is valid in the areas, where the source current is applied such as stator coil currents, whereas equation (2.14) is valid in the eddy current region, which is the case of the rotor of a solid rotor induction machine. But the eddy currents in the stator windings and in the laminated stator cores are ignored by this approach. The conductivity of the iron lamination sections is set to zero. The total resistance of the windings is given through the coupled circuit, that is, only the resistive voltage drop of the stator windings is taken into consideration in the analysis. The non-rotational part of the electric field strength is described by the scalar potential ϕ (2.9). It is due to the electric charges and polarisation of dielectric materials. The iron hysteresis effect in the stator and rotor core is also not considered in the analysis.

In a two-dimensional FEM calculation, the solution is based on one single axial component of the vector potential A_z . The axial coordinate is chosen to be the z -axis. Hence, the field solution (B, H) is found on the x - y -*Cartesian* plane, while \vec{J} , \vec{A} , and \vec{E} have only a z -component, ($\vec{E} = (0, 0, E_z)$) as in (2.16).

$$\nabla \times (\nabla \times \vec{A}_z) = -\mu \cdot \kappa \cdot \frac{\partial \vec{A}_z}{\partial t} - \mu \cdot \kappa \cdot \nabla \phi \quad (2.16)$$

$$\nabla^2 A_z = \mu \cdot \kappa \cdot \frac{\partial A_z}{\partial t} + \mu \cdot \kappa \cdot \frac{\partial \phi}{\partial z} \quad (2.17)$$

$$\frac{\partial^2 A_z}{\partial x^2} + \frac{\partial^2 A_z}{\partial y^2} = \mu \cdot \kappa \cdot \frac{\partial A_z}{\partial t} + \mu \cdot \kappa \cdot \frac{\partial \phi}{\partial z} \quad (2.18)$$

Therefore, the magnetic vector potential and current density vectors can be expressed as

$$\vec{A} = A_z(x, y, t) \vec{e}_z, \quad (2.19)$$

$$\vec{J} = J_z(x, y, t) \vec{e}_z, \quad (2.20)$$

where x and y are the *Cartesian* plane coordinate components and \vec{e}_z is the unit vector in the z -axis. When a two-dimensional model is used to calculate a straight conductor of the length l , the scalar potential difference between the ends of the conductor is given by (2.21).

$$u = \int -\nabla \phi \cdot d\vec{l} = \int +\vec{E} \cdot d\vec{l} \quad (2.21)$$

To reduce the number of field equations to be solved, the conductors inside the stator slots due to the turns per slot $2 \times N_c$ for a double layer, winding are simplified and modelled as a single solid conductor per layer, as it is assumed in [7]. The conducting region is assumed to form a straight conductor along the axial length, which is the same as the core length. Hence substituting (2.21) in (2.18), it is obtained that:

$$\frac{\partial^2 A_z}{\partial x^2} + \frac{\partial^2 A_z}{\partial y^2} = \mu \cdot \kappa \cdot \frac{\partial A_z}{\partial t} + \mu \cdot \kappa \cdot \frac{u}{l}. \quad (2.22)$$

The machine supply voltage u , which must be coupled with the field equation (2.23), is expressed as:

$$u = Ri + L_{ew} \frac{di}{dt} + \frac{d\psi}{dt}, \quad (2.23)$$

where u and i are the voltage and current of the stator winding per phase, R is the resistance of the winding per phase, ψ is the stator winding flux linkage per-phase, and L_{ew} is the end winding inductance representing the end winding flux linkage, which is not included in ψ . The rotor of the machine, which is made from a relatively pure iron, is modelled as a solid conductive iron with a non-linear magnetisation curve shown on Fig. 2.4. In order to model the rotor eddy currents, the current density is given by (2.14), where the gradient of the electric scalar potential is zero. The electromagnetic torque between the rotor and the stator of the machine is calculated in the simulation by the virtual work method. This allows computing the torque exerted on parts that keep their shape and that are surrounded by air [13], [46]. According to the reports by [7], [56], the virtual work method has shown to give reliable results, when computing the air-gap torques of rotating electric machines. In this method the torque is calculated as a partial differential of the magnetic co-energy W_{co} with respect to the virtual angular displacement θ as in (2.24).

$$M = \frac{\partial W_{co}}{\partial \theta} = \frac{\partial}{\partial \theta} \int_V \int_0^H B dH dV \quad (2.24)$$

2.2.3 Finite Element Modelling

For the electromagnetic calculation, the FEM program FLUX-2DTM software package from CEDRAT is used. The machine rotor parameters are calculated and

optimized, using a 2D FEM steady state AC magnetic analysis, where the field components are assumed to change in time sinusoidally. The losses and the performance characteristics of the solid rotor induction motor were evaluated, using a two dimensional, non-linear, time stepping finite element analysis of the magnetic field, i.e. magnetic iron saturation, skin effect in the rotor and movement of the rotor with respect to the stator were taken into account [4], [5], [13], [39].

Table 2.2: Axially slitted massive rotor parameters of the four pole motor

Parameter	value
Rotor outer diameter (mm)	89.2
Radial air gap width (mm)	0.4
Slit width / slit depth (mm)	2.5 / 13

The machine stator geometry is given in Fig. 2.1. The initial rotor parameters (Table 2.2) are used to design the 4-pole FE computing model Fig. 2.2a. Since the machine is symmetrical with respect to the pole axis, it was sufficient to model and compute the field per pole. Accordingly, anti-periodic boundary conditions are used on the sides of a solution section to consider north and neighbouring south poles.

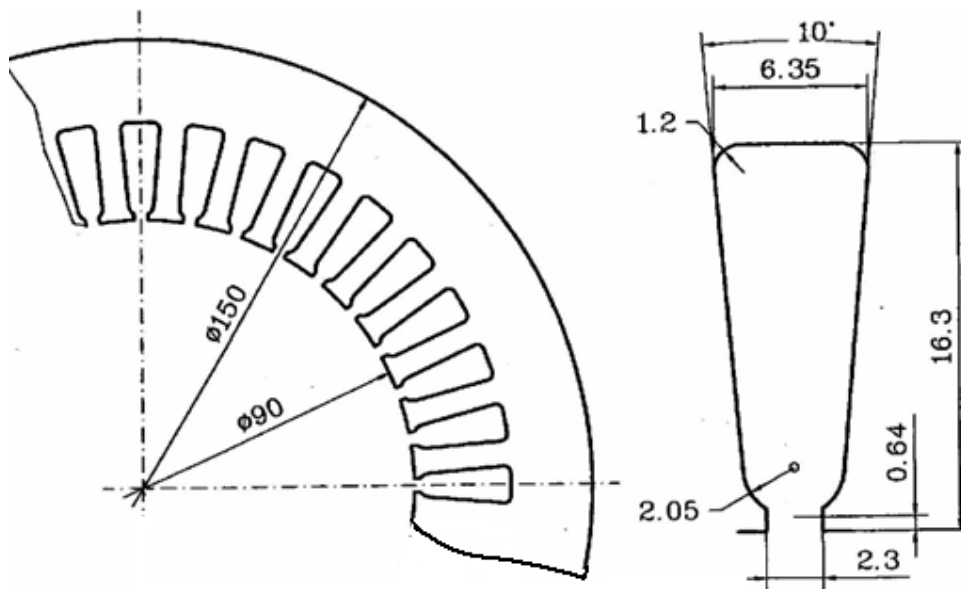


Figure 2.1: Stator core and slot geometry (dimensions in mm) [24], [33].

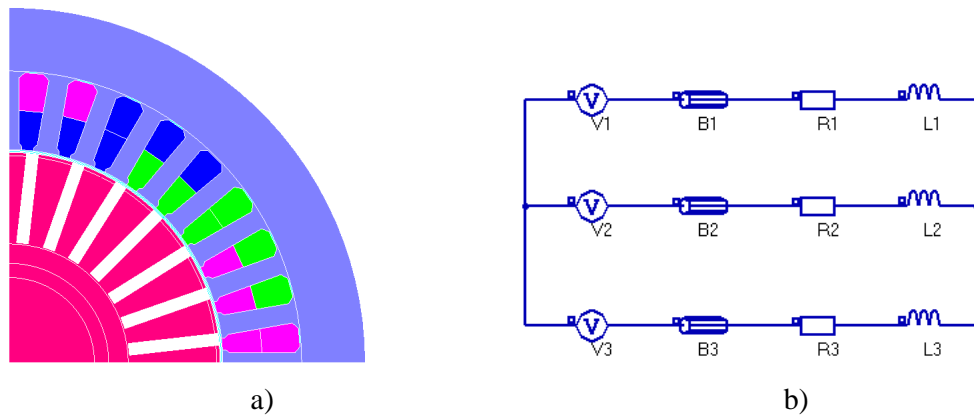


Figure 2.2: FE model of the machine: a) Model of the iron core with the stator winding, b) Coupled circuit to the model with a supply voltage V_1 , V_2 , V_3 per phase.

In the coupling circuit Fig. 2.2b V_1 , V_2 and V_3 are the three sinusoidal voltage sources; B_1 , B_2 and B_3 are the stator winding coils for phase A, phase B and phase C respectively; R_1 , R_2 and R_3 are the stator winding resistances for each phase and L_1 , L_2 and L_3 the end winding inductances per phase.

Table 2.2: Electrical parameters of the circuit to be coupled to the FE model

Parameter	Description	Value
R_1, R_2, R_3	Resistance of stator winding per phase at 20 °C[33]	0.024 Ω
L_1, L_2, L_3	Inductance of winding overhang per phase (2.25)	$2.5 \cdot 10^{-5}$ H
$\rho_{r,20^\circ\text{C}}$	Rotor core resistivity at 20 °C [41] [57]	$9.8 \cdot 10^{-8}$ Ωm
ε	Temperature coefficient of resistance of the rotor core [41], [57]	0.006 /K

The currents in the stator winding overhangs of the machine establish the flux linkage components that are not included in the fluxes, which are computed from the two dimensionally modelled areas in Fig. 2.2. These additional flux linkages must be taken into account in the voltage equation. This is done by adding the effect of end region fields into the equation as voltages in end-winding resistances and inductances. According to [44], [58], the end winding inductance per phase of a three-phase induction motor is expressed in the form

$$L_b = \mu_0 \cdot N_s^2 \cdot \frac{2}{p} \cdot \lambda_b \cdot l_b, \quad (2.25)$$

where μ_0 is the permeability of free space, N_s is the number of turns per phase, p is the number of pole pairs, $\lambda_b = 0.3$ is an empirical parameter, which depends on the geometry of the end-winding region and $l_b = 115$ mm is the average coil length of the winding overhang [33]. The 4-pole solid rotor induction FE model is developed, shown in Fig.2.2, and meshed (Fig.2.3), which is used for the analysis. The current penetration depth in the rotor iron core for the fundamental stator frequency is given at a calculated permeability μ as in (2.26).

$$d_E = \frac{1}{\sqrt{\pi \cdot s \cdot f_s \cdot \mu_r \cdot \mu_0 \cdot \kappa_r}}, \quad (2.26)$$

where μ_r is the relative permeability of the rotor iron core in the penetration depth area and κ_r is the conductivity of the rotor iron core. It is shown, that a fine mesh is constructed around the air gap to get a higher accuracy in computation of the induced electromagnetic torque (Fig.2.3). As it is recommended in [40], as a rule of thumb, the mesh element size in the rotor core near the air-gap region has been made to be at least three times less than the penetration depth of 4 mm for a stator frequency of $f_s = 800$ Hz and an operating slip of $s = 1.5$ %, at an assumed rotor temperature 200 °C according to (2.26). During the solving process, the mesh of the rotating air-gap is rebuilt at each change of the position of the rotor.

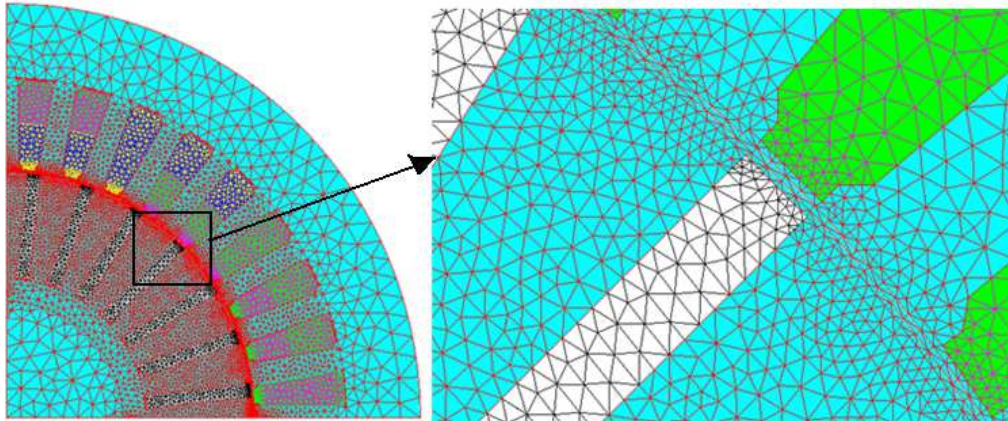


Figure 2.3: *FLUX 2D* mesh of the machine per pole with an air-gap detail (right).

The magnetic field is considered to be parallel to the centre lines of the machine poles, which corresponds to the *Neumann* boundary condition. It is also assumed that no flux penetrates the outer surface of the machine. This implies that the vector potential has a constant value on the boundary, which is known as *Dirichlet's* boundary condition [13]. The non-linearity of the stator and rotor core ferromagnetic materials leads in the FEM method to an iterative solution of the equation system of node values of the vector potential A_z , which is handled by using the *Newton-Raphson* iteration method.

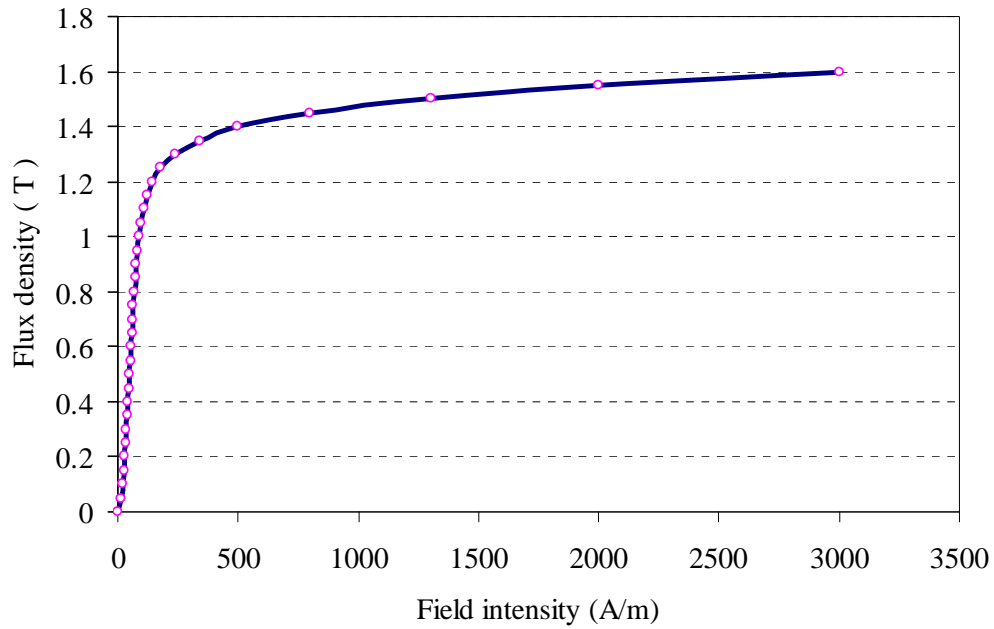


Figure 2.4: Magnetisation curve of the stator core *M330-35* [16].

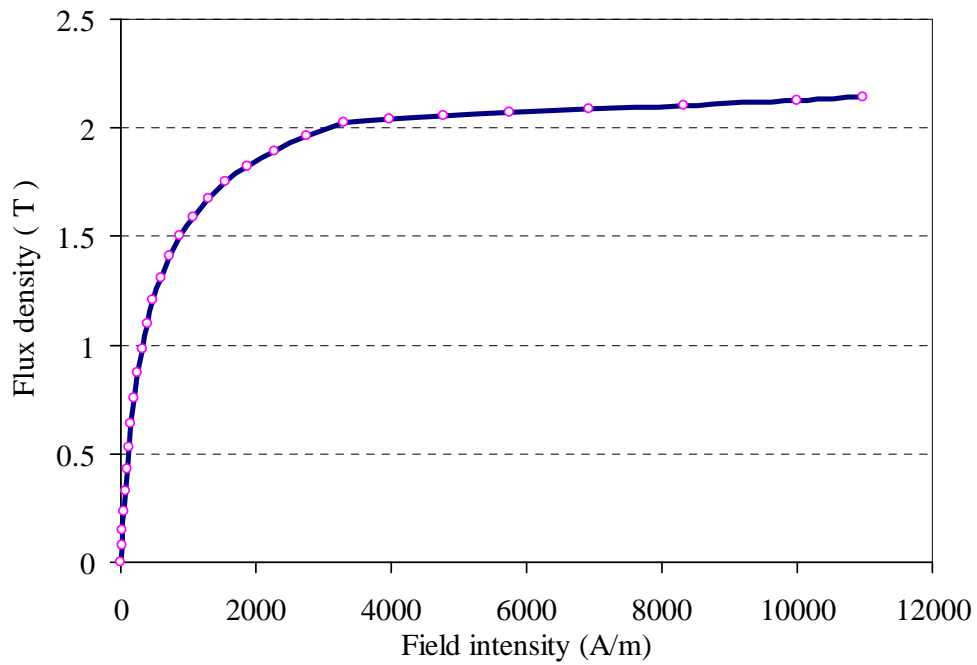


Figure 2.5: Magnetisation curve of the rotor core material (*VACOFER S1*) [42].

2.2.4 Rotor End Effects

The 3D rotor end effects without the influence of the copper end rings are considered in the 2D FE computation by increasing the rotor core resistivity (ρ_r) by a general equivalent end effect factor k_e , which is suitable for the considered axially slitted motor as given in (2.27). Without end-rings $k_e = \alpha$ according to (Fig. 2.6), and with end-rings k_e is used according to (2.28):

$$\rho_r' = k_e \cdot \rho_r, \quad (2.27)$$

$$k_e = 1 + C \cdot (\alpha - 1), \quad (2.28)$$

where $C = 0.3$ for thick copper end rings, which can be determined experimentally as reported in the study [25], and the coefficient α is expressed as:

$$\alpha = \frac{1}{k_R} = \frac{1}{1 - \frac{2 \cdot \tau_p}{\pi \cdot l_{Fe}} \tanh\left(\frac{\pi \cdot l_{Fe}}{2 \cdot \tau_p}\right)}, \quad (2.29)$$

where k_R is the *Russell* end effect factor [45], τ_p is the pole pitch and l_{Fe} is the rotor active iron length. The wave length of the inducing rotor rotating field wave is $2\tau_p$, so this value is used in (2.29) for α . In the Fig. 2.6b, for the line with copper end-rings one can assume that the rotor current flows more or less axially in the iron and in circumference direction in the copper end-rings. Hence the approximation of the 2D rotor current flow fits much better than without these end-rings, where $k_e = \alpha$ is used for the increase of resistance due to the circumferential rotor current flow in the iron. But in the power balance analysis, the losses in the copper-rings must be taken into consideration.

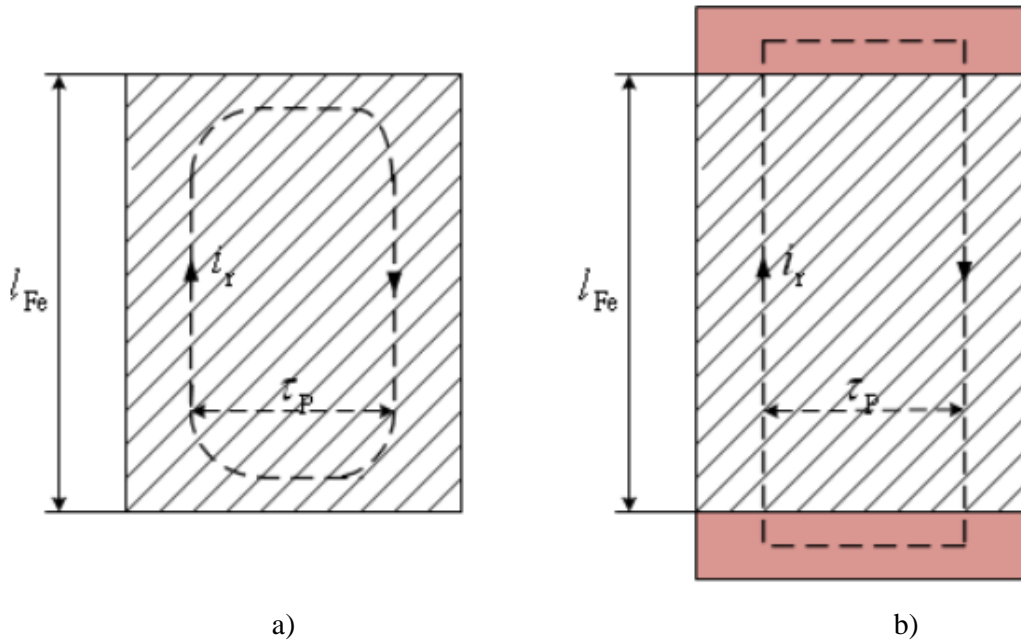


Figure 2.6: Rotor induced eddy current paths: a) without copper end-rings, b) with copper end-rings.

2.3 Steady-State AC Magnetic Analysis

In the time harmonic calculation (magneto-dynamic calculation), the unknown variable, the vector potential, is a complex quantity. It varies sinusoidal in time, similarly as the derivative quantities, the magnetic field strength (H) and magnetic flux density (B) vary sinusoidal, too. However in reality, due the non-linear nature of the magnetic core materials, the magnetic field and the magnetic induction can not have sinusoidal time dependence simultaneously (Fig. 2.7). Therefore, in order that these non-linear materials are taken into account, some approximations are applied. The FEM program *FLUX2D* computes, starting from the user defined $B(H)$ -curve, an equivalent $B(H)$ -curve, allowing the conversion of energy point by point. The method of an equivalent energy is explained in the *FLUX2D* user manual [13], which leads from the static $B(H)$ -curve to an equivalent $B(H)$ -curve.

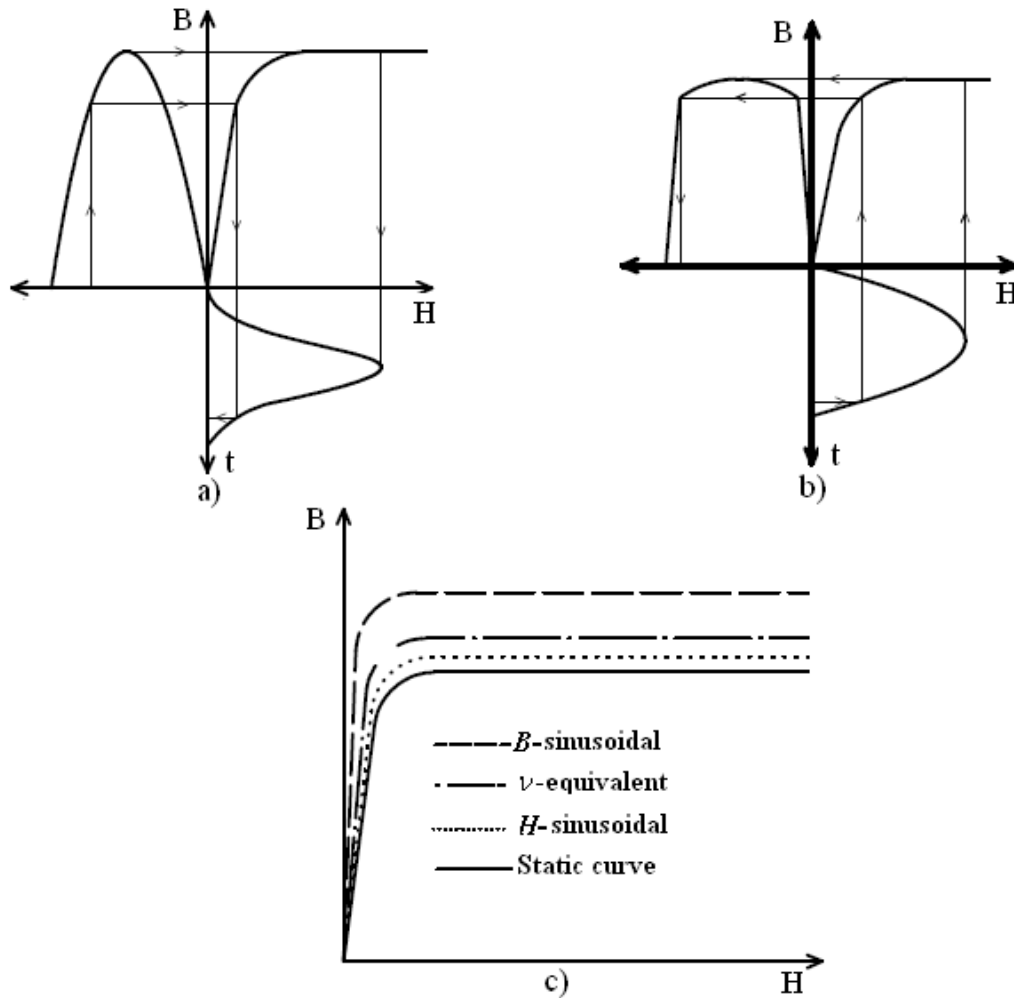


Figure 2.7: Non-linear behavior of the magnetic field strength H and the magnetic induction B : a) flux density varies sinusoidally, b) magnetic field strength varies sinusoidally and c) equivalent B - H -curve [25].

When a sinusoidal voltage source is used, the points on the curve are calculated supposing that the flux density varies sinusoidally as a function of time. When a sinusoidal current source is used, the points on the equivalent curve are calculated, supposing that the field strength H varies sinusoidally (Fig. 2.7). Both equivalent $B(H)$ -curves for sinusoidal B and for sinusoidal H yield $B-H$ -value pairs, which yield a higher B for a given H than the static curve. By choosing a parameter $0 < \nu < 1$, one can derive an equivalent $B(H)$ -curve, which is a mix of

the two equivalent curves, denoted as “ ν -equivalent” in Fig. 2.7c. For the current analysis, a sinusoidal voltage source is used. With the AC magnetic analysis, the spatial field harmonic effect which is presented here and PWM voltage time harmonics effects are neglected.

2.4 Calculation of Rotor Geometry

In the 2D steady state AC magnetic analysis, the computation time is much shorter than with a transient step-by-step simulation. Hence this method is implemented to calculate and optimize the rotor geometry parameters, i.e. the radial air-gap width, the slit-depth, the slit width and the end-ring thickness with a fair accuracy of the results.

2.4.1 Slit-Depth Optimization

It is known that the poor output characteristic of a smooth solid rotor induction motor can be improved by axially slitting the cross-section of the rotor [38], [43]. The slits are made by accurately milling narrow grooves at equal spacing on the rotor periphery [17], [18]. The axial slits increase the reluctance for the tangential flux path, and the flux has to penetrate deeper on its way to the other pole as shown in the Fig.2.10. The deeper flux penetration increases the rotor induced current penetration, which involves in the production of a higher electromagnetic torque, when the motor is operated at low slip. As a result, the torque increases with the increasing slit depth, until an optimum slit depth (“critical slit depth”) is reached, as it is demonstrated in the Fig. 2.8. The study shows, that the critical slit depth is at about half of the radius of the rotor, as it was researched in the works [1], [25]. A further increase in depth brings a decrease in torque, since the reluctance of the magnetic path to other pole increases much, resulting in a decrease in the amplitude of the flux density wave, which decreases the torque.

The following AC magnetic FEM analysed results are given for a slot width of $w_{\text{slit}} = 2.5 \text{ mm}$.

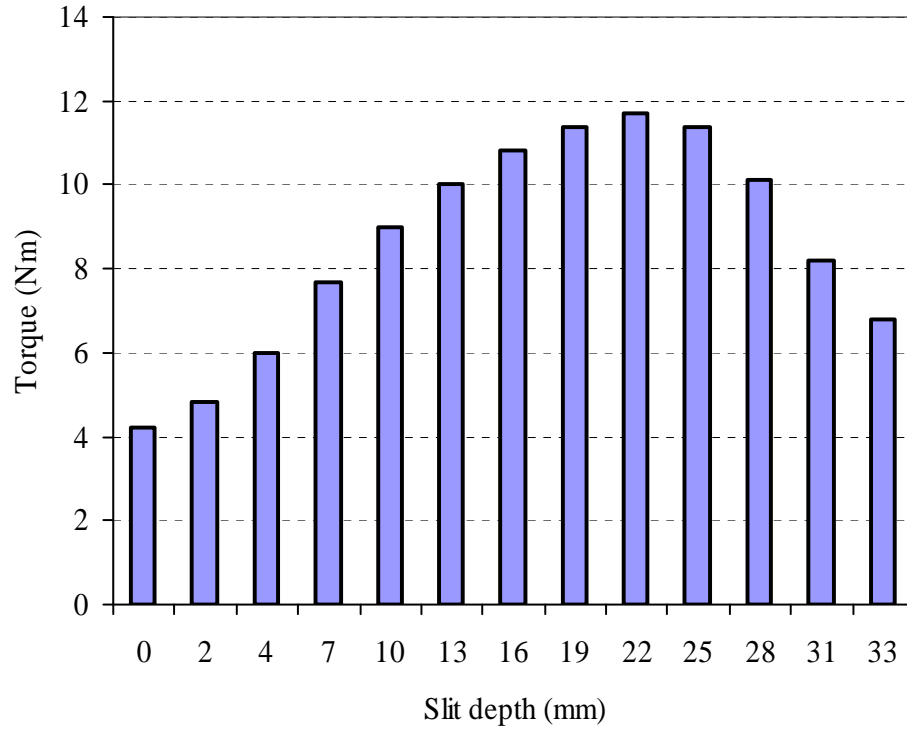


Figure 2.8: FEM calculated electromagnetic torque for different slit depths at a slip of $s = 1.5 \%$, line-to-line voltage $U_s = 330 \text{ V}$, Y , $f_s = 800 \text{ Hz}$, $w_{\text{slit}} = 2.5 \text{ mm}$, $\vartheta_{\text{rotor}} = 200^\circ\text{C}$.

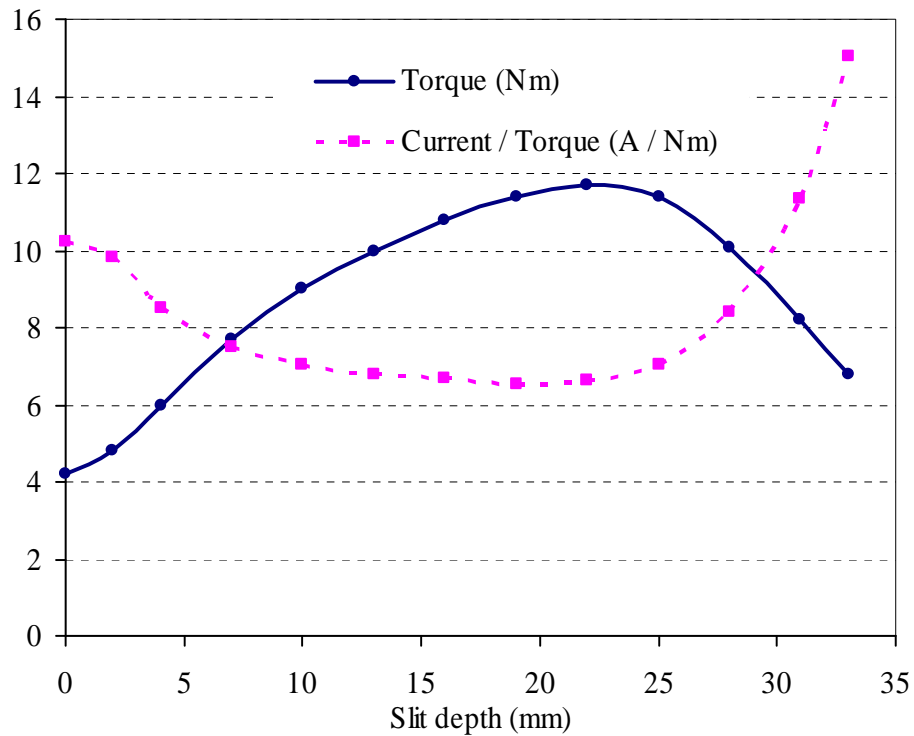


Figure 2.9: FEM calculated electromagnetic torque and ratio of input current per output torque for different slit depths of the 4-pole, axially slitted SRIM with copper end-rings at a slip of $s = 1.5\%$, line-to-line voltage $U_s = 330\text{ V}$, Y , $f_s = 800\text{ Hz}$, $w_{\text{slit}} = 2.5\text{ mm}$ and $\vartheta_{\text{rotor}} = 200^\circ\text{C}$.

According to the computation results given in the Fig. 2.9, for the designed 4-pole SRIM the 19 mm slit depth configuration is selected, which shows the maximum induced torque with minimum input current, resulting in an optimum depth at 19 mm.

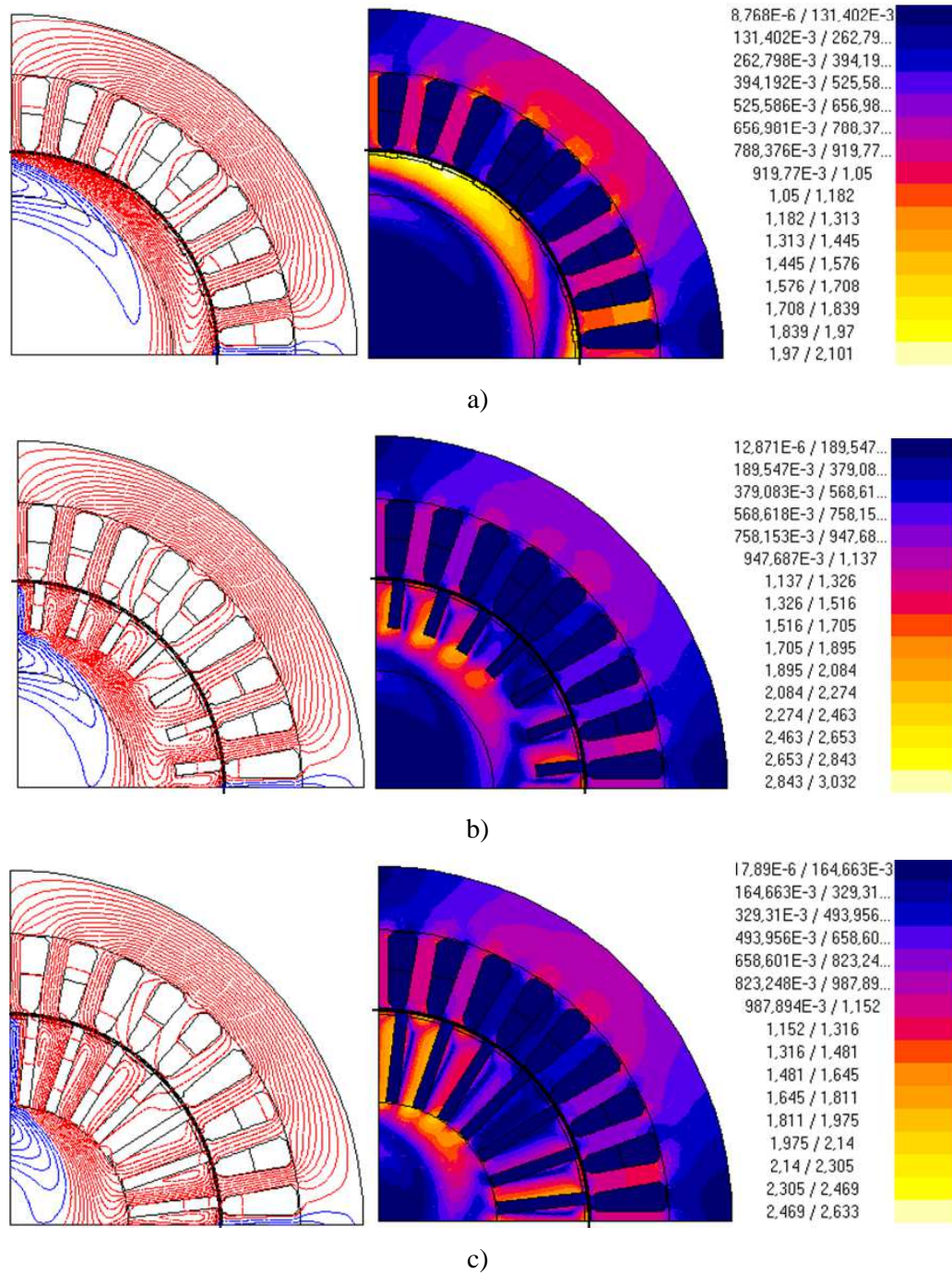


Figure 2.10: Computed flux lines and flux density distributions (in Tesla) of the 4-pole SRIM with axial slits at a slip $s = 1.5\%$, line-to-line voltage $U_s = 330\text{ V}$, Y , $f_s = 800\text{ Hz}$, $w_{\text{slit}} = 2.5\text{ mm}$, $\vartheta_{\text{rotor}} = 200^\circ\text{C}$ for different slit depths a) 0 mm, b) 10 mm and c) 19 mm.

2.4.2 Slit-Width Optimization

The slit width optimization has been done for a slit-depth of 19 mm and varying the slit-width from 0.5 mm up to 4 mm. The induced electromagnetic torque increases up to some optimum width, and for wider slits it decreases again. For narrow slits the tangential leakage flux increases, which tends to decrease the torque, whereas for wide slits the iron volume decreases, which also decreases the torque. In between, there is an optimum slit width, which is also practically suitable for the milling technology, where the maximum possible electromagnetic torque is produced, as illustrated in Fig. 2.11.

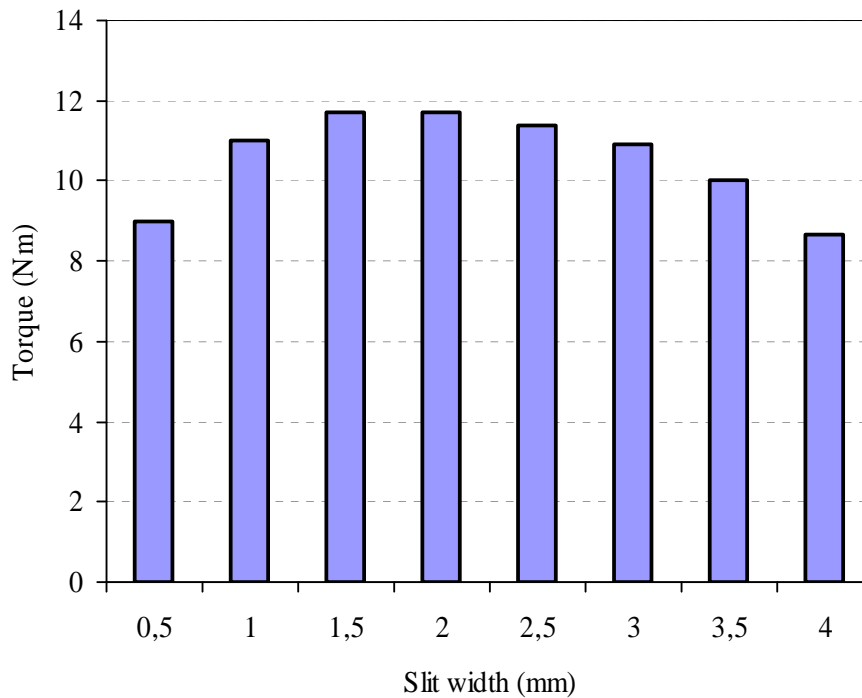


Figure 2.11: FEM calculated electromagnetic torque for different slit widths at a slip of $s = 1.5\%$, line-to-line $U_s = 330\text{ V}$, Y , $f_s = 800\text{ Hz}$, $h_{\text{slit}} = 19\text{ mm}$, $\vartheta_{\text{rotor}} = 200\text{ }^\circ\text{C}$.

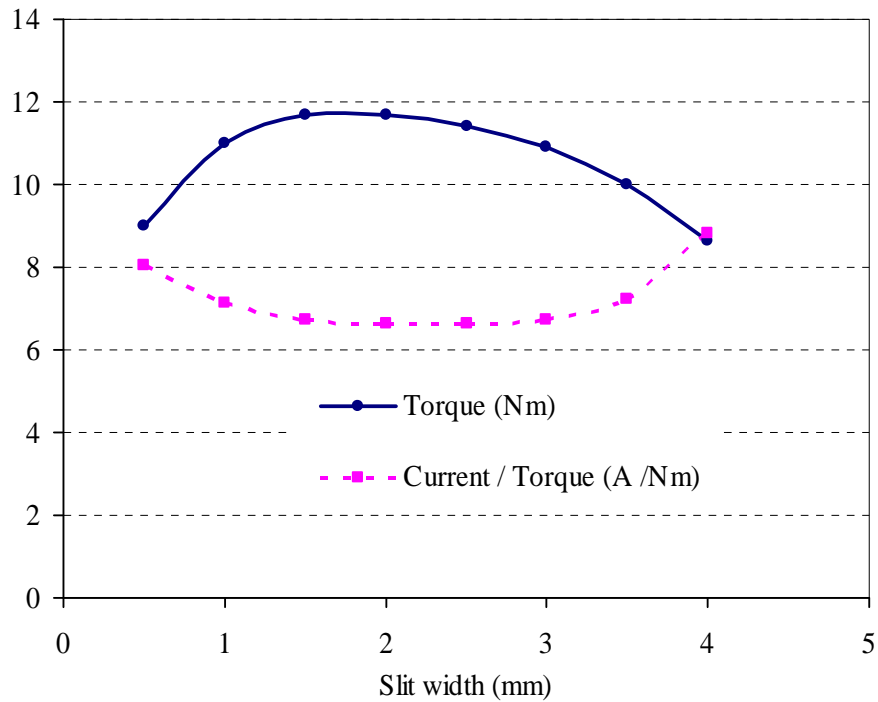


Figure 2.12: FEM calculated electromagnetic torque and ratio of input current per generated torque of the 4-pole SRIM with axial slits for different slit widths at a slip of $s = 1.5\%$, line-to-line $U_s = 330\text{ V}$, Y , $f_s = 800\text{ Hz}$, $h_{\text{slit}} = 19\text{ mm}$ and $\vartheta_{\text{rotor}} = 200^\circ\text{C}$.

The maximum induced electromagnetic torque with a minimum input current is found with a slit width between 2 to 2.5 mm. But from the machine processing in power tools point of view the slit depth 2.5 mm is selected for the design.

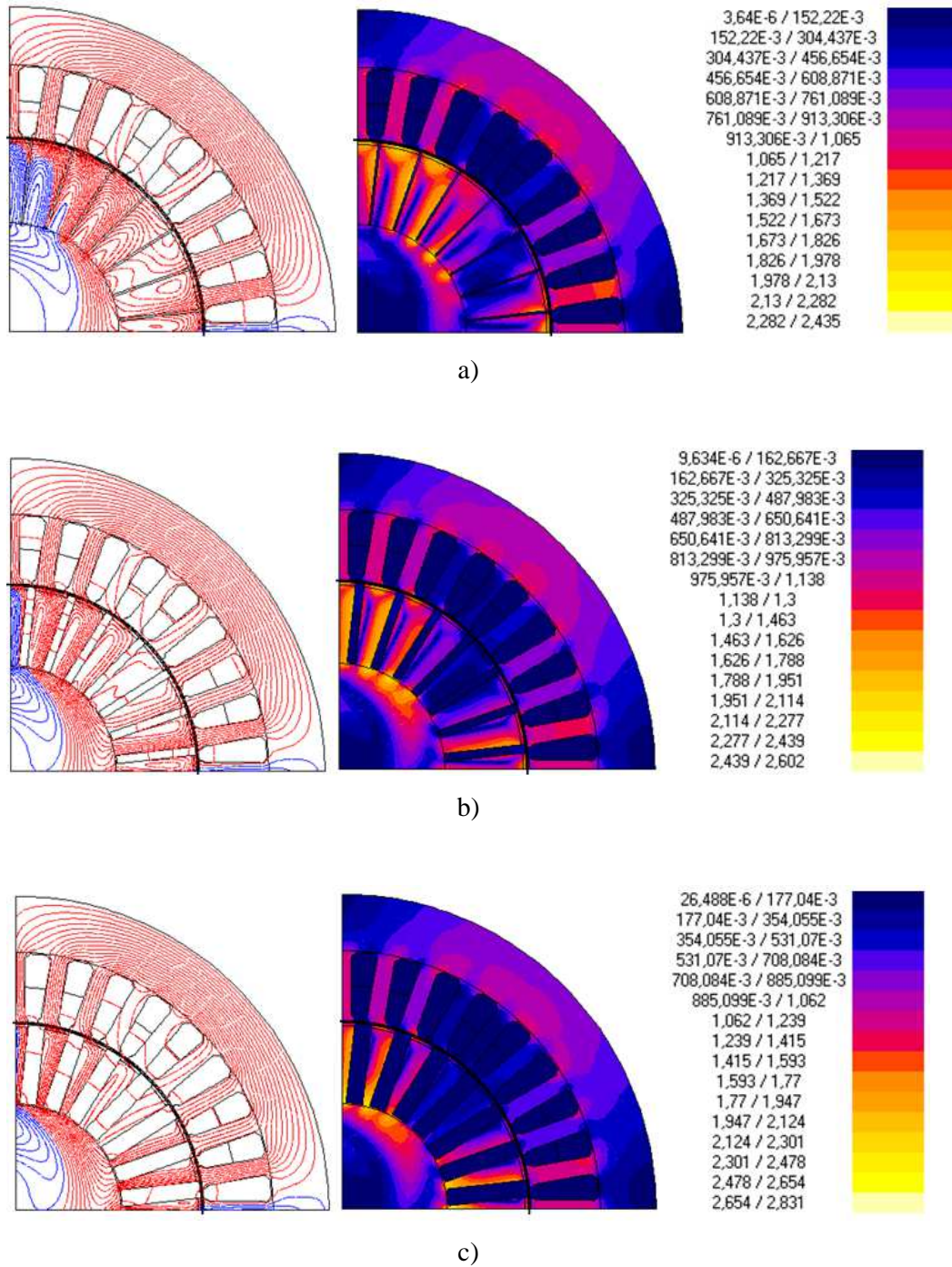


Figure 2.13: FEM computed field lines and flux density distributions of the 4-pole, axially slitted SRIM at a slip of $s = 1.5\%$, line-to-line $U_s = 330\text{ V}$, Y , $f_s = 800\text{ Hz}$, $h_{\text{slit}} = 19\text{ mm}$, $\vartheta_{\text{rotor}} = 200\text{ }^\circ\text{C}$ for different slit widths a) 0.5 mm, b) 2 mm and c) 4 mm.

2.4.3 End-Ring Thickness Calculation

The rotor end-ring thickness for the analysed axially slitted, 4-pole SRIM is estimated with the analogy of the squirrel cage induction motor. The rotor teeth in the rotor core act like rotor bars, where the fundamental harmonic current flows. The penetration depth of the rotor fundamental current in the iron is computed as in (2.30).

$$d_E = \frac{1}{\sqrt{\pi \cdot s \cdot f_s \cdot \mu_r \cdot \mu_0 \cdot \kappa_r}} \quad (2.30)$$

Taking the relative permeability in the penetration depth area $\mu_r = 283$ as shown on Fig. 2.13a at nominal operating slip $s = 1.6\%$, $f_s = 800$ Hz, the conductivity of the rotor core at the rotor temperature of $\kappa_{200^\circ C} = 4.9 \cdot 10^6$ S/m, the penetration depth is calculated to be 3.8 mm using (2.30). Assuming that the major part of the fundamental current penetrates deep into the teeth between the slits up to three times of the penetration depth ($3 \cdot d_E$), this results in a penetration of 11.4 mm. This iron penetration depth is taken as height of the current path, with the analogy of the height of the bar in squirrel cage induction motors. The average iron width ($b_{\text{iron}} = 6.6$ mm) along the current penetration is calculated from the rotor geometry as in (2.31).

$$b_{\text{iron}} = \frac{\left(\frac{2 \cdot \pi \cdot R_r}{2p} - \frac{Q_r}{2p} \cdot w_{\text{slit}} \right)}{\frac{Q_r}{2p}} = \frac{2 \cdot \pi \cdot R_r}{Q_r} - w_{\text{slit}}, \quad (2.31)$$

where $Q_r = 28$, $R_{r,\text{max}} = 44.6$ mm, $w_{\text{slit}} = 2.5$ mm. Hence the iron part of the teeth, where the current is flowing, is an iron teeth area of 75 mm^2 , which is given by the expression in (2.32).

$$A_{\text{iron}} = h_{\text{iron}} \cdot b_{\text{iron}}, \text{ with } h_{\text{iron}} = 11.4 \text{ mm} \quad (2.32)$$

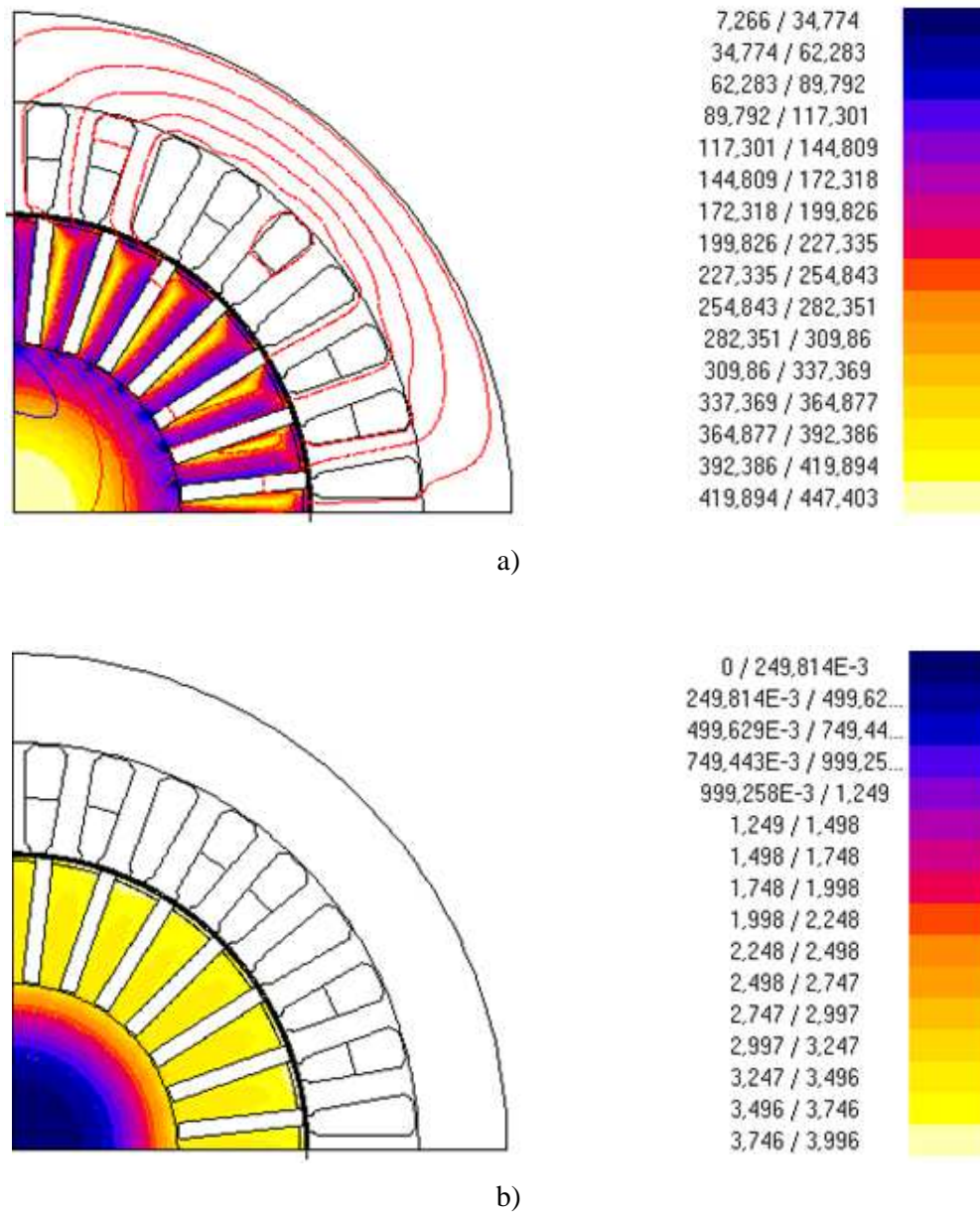


Figure 2.14: FEM computed result of the flux lines of the 4-pole SRIM at an operating slip of $s = 1.6\%$, line-to-line $U_s = 330\text{ V}$, $Y, I = 79\text{ A}$, $f_s = 800\text{ Hz}$, $h_{slit} = 19\text{ mm}$, $w_{slit} = 2.5\text{ mm}$, $\vartheta_{rotor} = 200^\circ\text{C}$: a) rotor relative permeability distribution ($\mu_{rel,rot}$), and b) rotor current density distribution (J_r) in A/mm².

For the nominal operating point FE computation, the rotor current is 279A calculated by (2.33),

$$I_r = J_r \cdot A_{\text{iron}} = 270\text{A}, \quad (2.33)$$

where $J_r \approx 3.6 \text{ A/mm}^2$ is the average rotor current density in the skin depth as shown in FE computation result Fig.2.14b. The ring segment current I_{ring} between two rotor teeth then is estimated as in the case of the squirrel cage induction motor to be equal to 607A, as given by (2.34).

$$I_{\text{ring}} = \frac{I_r}{2 \cdot \sin(p\pi / Q_r)} \quad (2.34)$$

The end-ring effective area for the flow of the major part of the fundamental ring segment rotor current I_{ring} is 169 mm^2 according to (2.35):

$$A_{\text{ring}} = \frac{I_{\text{ring}}}{J_{\text{ring}}}, \quad (J_{\text{ring}} = J_r = 3.6 \text{ A/mm}^2), \quad (A_{\text{ring}} = 169 \text{ mm}^2) \quad (2.35)$$

Hence, for the calculated necessary ring cross section, the end ring thickness (b_{ring}) is found to be 15 mm from the relation (2.36).

$$b_{\text{ring}} = \frac{A_{\text{ring}}}{b_{\text{iron}}} \approx 15 \text{ mm} \quad (2.36)$$

2.5 Time Stepping (Magneto-Transient) Analysis of SRIM

The transient magnetic formulation of the 2D FEM calculation involves the solving the field and circuit coupled problem at discrete points in time domain, using a small constant time step of $\Delta t = 6 \cdot 10^{-6}$ s. Accordingly, during the rotation, the rotor has made 100 time steps per moving by one pole pitch. The spatial harmonic effects of the air-gap field, which were not considered in the time harmonic analysis, are here taken in to account. The influence of the PWM effect is still neglected, as a sine-wave filter operation is assumed.

2.5.1 FEM Model for Transient Analysis

For the magneto-transient analysis, the same FE model with the time harmonic analysis is used with redefining the model application to a transient magnetic problem. Here, the sinusoidal input phase voltages as power supplies are defined by their peak values, their operating frequency, and their phase angle difference at the zero instant time. In the given study, a sinusoidal three-phase voltage supply system is considered, which is modelled in the coupled circuit equation as illustrated in Fig. 2.15.

2.5.2 Time Stepping Computation Results

The Fig. 2.16 shows the computed input phase currents, which have a sinusoidal variation, like the feeding voltage system with a lagging phase angle difference, giving a power factor of $\cos \varphi = -0.71$.

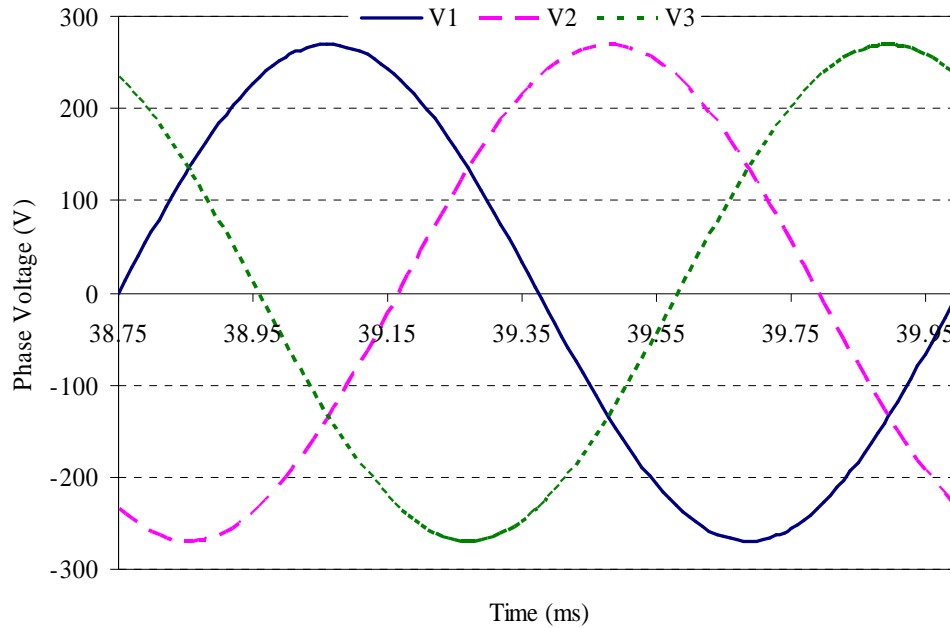


Figure 2.15: A three-phase sinusoidal feeding phase voltage system 191V (RMS) at $f_s = 800$ Hz.

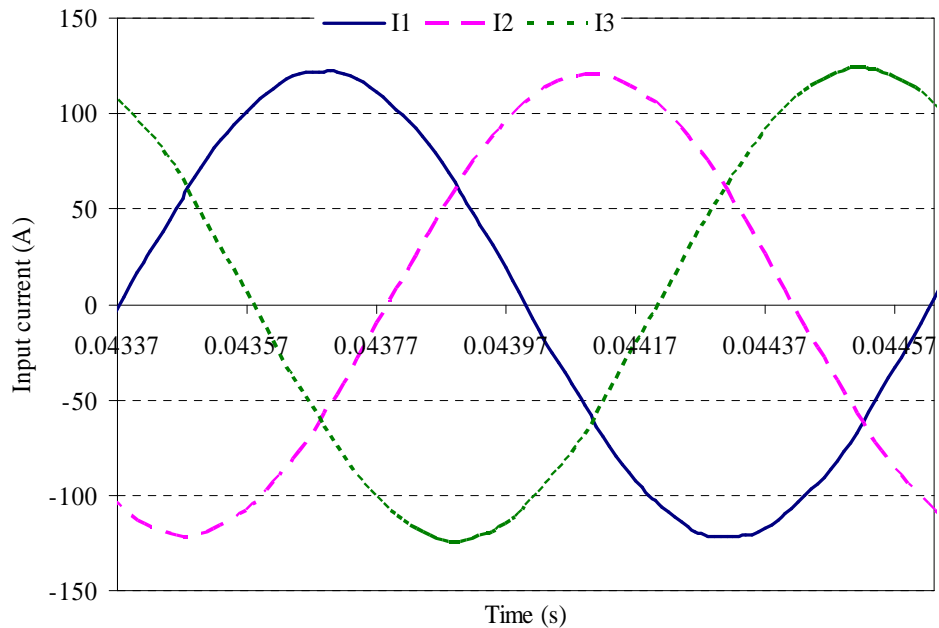


Figure 2.16: Time stepping computed three-phase input phase currents 82 A (RMS) of the 4-pole SRIM at an operating slip of $s = 1.8\%$ line-to-line voltage $U_s = 330$ V, Y, $f_s = 800$ Hz, $h_{\text{slit}} = 19$ mm, $w_{\text{slit}} = 2.5$ mm, $\vartheta_{\text{rotor}} = 200$ °C.

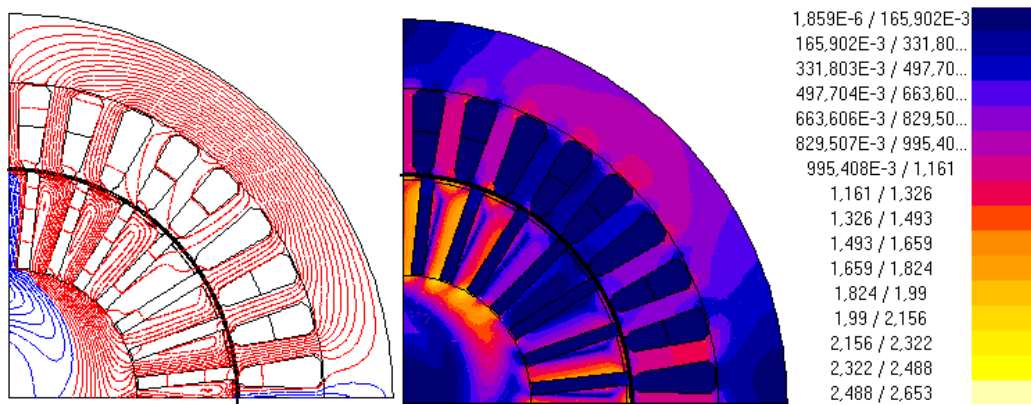


Figure 2.17: Time stepping computed air-gap field lines and flux density distributions of the 4-pole SRIM at an operating slip of $s = 1.8\%$, line-to-line voltage $U_s = 330$ V, Y, $f_s = 800$ Hz, $I_s = 82$ A, $M_e = 12$ Nm.

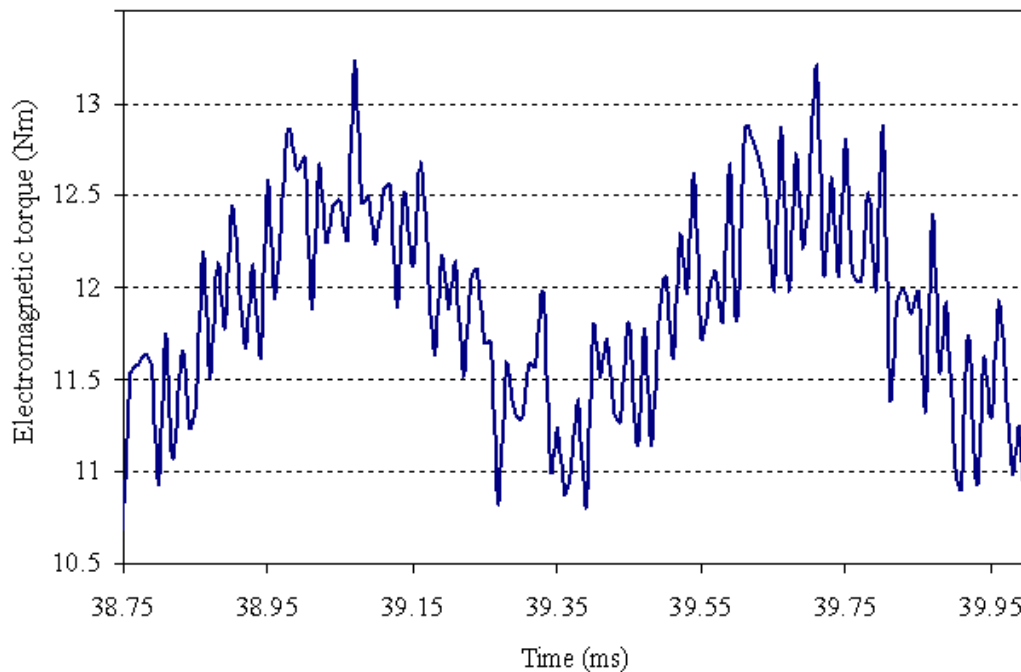


Figure 2.18: Time stepping FEM computed air-gap electromagnetic torque at a slip $s = 1.8\%$, line-to-line voltage $U_s = 330$ V, Y, $f_s = 800$ Hz, $I_s = 82$ A.

With the given preliminary optimization of the rotor parameters, the time stepping computed average air-gap electromagnetic torque of the axially slitted, 4-pole SRIM is 12 Nm (Fig. 2.18) at the operating slip of 1.8%.

3 Losses in Solid Rotor Machines

The power losses in electrical machines determine the efficiency of the motor and also the cooling, which is required to keep the temperature of the insulation below the upper limit. Insulation materials are very sensitive to over-temperature, as the velocity of chemical decomposition of the insulation materials increases exponentially with temperature. For example, for transformer oil and solid insulation materials *Montsinger's* rule is valid, that can be expressed as: life span of the insulation decreases by about 50 % with an increase of temperature by 10K [40]. The motor efficiency η is expressed as the ratio between the mechanical power output P_{out} and the applied electrical power input P_{in} .

$$\eta = \frac{P_{\text{out}}}{P_{\text{in}}} \quad (3.1)$$

The power absorbed in the electric motor is the loss incurred in making the electromechanical energy conversion process. The total power loss P_{loss} of the motor is the difference between supplied electrical power input P_{in} and mechanical power output P_{out} .

$$P_{\text{loss}} = P_{\text{in}} - P_{\text{out}} \quad (3.2)$$

The power losses in electrical machines can be subdivided into electrical, magnetic and mechanical losses. During the energy conversion process all losses are transferred into heat energy in the system. In this chapter, the losses of a 4-pole axially slitted SRIM with copper end-rings are calculated analytically with the aim of loss reduction, using parameters, which are results of numerical computation at sinusoidal voltage supply.

3.1 Electrical Losses

Electrical *Joule* losses in current carrying conductors include copper losses of the stator winding $I^2 \cdot R$ due to the current flow with fundamental and harmonic frequencies and losses due to the current displacement. The total winding losses comprise the $I^2 \cdot R$ losses plus the 1st order current displacement losses $P_{\text{Cu,Ft,b}}$ due to unbalanced current sharing between the a_i parallel wires per turn plus the 2nd order current displacement losses $P_{\text{Cu,Ft,a}}$ due to the skin effect within each wire. The phase resistance R_s of the stator winding depends on the operating temperature. The phase current I flows in the winding conductors. With the time changing magnetic and electric fields along the conductor due to a sinusoidal alternating current I , depending on the geometry and operating frequency, eddy currents are induced mainly in the slot part of the conductors. Due to these eddy currents, superimposed on the current flow I , the total conductor current density J is displaced within the conductor cross-section, which is known as ‘skin effect’. Accordingly, due to this so-called second order current displacement the stator AC resistance increases, which increases the stator *Joule* losses by the value $P_{\text{Cu,Ft,a}}$. On the other hand, the first order current displacement losses ($P_{\text{Cu,Ft,b}}$) occurs due to the unequal current distribution on parallel wires per turn, which can be estimated empirically, as given in [58].

$$R_s = R_{s,20^\circ} \left(1 + \frac{\vartheta - \vartheta_0}{235 + \vartheta_0} \right) \quad (3.3)$$

In (3.3) $R_{s,20^\circ}$ is the phase winding dc-resistance at $\vartheta_0 = 20^\circ \text{C}$, and ϑ is the winding operating temperature.

$$P_{\text{Cu,s}} = 3 \cdot I^2 \cdot R_s + P_{\text{Cu,ad}} \quad (3.4)$$

High speed machines operate at higher stator electric frequencies, so the current displacement, caused by internal eddy currents, plays an important role. A dc current is equally distributed over the conductor cross-section, but the ac current is not due to the skin-effect. The current penetration depth is roughly defined as boundary of the region, where the largest part of the current flows. This region is only some part of the conductor cross-section area, so the equivalent resistance, which is called ‘AC resistance’ to be used in the copper loss expression ($I^2 \cdot R$) is increased, caused by both first and second order current displacements. The increase in the AC winding resistance accounts for the winding losses, which are determined roughly by the expressions (3.6) and (3.12) [58].

$$P_{\text{Cu,ad}} = P_{\text{Cu,Ft,a}} + P_{\text{Cu,Ft,b}} \quad (3.5)$$

$$P_{\text{Cu,Ft,a}} = 3R_s \cdot I_s^2 (\bar{k}_a - 1) \quad (3.6)$$

$$\bar{k}_a = \frac{k_a \cdot l_{\text{Fe}} + l_b}{l_{\text{Fe}} + l_b} \quad (3.7)$$

$$k_a = \varphi(\xi_T) + \frac{m_T^2 - 1}{3} \cdot \psi(\xi_T) \quad (3.8)$$

$$\varphi(\xi_T) = \xi_T \cdot \frac{\sinh(2\xi_T) + \sin(2\xi_T)}{\cosh(2\xi_T) - \cos(2\xi_T)} \quad (3.9)$$

$$\psi(\xi_T) = 2\xi_T \cdot \frac{\sinh(\xi_T) - \sin(\xi_T)}{\cosh(\xi_T) + \cos(\xi_T)} \quad (3.10)$$

$$\xi_T = b_T \sqrt{\mu_0 \pi \kappa_{\text{Cu}} f_s \cdot a_T b_T / b_{\text{Qm}}} \quad (3.11)$$

The additional losses due to current displacement in the winding overhang area are much smaller than in the slots, since the end winding leakage flux density is much smaller than the slot leakage flux density. Here, it is assumed that along the overhang length l_b of the turns the additional losses are zero (3.7). The 1st order current displacement due to unequal distribution of currents among parallel wires is determined as follows:

$$P_{\text{Cu,Fe,b}} = 3R_s^2 I_s^2 (k_b - 1) , \quad (3.12)$$

$$k_b = \varphi(\xi) + \eta(\eta + 1) \cdot \psi(\xi) , \quad (3.13)$$

$$\xi = h_L^* \cdot \sqrt{\mu_0 \pi \kappa_{\text{Cu}} \cdot \frac{l_{\text{Fe}}}{l_{\text{Fe}} + l_b} \cdot f_s \cdot a_T b_T / b_{\text{Qm}}} . \quad (3.14)$$

In equation (3.7) ÷ (3.14) the following parameters are used: l_b is the end winding overhang length, l_{Fe} is the iron core length, a_T is the average wire numbers side by side in a slot width, m_T is the number of coil sides one over the other in a slot height as shown on Fig.3.1, b_T is the width of an "equivalent" quadratic profile wire given by $b_T = \sqrt{d_{\text{Cu}}^2 \cdot \pi / 4}$, b_{Qm} is the average slot width, κ_{Cu} is the electrical conductivity of the conductors at operating temperature and f_s is the electric frequency. The term η is described in the following two extreme cases for the designed double layer winding:

$$\eta = \frac{m_L - 1}{2} , \text{ (Fig.3.1b)} \quad (3.15)$$

$$\eta = -\left(\frac{m_L}{4} + \frac{1}{2}\right) , \text{ (Fig.3.1c)} \quad (3.16)$$

where h_L^* is the height of the conductor, which is made from parallel connected sub-conductors, and m_L is the number of conductors on top of each other as given in the conductor distribution on the Fig. 3.1.

The equations (3.5) up to (3.14), which were developed by *Emde* and *Field*, are applicable for rectangular profile conductors, which are regularly placed in a parallel sided slot. Therefore, since the studied machine has oval shaped stator slots with round wires, for the calculation of the additional losses these wires must be considered as approximated rectangular profile conductors of the same cross-section in an 'equivalent' slot parallel sided slot. For the designed machine a double layer winding with $N_c = 8$ turns/coil with 3 parallel round wire conductors is selected. It implies that the conductors are placed in the slots more or less randomly. Therefore, in order to calculate the first order current displacement additional losses with a fair accuracy, it is determined by consideration of the average loss value of the best case (3.15) and the worst case (3.16) arrangements of conductors in the considered 'equivalent' slot (Fig.3.1b,c) [33]. Hence the total current displacement additional losses are determined as:

$$P_{Cu,ad} = P_{Cu,Ft,a} + (P_{Cu,Ft,b,best} + P_{Cu,Ft,b,worst}) / 2 . \quad (3.17)$$

Accordingly, the stator $I^2 \cdot R$ and additional stator winding copper losses are calculated analytically for a sinusoidal current I , and results are given in Table 3.1. The current in (3.4) is computed numerically in a time stepping FEM (magneto-transient) analysis of the 4-pole axially slitted SRIM with copper end rings for a given torque $M_e = 12$ Nm.

Table 3.1: Analytically calculated stator winding losses $I^2 \cdot R$ and additional copper losses of the 4-pole SRIM at the stator winding temperature $\vartheta_{\text{Cu,s}} = 100^\circ\text{C}$, $R_{\text{s},20^\circ} = 0.024\ \Omega$ and $M_e = 12\ \text{Nm}$

f / Hz	U_{ph} / V	$s / \%$	I_s / A	P_{Cu} / W	$P_{\text{Cu,ad}} / \text{W}$	$P_{\text{Cu,ad}} / P_{\text{Cu}}$
800	191	1.8	83.8	674	37.8	0.06
600	143	2.4	84.4	684	19.2	0.03
400	95	3.6	84.9	692	10.1	0.02

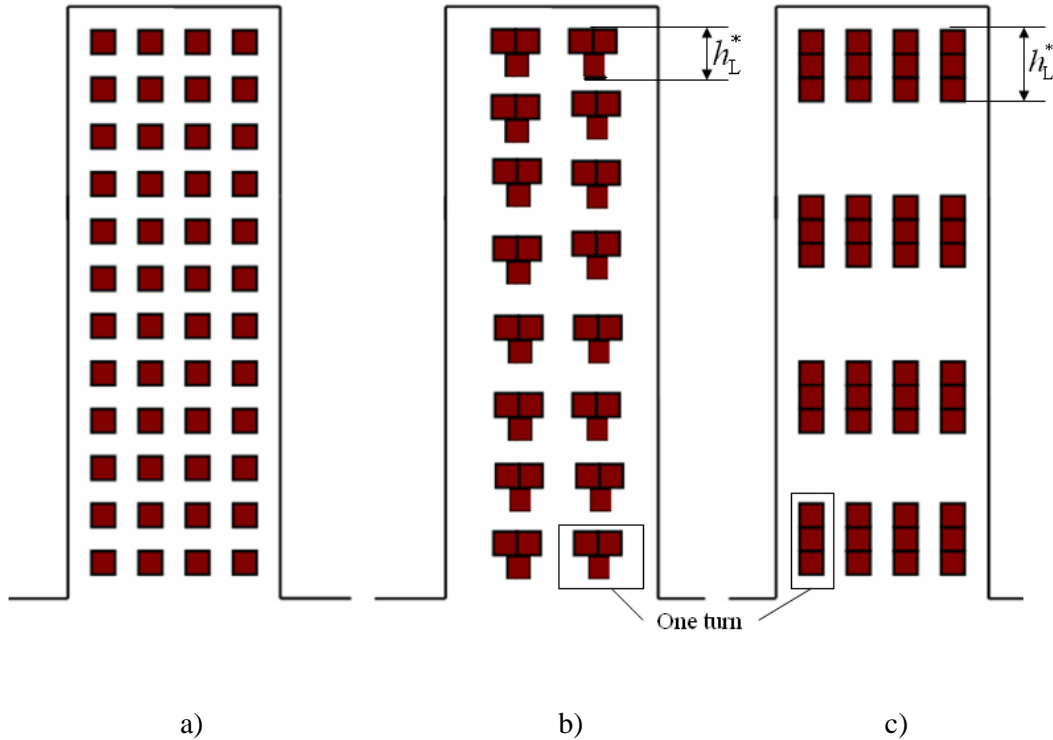


Figure 3.1: Conductor distributions of the 4-pole SRIM in a slot shown to calculate the additional copper losses due to a) the skin effect within each parallel wire ($a_T = 4$, $m_T = 12$) b) an unequal sharing of currents among parallel wires with a minimum equivalent conductor height (best case) ($a_T = 4$, $m_L = 8$) and c) an unequal sharing of currents among parallel wires with a maximum equivalent conductor height (worst case) ($a_T = 4$, $m_L = 4$).

It is seen from the calculated results (Table 3.1), that for the rated operating frequency $f = 800$ Hz the first and second order current displacement additional losses constitute 6 % of the $I^2 \cdot R$ copper losses.

3.2 Magnetic Losses

The magnetic losses at fundamental stator current operation include the stator and rotor iron core losses. The rotor core losses include rotor eddy current losses of the fundamental and high frequency harmonic rotor currents and rotor hysteresis losses.

3.2.1 Stator Core Losses

Magnetic iron losses are caused by time-changing magnetic fields in ferromagnetic material. They include hysteresis losses P_{Hys} due to with the magnetic hysteresis loop of the ferromagnetic material and eddy current losses. The eddy current losses P_{Ft} themselves are separated into classical eddy current losses P_{class} and excess losses P_{ex} due to the non-uniform distributions of magnetic flux density in the lamination because of the grain properties of the ferromagnetic material [25].

$$P_{\text{Fe}} = P_{\text{Hys}} + P_{\text{Ft}} \quad (3.18)$$

$$P_{\text{Ft}} = P_{\text{class}} + P_{\text{ex}} \quad (3.19)$$

The hysteresis losses from the AC magnetisation process are equal to the area of the quasi-static hysteresis loop times the magnetising frequency and the volume of the core. The loss energy density per cycle of the hysteresis loop can be expressed as:

$$w = \oint HdB \quad (3.20)$$

Since the area of the hysteresis loop increases with increasing maximum induction B_m , the loss energy can be expressed as a function of it. Hence, the specific hysteresis loss can be approximately calculated using an empirical relationship (3.21) from *Steinmetz*, which is based on experimental studies.

$$p_{\text{Hys}} = k_h \cdot f \cdot B_m^2, \quad (3.21)$$

where k_h is a hysteresis loss constant, which is determined by the nature of the core material and comprises the average effect of rotating and pulsating magnetic fields, f is the frequency and B_m is the maximum flux density. According to equation (3.21), the hysteresis loss depends on the square of the magnetic flux density and is linear proportional to the frequency of the field. Eddy current losses are caused by induced electric currents in the magnetic core by an external time changing magnetic field. The specific eddy current losses per volume are expressed as in (3.22), which holds true, as long as the penetration depth of the eddy current distribution is much bigger than the sheet thickness.

$$p_{\text{Ft}} = k_{\text{Ft}} \cdot f^2 \cdot B_m^2, \quad (3.22)$$

The eddy current loss constant k_{Ft} considers the conductivity and the thickness of the sheets [48]. Due to the difference of the flux density in the yoke and teeth of the stator core, it is recommended to separate the loss calculation into two sections. Due to the punching of the slots in the sheets, the punching shear stress in the iron increases the hysteresis losses as well. Punching also destroys the insulation of the lamination sheets partially. Thus bridging of the sheets occurs, when they are stacked together. This causes an increase of eddy current losses. As the ratio of cutting or punching length versus the sheet surface is bigger for the teeth than for the yoke, the typical loss increase rates are $k_{\text{vd}} = 1.8 \dots 2.0$ for teeth and $k_{\text{vy}} = 1.3 \dots 1.5$ for the yoke [33].

Accordingly, the total hysteresis and eddy current losses can be calculated roughly as:

$$P_{\text{Fe,d}} = k_{\text{vd}} \cdot \left(\frac{B_{\text{d},1/3}}{1.0} \right)^2 \cdot \nu_{10} \cdot m_{\text{d}} \cdot k_{\text{f}}, \quad (3.23)$$

$$P_{\text{Fe,y}} = k_{\text{vy}} \cdot \left(\frac{B_{\text{ys}}}{1.0} \right)^2 \cdot \nu_{10} \cdot m_{\text{y}} \cdot k_{\text{f}}, \quad (3.24)$$

$$\nu_{10} = p_{\text{Hy}} \cdot (f/50) + p_{\text{Ft}} \cdot (f/50)^2 \cdot (b_{\text{sh}}/0.5)^2, \quad (3.25)$$

where ν_{10} is the total iron loss constant calculated as in (3.25), $B_{\text{d},1/3}$ and B_{ys} are the magnetic flux densities at the stator teeth at 1/3 of the tooth length and the stator yoke respectively, m_{d} and m_{y} are the mass of the stator teeth and stator yoke respectively, b_{sh} is the thickness of the selected less loss stator laminated sheet (M330-35A) and k_{f} is the lamination stacking factor. In (3.25) f is to be used in [Hz] and b_{sh} in [mm]. The formulas (3.23) ÷ (3.25) are valid for sinusoidal time variation in time.

In this study, the stator iron losses are calculated numerically as a post processing analysis of the time stepping FEM simulations using the *Bertotti* formula given in (3.26) [9], [13]. So a non-sinusoidal time variation of $B(t)$ can be considered, including the effect of excess losses. In (3.26) it is assumed, that $B(t)$ contains a fundamental sinusoidal variation $B(t)$ with the frequency f and that the deviation of that does not influence the hysteresis losses.

$$p(t) = k_{\text{f}} \cdot \left(k_{\text{h}} B_{\text{m}}^2 f + \kappa \cdot \frac{b_{\text{sh}}^2}{12} \left(\frac{dB(t)}{dt} \right)^2 + k_{\text{ex}} \left(\frac{dB(t)}{dt} \right)^{1.5} \right) \quad (3.26)$$

So $p(t)$ are the specific iron losses per volume of the iron core, k_f is the laminations stacking factor, k_h is hysteresis loss constant, B_m is the maximum flux density of the fundamental sinusoidal time variation, f is the operating fundamental frequency, κ is the electrical conductivity of the core sheets, b_{sh} is the lamination thickness, and k_{ex} is the excess eddy current losses constant. However, the hysteresis (k_h) and excess loss (k_{ex}) constants are unknown in the expression (3.26), which can be determined using (3.27), of the total iron losses for the case of a harmonic field variation with the frequency f [13]. Since the unknowns are two, the constants are determined by expressing the equation (3.27) by two equations for two frequencies i.e. for 200 and 400 Hz with 8.25 W/m^3 and 23.54 W/m^3 specific iron losses respectively, as shown on Fig. 3.2.

$$p = \left(k_h \cdot B_m^2 \cdot f + \frac{\pi^2 \kappa \cdot b_{sh}^2}{6} (B_m \cdot f)^2 + k_{ex} (B_m \cdot f)^{1.5} \cdot 8.67 \right) \cdot k_f \quad (3.27)$$

Table 3.2: Calculated results of hysteresis and excess loss constants for the lamination sheet *M330-35*: $\kappa = 2.63 \cdot 10^6 \text{ S/m}$, $k_f = 0.97$, $B_m = 1 \text{ T}$ and $b_{sh} = 0.35 \text{ mm}$

f (Hz)	p (W/kg)	p (W/m ³)	k_h (W·s/T ² ·m ³)	k_{ex} (W/m ³)·(T/s) ^{1.5}
200	8.25	63112.5	140.4	0.56
400	23.54	180081		

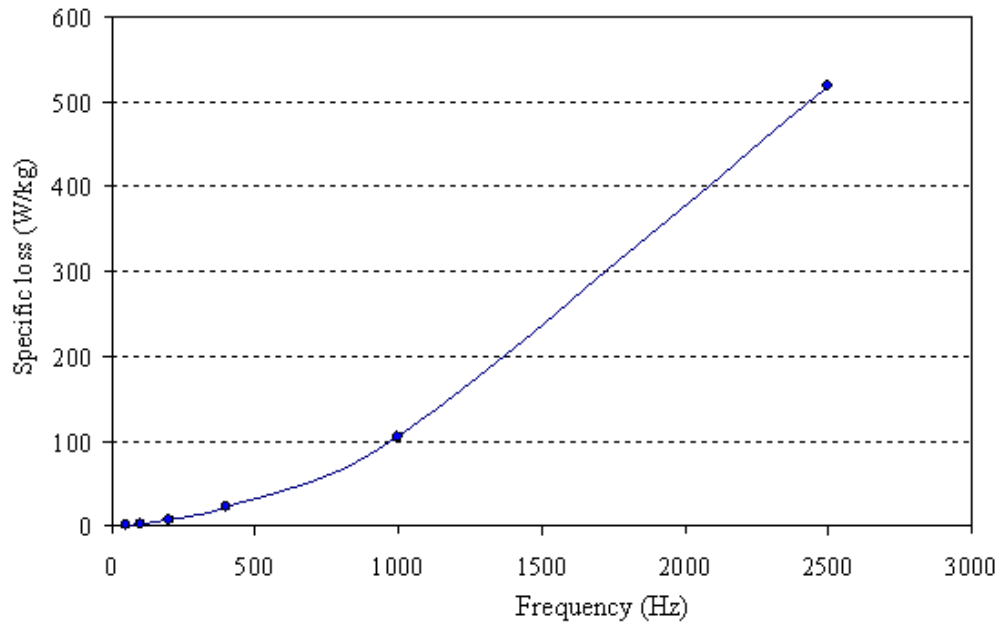


Figure 3.2: Specific magnetic losses of the core *M330-35A* [16].

So, the total magnetic losses are calculated by the FEM program as $p_d V_d = P_{Fe,d}$ for the teeth and as $p_Y V_Y = P_{Fe,Y}$ for the stator yoke, where V_d and V_Y are the teeth and the yoke volumes respectively and are presented in the Table 3.3 below.

Table 3.3: FEM calculated stator core losses for the 4-pole SRIM at the stator winding temperature $\vartheta_{Cu,s} = 100^\circ\text{C}$ and generated electromagnetic torque $M_e = 12\text{ Nm}$

f / Hz	U_{ph} / V	$s / \%$	I_s / A	$P_{Fe,Y} / \text{W}$	$P_{Fe,d} / \text{W}$	$P_{Fe,s} / \text{W}$
800	191	1.8	83.8	264.1	399.1	663.2
600	143	2.4	84.4	175.4	244.6	420.0
400	95	3.6	84.9	95.8	125.5	221.3

It is remarked that for all the studied operating frequencies the losses in stator teeth constitute 60 % of the total iron losses. The higher iron loss in stator teeth is associated with the higher flux density $B_d = 1.2$ T than in the yoke, which is computed as $B_Y = 0.9$ T.

3.2.2 Rotor Eddy-Current Losses

The air gap flux-density distribution along the rotor surface circumference consists of a fundamental and of higher harmonic components, caused by stator slotting and rotor slitting with ordinal numbers -13, 15, -17, 19 (Fig. 3.3). Although the time variation of the stator voltage and current, supplied to the FEM model through coupling circuit, are sinusoidal, the spatial distribution of flux density in the air gap is not. The space distribution of the flux density is independent of the time variation of the feeding winding currents. It depends only on winding arrangements in the slots and on the rotor geometry. The *Fourier* analysis of the stator air gap field of a 3-phase stator winding, distributed in 36 stator slots, fed by a sinusoidal time variation 3-phase stator current system with $2\pi/3$ radians phase shifts, with an amplitude of I_{\max} and frequency f_s , yields an air-gap flux density distribution $B_{\delta,s}(x_s, t)$, which can be represented by an infinite sum of sinusoidal spatial flux density waves (Fig. 3.3b). The sinusoidal time changing rotor current I_r , flowing along the ‘rotor teeth’ in parallel with the rotational axis, is exciting also a non-sinusoidal distributed air gap flux density distribution $B_{\delta,r}(x_s, t)$, which can also be represented by an infinite sum of sinusoidal space-distributed flux density waves. These flux pulsations due to the stator slot openings and rotor slitting cause rotor eddy current losses [11], [31]. The rotor eddy current losses $P_{\text{Ft,r}}$ consist of the fundamental component $P_{\text{Ft,r1}}$, which depends on the rotor frequency $f_r = s \cdot f_s$, and of the high-frequency eddy current losses $P_{\text{Ft,r,ad}}$, due to slotting [20]. These rotor eddy current losses are numerically computed with a time stepping FEM simulation, using (3.28) [20], [49].

$$P_{\text{Ft,r}} = \int_V \rho \cdot J_{\text{Ft}}^2 dV, \quad (\rho = 1/\kappa), \quad (3.28)$$

$$P_{\text{Ft,r}} = P_{\text{Ft,r,l}} + P_{\text{Ft,r,d}}, \quad (3.29)$$

where ρ in (3.28) is specific electrical resistance of the rotor steel. The calculation was done with the FEM program code FLUX 2D.

The total eddy current loss density in the rotor is separated into the high value beneath the rotor surface with a penetration depth of d_E , which is designated as $P_{\text{Ft,r,d}_E}$. The penetration value d_E is calculated numerically as shown on the FEM computation result Fig. 3.4. The second part of eddy current losses is considered within the rotor teeth $P_{\text{Ft,r,d}}$ and the third one within the rotor yoke $P_{\text{Ft,r,Y}}$. So the total rotor eddy current losses within the rotor iron body are:

$$P_{\text{Ft,r}} = P_{\text{Ft,r,d}_E} + P_{\text{Ft,r,d}} + P_{\text{Ft,r,Y}} \quad (3.30)$$

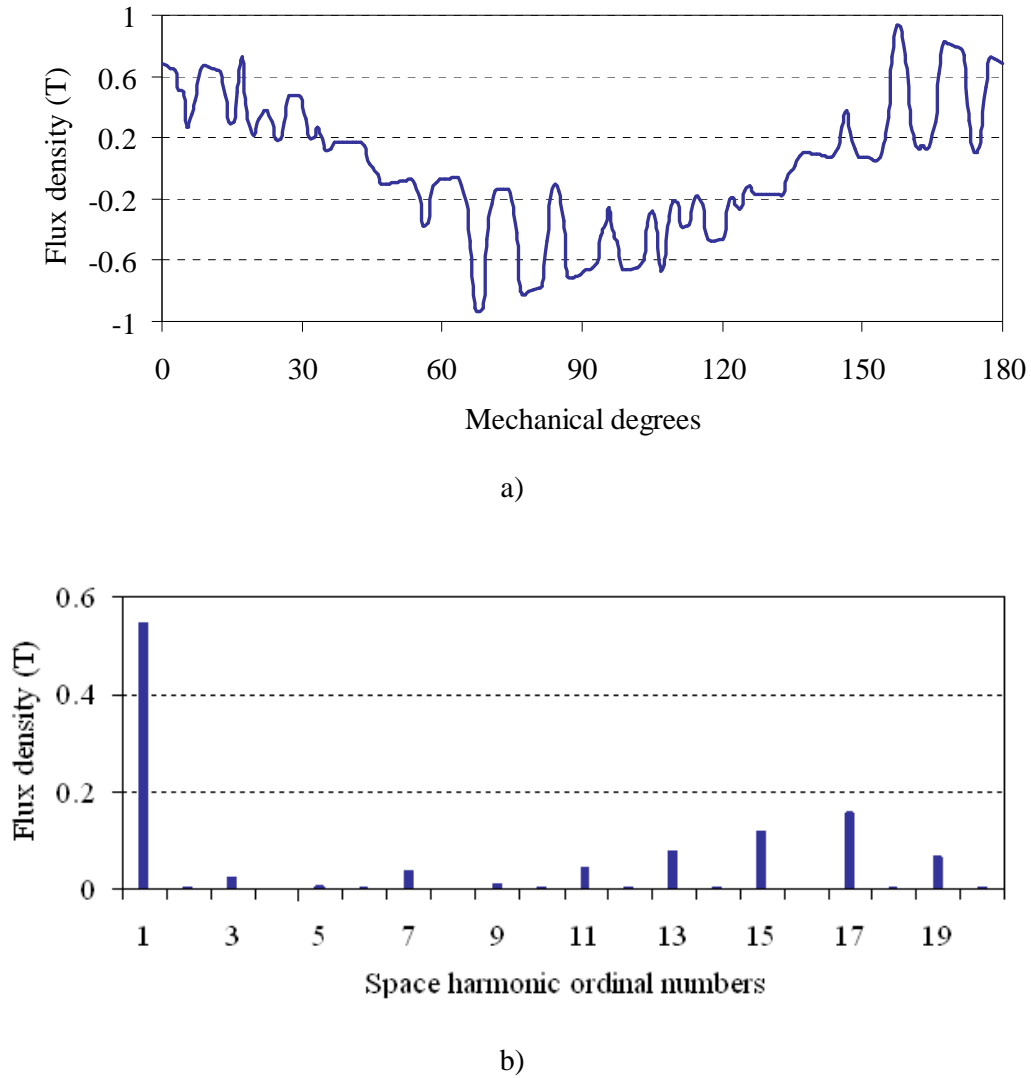


Figure 3.3: Time stepping computed air-gap field solution of the 4-pole SRIM at an operating slip of $s = 1.8\%$, line-to-line voltage $U_s = 330$ V, Y, $f_s = 800$ Hz, $I_s = 82$ A, $h_{\text{slit}} = 19$ mm, $w_{\text{slit}} = 2.5$ mm, $\vartheta_{\text{rotor}} = 200$ °C: a) radial component of the air-gap flux density, b) harmonic spectrum of a).

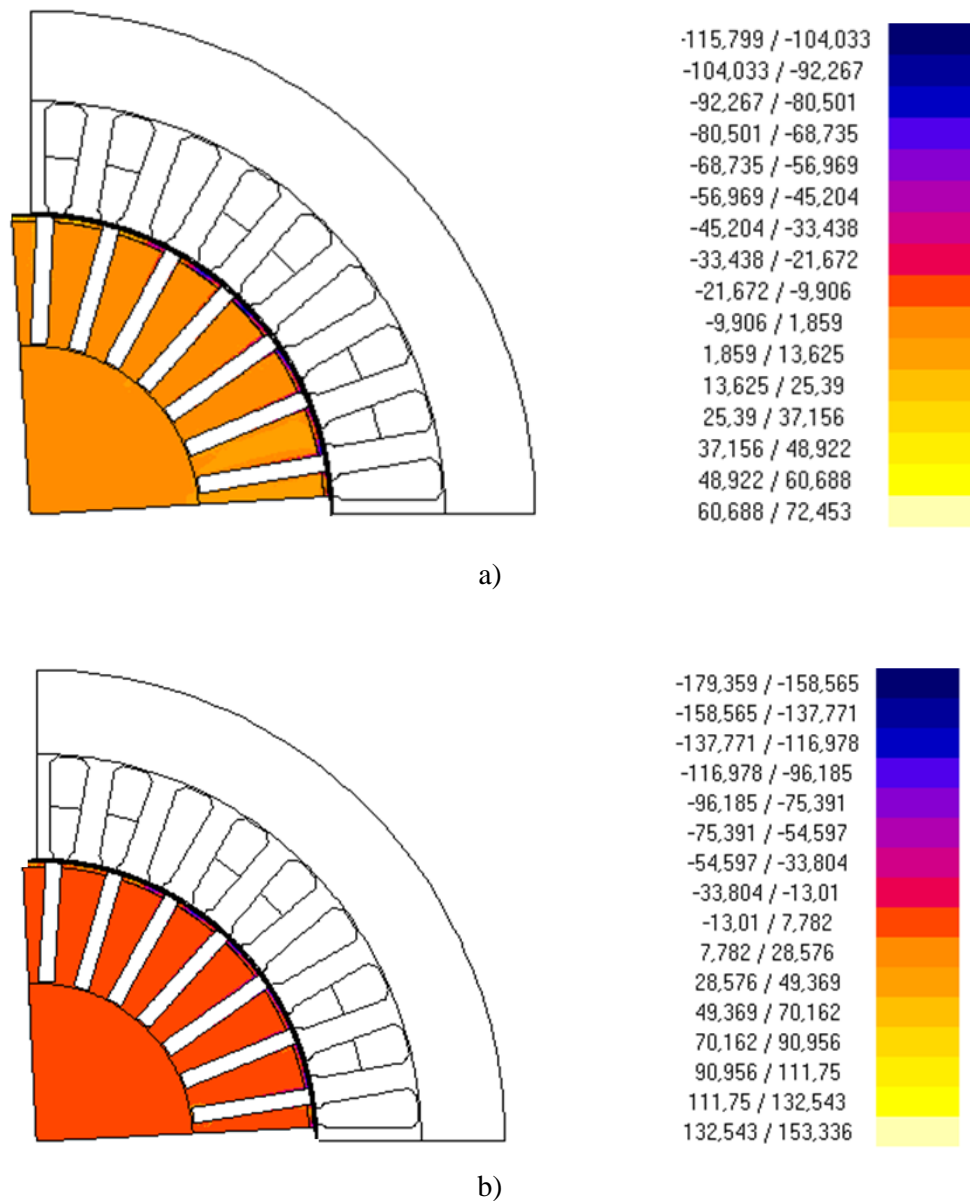


Figure 3.4: Time stepping FEM computed rotor eddy current density distribution of the axially slitted 4-pole SRIM with copper end-rings for different operating frequencies (A/mm^2) a) for 400 Hz, b) for 800Hz.

Table 3.4: Computed rotor eddy current losses due to the fundamental field wave and due to the stator slotting influence of the 4-pole SRIM at the rotor temperature $\vartheta_{\text{Rotor}} = 200\text{ }^{\circ}\text{C}$, and generated torque $M_e = 12\text{ Nm}$

f / Hz	U_{Ph} / V	$s / \%$	I_S / A	$P_{\text{Ft,r,d}_E} / \text{W}$	$P_{\text{Ft,r,d}} / \text{W}$	$P_{\text{Ft,r,Y}} / \text{W}$	$P_{\text{Ft,r}} / \text{W}$
800	191	1.8	83.8	2102	612	72	2786
600	143	2.4	84.4	1564	590	73	2227
400	95	3.6	84.9	981	574	74	1629

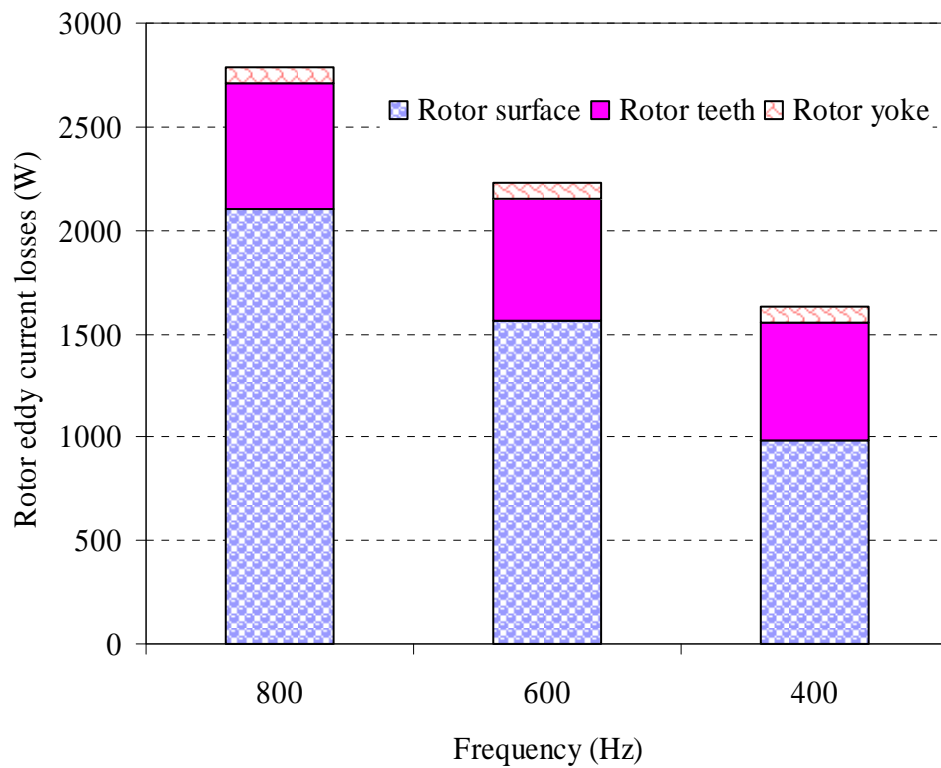


Figure 3.5: Rotor eddy current loss distributions of the 4-pole axially slitted SRIM with copper end-rings for different rotor parts i.e. at the rotor surface within the skin depth d_E , within the rotor teeth and in the rotor yoke.

It is seen, that in high speed solid rotor induction motors the rotor eddy current losses are high, which constitute up to 40 % of the total motor losses and are mainly concentrated on the rotor surface skin depth d_E . For the analysed 4-pole SRIM, the rotor eddy current losses within the rotor skin depth d_E are found to be $P_{F_{t,r,d_E}} / P_{F_{t,r}} = 80 \%$, 70% and 60% of the total rotor eddy current losses for 800 Hz, 600 Hz and 400 Hz operating frequencies respectively, as given in Table 3.4.

3.3 Rotor Radial Grooves

The high rotor losses cause a sharp increase in the rotor temperature, which greatly affects the life span of the high speed ball bearings, which are designed for a maximum operating temperature up to $110 \text{ }^\circ\text{C}$. One way of decreasing the rotor losses and hence limiting its temperature rise is making radial grooves on the rotor surface, and thereby cutting the path of high frequency harmonic currents [28], [38].

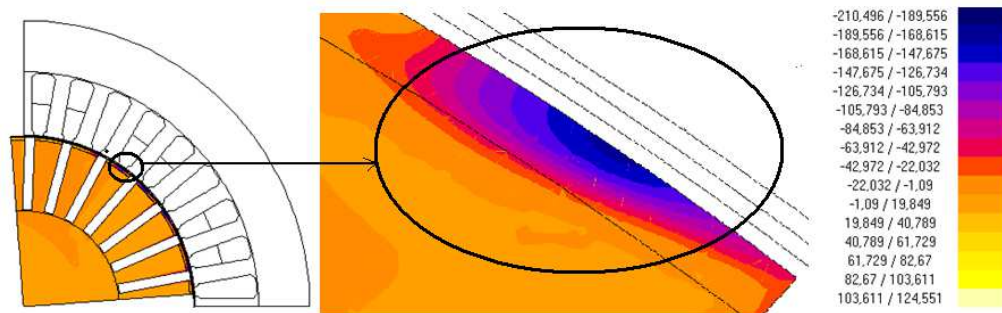


Figure 3.6: 4-pole axially slitted solid rotor induction motor FEM computed rotor eddy current density in A/mm^2 at stator supply frequency $f_s = 600 \text{ Hz}$, $U_s = 248 \text{ V}$, and slip = 2.4% .

The FEM results of the rotor current distribution show that the high frequency rotor eddy currents are occurring mainly beneath the surface (Fig.3.6). From the computed penetration depth, radial rotor grooves with a width of $a = 0.5 \text{ mm}$, a depth of $c = 0.7 \text{ mm}$ and $b = 2.5 \text{ mm}$ distance between grooves was designed and constructed, as shown in the Fig. 3.7. It is visible from the air-gap field distribution

(Fig.3.3) that the dominant higher space harmonics are with ordinal numbers $\nu = -17$ and 19, which are the slot harmonics of the stator slots. According to *Russell* [45] the rotor ends can be taken into account in the 2D computation by decreasing the electrical conductivity of the rotor core material by the average equivalent *Russell* end-effect factor $k_{R,eq}$ as in (3.31). This equivalent end-effect factor includes the effect of fundamental air-gap field ($k_{R,\nu=1}$), given by (3.33), and higher harmonic fields ($k_{R,\nu}$) (3.36), which are penetrating into the grooved area. Accordingly, for the rotor surface, the resistivity is corrected, using the *Russell* end-effect factor in the grooved iron parts, where mainly higher frequency harmonic currents flow, which would be equivalent with the reduction of the surface iron conductivity by 90 % as calculated in (3.31). Accordingly, applying only 10 % iron conductivity for the penetration depth area (0.7 mm deep), the rotor eddy current losses beneath the outer surface decreased significantly by 75 % for 400 Hz, 70 % for 600 Hz and 65 % for 800 Hz operating frequencies.

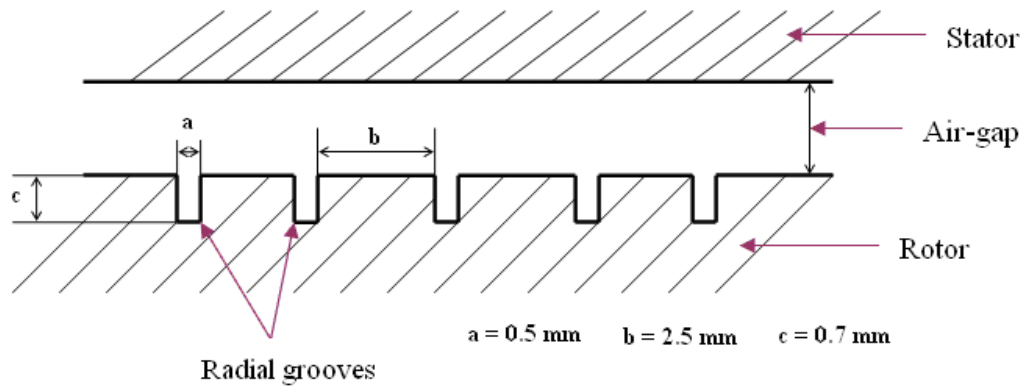


Figure 3.7: Designed radial grooves on the rotor surface which have 0.7 mm deep, 0.5 mm width and 2.5 mm between each grooves.

$$k_{R,eq} = \frac{k_{R,v=1} + k_{R,v}}{2}, \quad (3.31)$$

$$k_{R,v=1} = 1 - \frac{2 \cdot \tau_p}{\pi \cdot l} \tanh\left(\frac{\pi \cdot l}{2 \cdot \tau_p}\right), \quad (3.32)$$

$$k_{R,v=1} = 1 - \frac{2 \cdot 69.7}{\pi \cdot 2.5} \tanh\left(\frac{\pi \cdot 2.5}{2 \cdot 69.7}\right) = 0.0011 \quad (3.33)$$

$$k_{R,v} = 1 - \frac{2 \cdot \tau_{pv}}{\pi \cdot l} \tanh\left(\frac{\pi \cdot l}{2 \cdot \tau_{pv}}\right), \quad (3.34)$$

$$\tau_{pv} = \frac{\tau_p}{v_{av}} = \frac{69.7}{18} = 3.87 \text{ mm}, \quad v_{av} = \frac{|-17| + 19}{2} = 18, \quad (3.35)$$

$$k_{R,v} = 1 - \frac{2 \cdot 3.87}{\pi \cdot 2.5} \tanh\left(\frac{\pi \cdot 2.5}{2 \cdot 3.87}\right) = 0.24 \quad (3.36)$$

In the previous equation, τ_p is the pole-pitch for the fundamental field, l is the distance b distance between the radial grooves, which is taken as an iron length path for high frequency harmonic currents, and τ_{pv} is the average pole pitch of the stator slot harmonic fields. Applying the modified end effect factor for the rotor surface conductivities in the region of the penetration depth $d_E \approx 0.7$ mm, the following time stepping FEM computation results are obtained, which are presented in Table 3.4, Table 3.5 and Table 3.6. It is seen that by implementing the rotor radial surface grooves, the rotor eddy current losses at the rotor surface are drastically decreased (up to 70 %) at nominal speed with 800 Hz operating frequency in comparison to that of the motor without radial grooves with the same electromagnetic torque, as shown in the Fig. 3.8.

Table 3.5: Analytically calculated stator winding fundamental and additional copper losses of the 4-pole SRIM at a stator winding temperature $\vartheta_{\text{Cu,s}} = 100\text{ }^{\circ}\text{C}$, $R_{\text{s},20} = 0.024\ \Omega$ and a generated electromagnetic torque $M_e = 12\text{ Nm}$ with radial grooves on the rotor surface

f / Hz	U_{ph} / V	$s / \%$	I_s / A	$P_{\text{Cu,s}} / \text{W}$	$P_{\text{Cu,Ft,a}} / \text{W}$	$P_{\text{Cu,Ft,b}} / \text{W}$	$P_{\text{Cu,Ft,ad}} / P_{\text{Cu,s}}$
800	191	1.8	81.1	631	12.6	22.7	0.06
600	143	2.4	81.4	636	4.59	13.4	0.03
400	95	3.6	81.8	642	3.2	10.3	0.02

Table 3.6: Stator core losses of the 4-pole SRIM at a stator winding temperature $\vartheta_{\text{Rotor}} = 200\text{ }^{\circ}\text{C}$, and a generated torque $M_e = 12\text{ Nm}$ with radial rotor surface grooves

f / Hz	U_{ph} / V	$s / \%$	I_s / A	$P_{\text{Fe,y}} / \text{W}$	$P_{\text{Fe,d}} / \text{W}$	$P_{\text{Fe,s}} / \text{W}$
800	191	1.8	81.2	324	485	809
600	143	2.4	81.4	198	294	492
400	95	3.6	81.8	100	144	244

Table 3.7: Computed rotor fundamental and harmonic rotor eddy current losses of the 4-pole SRIM at the rotor temperature of $\vartheta_{\text{Rotor}} = 200^\circ\text{C}$, and generated torque $M_e = 12\text{Nm}$ with radial grooves on the rotor surface

f / Hz	U_{ph} / V	$s / \%$	I_s / A	$P_{\text{Ft,r,d}_E} / \text{W}$	$P_{\text{Ft,r,d}} / \text{W}$	$P_{\text{Ft,r,Y}} / \text{W}$	$P_{\text{Fe,r}} / \text{W}$
800	191	1.8	81.1	656	640	73	1369
600	143	2.4	81.4	428	626	73	1127
400	95	3.6	81.8	221	608	74	903

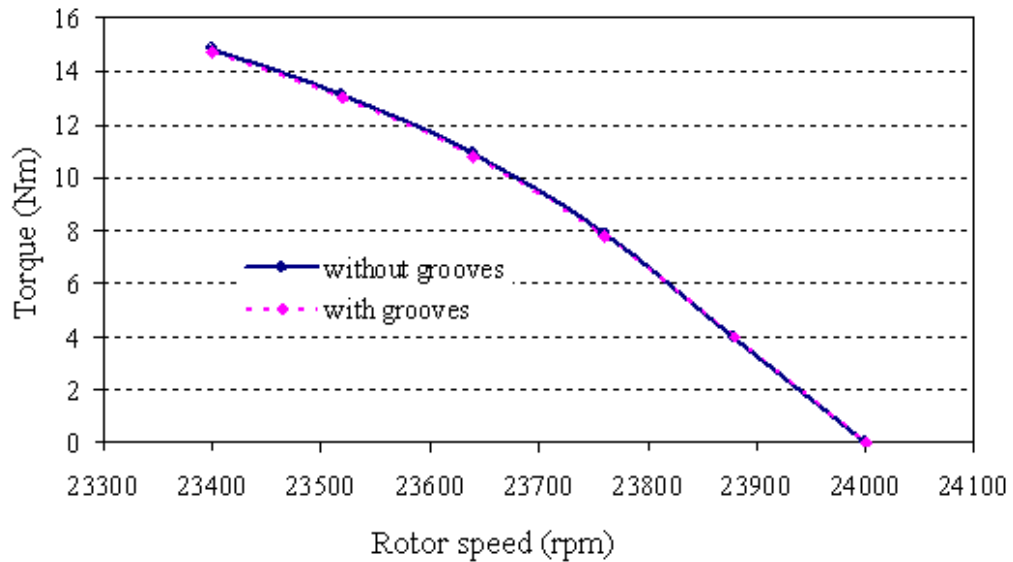


Figure 3.8: Comparison of the torque-speed-curve of the 4-pole SRIM with and without rotor radial grooves in the rotor surface.

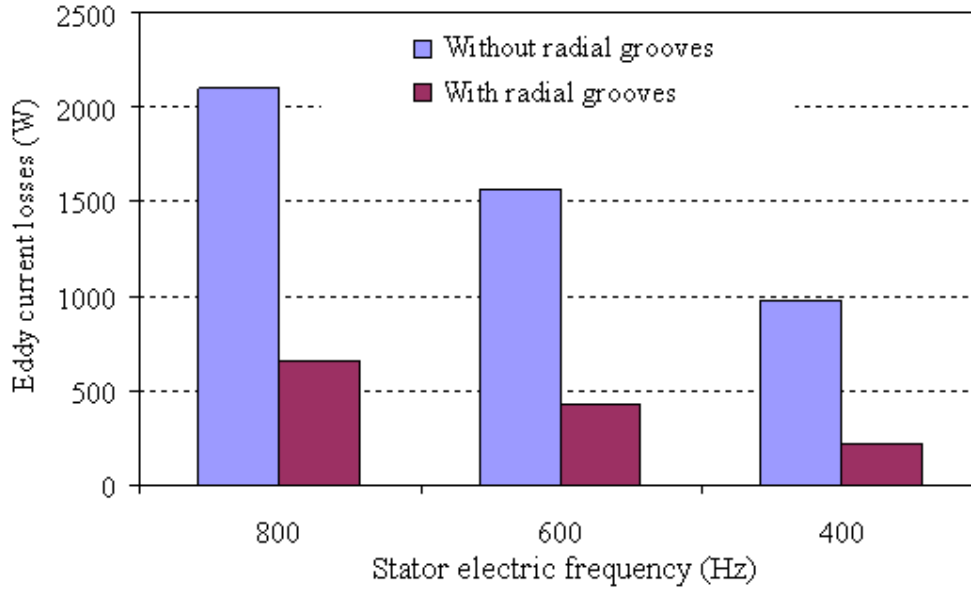


Figure 3.9: Comparison of the rotor eddy current losses at the rotor surface $P_{Fl,r,dE}$, where the high frequency rotor eddy currents flow within the penetration depth.

3.4 Rotor End Rings Copper Losses

Electrical joule losses on the rotor copper end-rings resistance R_{er} caused by the current flow in each ring $I_{er} = 607$ A given as in (2.34) were determined to be 37W as per (3.37).

$$P_{Cu,er} = 2 \cdot I_{er}^2 \cdot R_{er} \quad (3.37)$$

The end-ring resistance R_{er} was calculated using the geometry and the electrical conductivity of the ring at the operating temperature $\vartheta_{Rotor}^{\circ} = 200$ °C as in (3.38).

$$R_{er} = \frac{\pi \cdot D_{er}}{\kappa \cdot A_{er}} = \frac{\pi \cdot 88.8 \cdot 10^{-3}}{33 \cdot 169} = 50 \mu\Omega \quad (3.38)$$

3.5 Mechanical Losses

The mechanical losses include air friction (*windage*) and bearing friction losses. They occur due to air-gap friction and the friction in the bearings and are calculated analytically. At high speed operation, these losses constitute a large portion (about 20 %) of the total losses [26], [47], [48]. Hence, a careful estimation is vital to limit the total rotor losses, which affect its temperature rise and the total operating efficiency of the motor.

3.5.1 Air Friction Losses

The air friction losses in the air-gap of the motor are estimated by semi-empirical formulas, given in [26], [48] for rotating cylinders in enclosures like the stator bore, which is also the case for rotating electrical machines. The air-friction (*windage*) losses at high speed operation are caused by the shear stress τ_s of the turbulent air flow given in (3.39).

$$\tau_s = C_T \cdot \frac{\rho_{\text{air}} \cdot (\omega_m \cdot r_a)^2}{2}, \quad (3.39)$$

Hence, the air friction power P_w associated with the resisting drag torque of a rotating cylinder is given by (3.38).

$$P_{w, \text{enclosure}} = k_1 \cdot C_T \cdot \pi \cdot \rho_{\text{air}} \cdot \omega_m^3 \cdot r_a^4 \cdot l_{\text{Fe}}, \quad \omega_m = 2 \cdot \pi \cdot n \quad (3.40)$$

In (3.38) k_1 is the roughness coefficient ($k_1 = 1$ for smooth surfaces, $k_1 = 2.5$ for axially slitted surfaces [1]), C_T is the friction torque coefficient calculated by (3.41), ρ is the mass density of the fluid ($\rho_{\text{air}} = 0.83 \text{ kg/m}^3$ at 150°C), ω_m is the angular mechanical velocity and r_a is outer radius of the rotor. When a cylinder is rotating in free space like at the rotor ends, one way to determine the nature of the

tangential gas flow, exerted by the rotating cylinder, is to use the *tip-Reynolds* number as in (3.42) [47].

$$C_T = 0.035 \cdot R_e^{-0.15} \quad (3.41)$$

$$R_{ct} = \frac{\rho \cdot \omega_m \cdot r_a^2}{\mu} \quad (3.42)$$

In order to take the effect of the enclosure by the stator bore into account, the radial air-gap length δ has to be included in the *Reynolds* number as given in (3.43) [47],

$$R_{e\delta} = \frac{\rho \cdot \omega_m \cdot r_a \cdot \delta}{\mu}, \quad (3.43)$$

where μ is the dynamic viscosity of the fluid ($\mu = \rho \cdot \nu$), δ is the radial air-gap length and ν is the kinematic viscosity of the fluid ($\nu = 28.8 \cdot 10^{-6} \text{ m}^2/\text{s}$ for air at 150 °C). The end sides of the rotor do also have friction losses. The nature of the tangential flow is determined with the tip *Reynolds* number. The friction losses at the rotor end, which are the power needed to rotate end bodies, are determined by in (3.44) as indicated in [58],

$$P_{w,\text{end}} = \frac{1}{2} C_{T,\text{end}} \cdot \rho \cdot \omega^3 \cdot (r_a^5 - r_i^5), \quad (3.44)$$

where r_a and r_i are the outer and inner radii of the end rings respectively. In the studied solid rotor motors, the free space for the rotor ends in the end-winding area is typically large, hence the rotor ends act like a centrifugal pump. When the rotor end is assumed to rotate in free space, the torque coefficient $C_{T,\text{end}}$ is given by (3.45).

$$C_{T,\text{end}} = \frac{3.87}{R_{et}} \quad (3.45)$$

Hence, the total air friction losses are the sum of the air-gap air friction (3.38) and the rotor end air friction losses (3.42).

$$P_w = P_{w, \text{enclosure}} + 2 \cdot P_{w, \text{End}} \quad (3.46)$$

Table 3.8: Computed rotor air-friction losses of the 4-pole SRIM at a rotor temperature of $\vartheta_{\text{Rotor}} = 200^\circ\text{C}$

f / Hz	$n_{\text{syn}} / \text{min}^{-1}$	$s / \%$	I_s / A	$P_{w, \text{enclosure}} / \text{W}$	$P_{w, \text{End}} / \text{W}$	P_w / W
800	24000	1.8	81.2	381.2	11.4	392.6
600	18000	2.4	81.7	164.9	5.5	170.4
400	12000	3.6	82.1	50.1	1.9	52.0

3.5.2 Bearing Friction Losses

The bearing friction losses P_{fr} , which are caused by a friction torque M_b , for the drive end and non-drive end oil-lubricated high speed spindle ball bearings type *SKF 71906 CD* with contact angle 15° ($d_b = 30$ mm, $D_b = 47$ mm, $b_b = 9$ mm) are determined as in [33].

$$P_{\text{fr}} = 2 \cdot M_b \cdot \omega_m \quad (3.47)$$

The total bearing friction torque of the implemented high speed bearings can be roughly determined using (3.48) under the following conditions: mean bearing load $P/C \approx 0.1$ (dynamic load / nominal load), viscosity ratio $\nu_b / \nu \approx 1$ (kinematic viscosity / reference viscosity), with average speed range and predominant radial

load [33].

$$M_b = \mu_b \cdot \sqrt{F_r^2 + F_a^2} \cdot d_b / 2, \quad (3.48)$$

where μ_b is the bearing rolling friction coefficient, which can be assumed to be 0.002 as per [52], F_r is the radial bearing force determined by the gravitational force ($F_r = m_r \cdot g = 6.1 \cdot 9.8 = 60$ N: with $m_r = 6.1$ kg is the rotor mass and $g = 9.8$ m/s² is the gravity), F_a is axial bearing force, which determines the total tension on against the bearing inner ring. It is approximated to be equal to 283 N for the given bearing type [52] and d_b is the bearing inner bore diameter. The rough bearing torque calculation using (3.48) delivers low values as per the investigation made by [33]. For high speed machines, therefore a detailed bearing loss analysis has to be made as follows. The bearing friction torque M_b consists of components i.e. a speed and viscosity dependent part M_{b0} and a load dependent part M_{b1} .

$$M_b = M_{b0} + M_{b1} \quad (3.49)$$

$$M_{b0} = f_0 \cdot 10^{-10} \cdot (\nu_b \cdot n)^{2/3} \cdot d_{bm}^3 \quad (3.50)$$

In (3.50) the coefficient $f_0 = 1.75$ is a factor, which depends on the type of bearing construction and lubrication method, $\nu_b = 4.5$ mm²/s at 150 °C is the kinematic viscosity of the lubricant oil and $d_{b,av} = (D_b + d_b)/2$ is average diameter of the bearings with the outer bearing diameter $D_b = 47$ mm and the inner bearing diameter $d_b = 30$ mm.

$$M_{b1} = f_1 \cdot P_1 \cdot d_{bm}, \quad (3.51)$$

$$f_1 = 0.0007 \cdot (P/C_0)^{0.5}, \quad (3.52)$$

$$P = 1.3F_a + 0.44F_r, \quad (3.53)$$

$$P_1 = 3.3F_a - 0.1F_r. \quad (3.54)$$

The torque M_{b1} is determined by the rated static load $C_0 = 4550$ N and the axial and radial bearing forces $F_a = 283$ N and $F_r = 60$ N. The bearing friction losses in the machines are calculated then using (3.55)

$$P_{fr} = 2 \cdot (M_{bo} + M_{b1}) \cdot \omega_m \quad (3.55)$$

$$P_{fr+w} = P_{fr} + P_w \quad (3.56)$$

Table 3.9: Analytically calculated bearing-friction and total mechanical losses of the 4-pole SRIM at the rotor temperature of $\vartheta_{Rotor} = 200$ °C

f / Hz	$n_{syn} / \text{min}^{-1}$	$s / \%$	I_s / A	P_{fr} / W	P_w / W	P_{fr+w} / W
800	24000	1.8	81.2	148	393	541
600	18000	2.4	81.7	96	170	266
400	12000	3.6	82.1	52	52	104

It is observed that, the total mechanical losses P_{fr+w} given in (3.53), for the optimized 4-pole axially slitted, radial grooved SRIM constitute 20 %, 15 %, 10 % of the total motor losses for the operating frequencies of 800, 600 and 400 Hz respectively, which are in line with the studies made in the literatures [26], [47], [48].

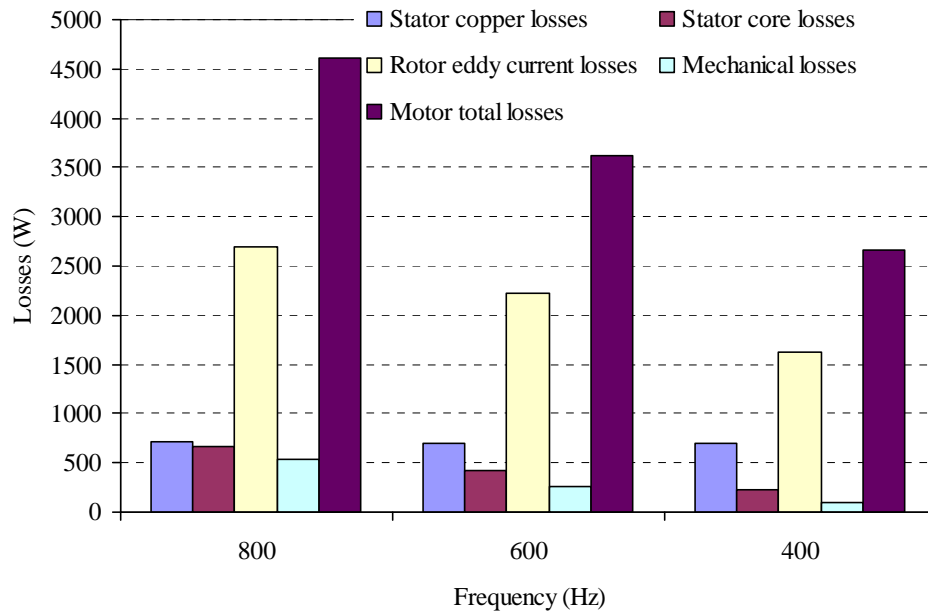


Figure 3.10: Comparison of calculated 4-pole motor losses for different operating frequencies; rotor surface without radial grooves, operation at an electromagnetic torque $M_{em} = 12$ Nm.

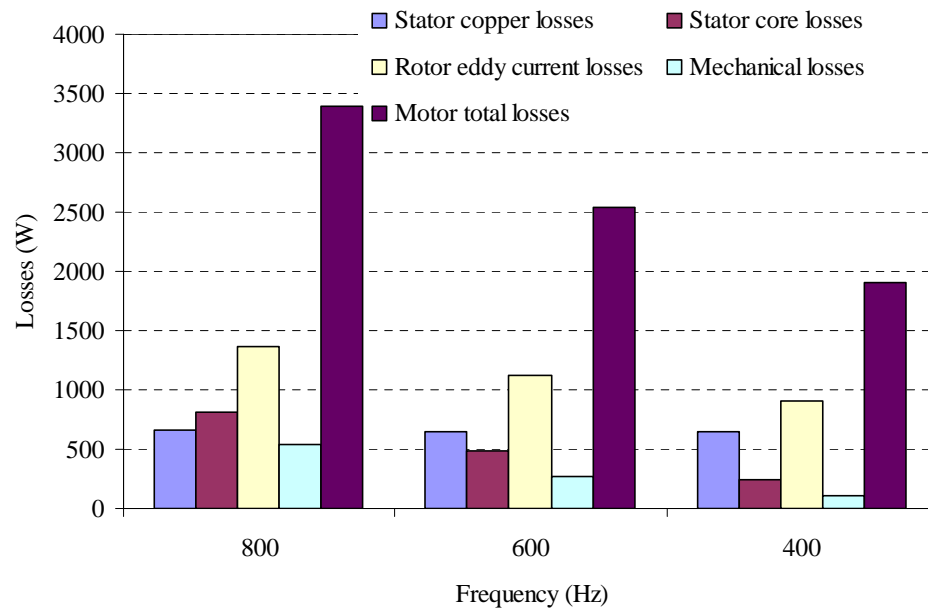


Figure 3.11: Comparison of calculated 4-pole motor losses for different operating frequencies; rotor outer surface with radial grooves operation at $M_{em} = 12$ Nm.

4 Electromagnetic Design and Analysis of a 2-pole SRIM

It is seen in Chapter 3, section 3.2.2, that the rotor magnetic losses, mainly the fundamental and higher harmonic eddy current losses are high, which increases the rotor heating and results in poor operating efficiency [47]. For high speed solid rotor induction motors the supply frequency is so high i.e. 800 Hz for the 4-pole machine to get the rated speed $n_{\text{syn}} = 24000 / \text{min}$. Half stator frequency and hence less stator and rotor core losses can be achieved by implementing a 2-pole solid rotor machine [65]. Therefore, in the following a 2-pole SRIM is investigated.

4.1 Two-pole SRIM contra 4-pole SRIM

For a 2-pole machine the magnetising reactance increases by a factor 2, which improves the power factor significantly. The improvement in the power factor results in a decreased level of the no-load magnetising current and thereby also in a decrease of the full load current, which then decreases the stator winding copper losses. The hysteresis component of core losses varies nearly linear with frequency and the eddy current loss component varies with the square of the stator frequency. Therefore, for a 2-pole SRIM, with half operating frequency for the given speed ($n_{\text{syn}} = 24000 / \text{min}$), the total core losses are decreased. However, an increased mass of the lamination steel is necessary due to the bigger cross-section for the increased return flux paths, so somehow this counteracts the improvement expected from reducing the operating frequency. The rotor fundamental and harmonic eddy current losses are less for the 2-pole machine due to a smaller rotor fundamental slip frequency. The other advantage is that in the 2-pole configuration the leakage fluxes are less in comparison to the main flux, resulting in a smaller leakage coefficient and an increased overload capability of the motor, which is determined by the

maximum possible breakdown torque.

4.2 Electromagnetic Design of a 2-pole SRIM

The electromagnetic design of a 2-pole SRIM includes the design of the stator core and the stator winding for an operating frequency ($f = 400$ Hz), which is half the value for the 4-pole design, with the same axially slitted, radially grooved solid rotor, which was already designed and optimized in Chapter 2 for the 4-pole SRIM.

4.2.1 Stator Core Design

The flux per pole for a 2-pole machine is two times of that of a 4-pole machine. This is directly linked with a necessary increase of the return flux path cross-section in the stator yoke. These yoke paths have to carry each one half of the flux per pole. Hence, to keep the induction constant the stator must be constructed with double height of the stator yoke Fig. 4.1b. However the increased height of the stator yoke leads to a thicker (bigger) machine and to bigger stator copper losses due to the twice longer winding overhang length. Accordingly, keeping the inner diameter and iron length as in case of the 4-pole machine, the stator yoke height is doubled. This allows due to the same stator bore the implementation of the same optimized axially slitted, radially grooved solid rotor (Fig. 4.1) as in the design of the 4-pole SRIM.

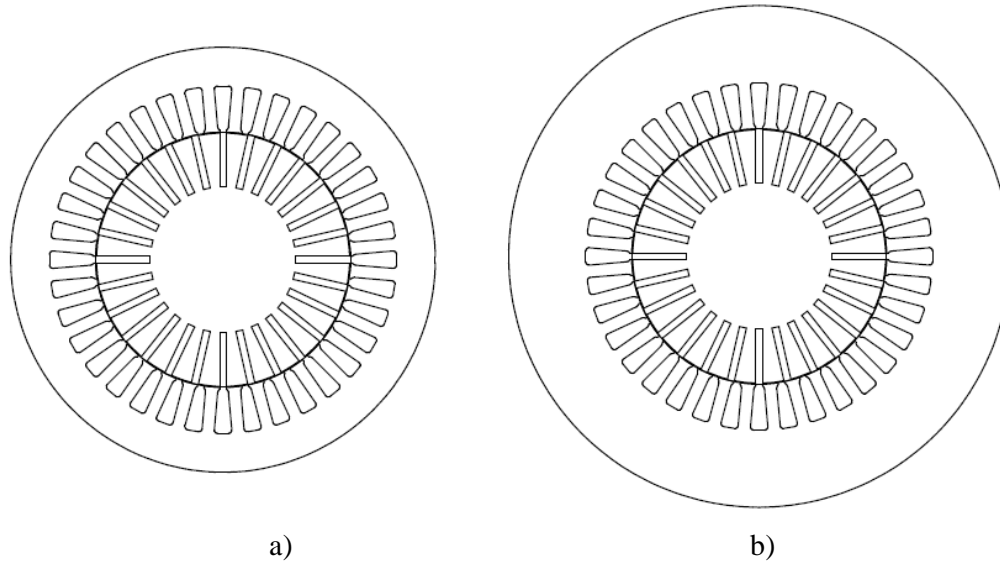


Figure 4.1 Construction models a) for a 4-pole and b) for a 2-pole SRIM for the same air-gap flux density and the same rotor.

Table 4.1 : Basic design data of a 2-pole, 30 kW SRIM, 330V, Y in comparison with a 4-pole SRIM

Machine	$2p = 4$	$2p = 2$
Stator frequency (Hz)	800	400
Stator outer / inner diameter (mm)	150 / 90	177 / 90
Air gap / stator slot opening (mm)	0.6 / 2.3	0.6 / 2.3
Stack length (mm)	90	90
Number of stator slots / rotor slits	36 / 28	36 / 28
Turns per coil / Turns per phase	8 / 24	4 / 24

4.2.2 Stator Winding Design

The three phase two-layer integer slot stator winding with q slots per pole and phase is made of round wire with a_i parallel conductors per turn and a_a parallel branches per phase with a coil pitch W / τ_p (Table 4.2). It comprises of N_c turns per

coil and N_s turns per phase as it is given in (4.1). The overhang length l_b and the stator core length l_{Fe} give together with the round wire diameter d_{Cu} the resulting DC resistance R_s .

$$N_s = 2p \cdot q \cdot N_c / a_a \quad (4.1)$$

Table 4.2: Winding data of the 2-pole SRIM compared with data of the 4-pole SRIM

Machine with pole count:	$2p = 4$	$2p = 2$
Chording W / τ_p	7/9	14/18 = 7/9
Slot count Q_s	36	36
Turns per coil and per phase N_c / N_s	8 / 24	4 / 24
Parallel wires and branches a_1 / a_a	3 / 4	3 / 2
Slots per pole and phase q	3	6

4.3 FEM Computation and Analysis

The electromagnetic design and analysis of the 2-pole, 400 Hz, 330V, Y, high-speed SRIM is done using a 2D time stepping FEM [13]. The encountered losses are calculated analytically using the same procedure as in case of the 4-pole SRIM described in Chapter 3. It is done using the transient magnetic computation result parameters of the current, the flux density and the eddy current losses.

4.3.1 FEM Model of a 2-pole SRIM

The stator geometry parameters, the optimized rotor geometry parameters (Table 4.1) and the winding data parameters (Table 4.2) are used to build the simulation

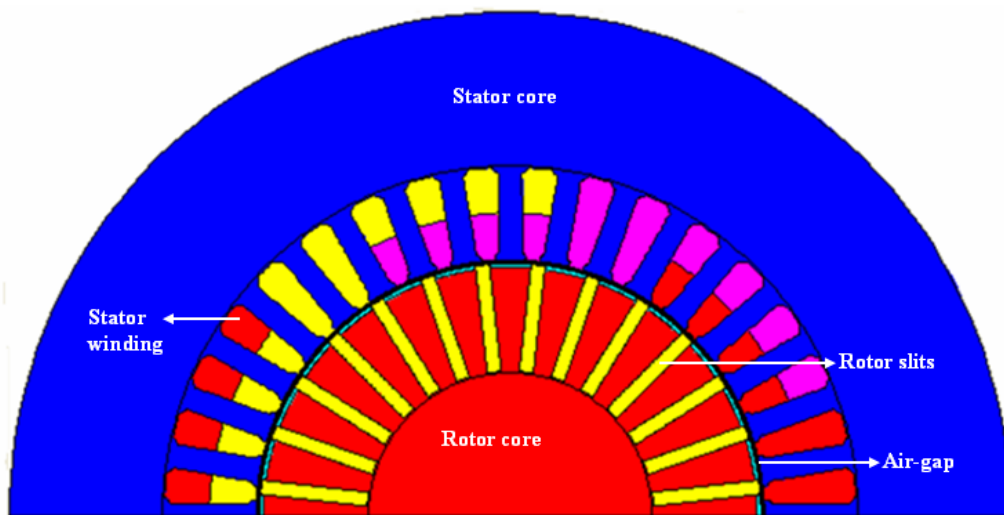
model, which is shown in Fig. 4.2. Since the analysed 2-pole SRIM is symmetrical along the pole axis, it was sufficient to model only half of the machine (Fig. 4.2a) with 52342 nodes and 25828 surface elements, as it is illustrated in Fig. 4.2b. For the computation process, the FLUX 2D solver frequency is set to 400 Hz for the nominal operating point. The electrical input parameters i.e. phase voltages, the three stator winding resistances and the end-winding leakage inductances, which are given in Table 4.3, are modelled via the coupling electrical circuit as in the case of the 4-pole SRIM shown in the Fig.2.2b.

Table 4.3: Electrical parameters of the circuit to be coupled to the FE model

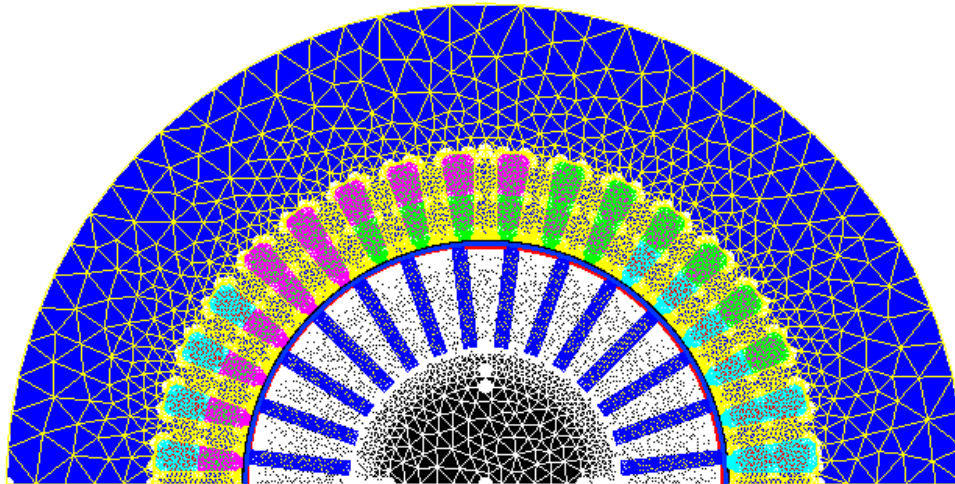
Parameter	Description	Value
R_1, R_2, R_3	Resistance of the stator winding /phase at 20 °C	0.036 Ω
L_1, L_2, L_3	Inductance of the stator winding overhang /phase as in (2.25) with $\lambda_b = 0.3$, $l_b = 230$ mm, $N_s = 24$	$1 \cdot 10^{-4}$ H

4.3.2 Transient Simulation Results

The time stepping simulation results are presented in the field distribution diagrams (Fig. 4.3 – Fig. 4.5). It is observed from the transient simulation results Fig 4.4 and Fig. 4.5, that the air-gap fields (radial and tangential components) have step-like waves, due to the stator slotting and the rotor slits.



a)



b)

Figure 4.2: Two-pole solid rotor induction motor (SRIM) FEM simulation models: a) material regions, b) model with the implemented mesh.

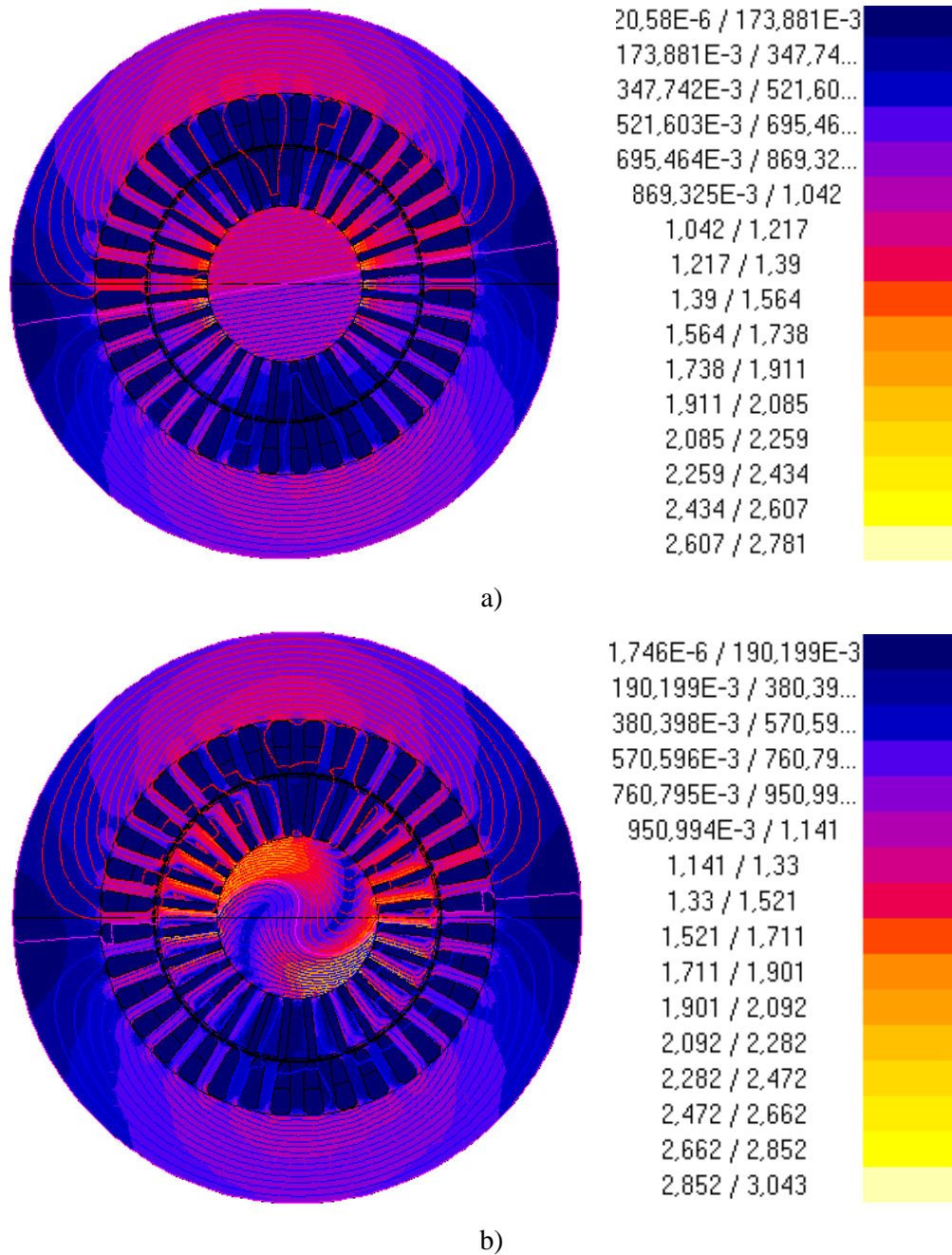
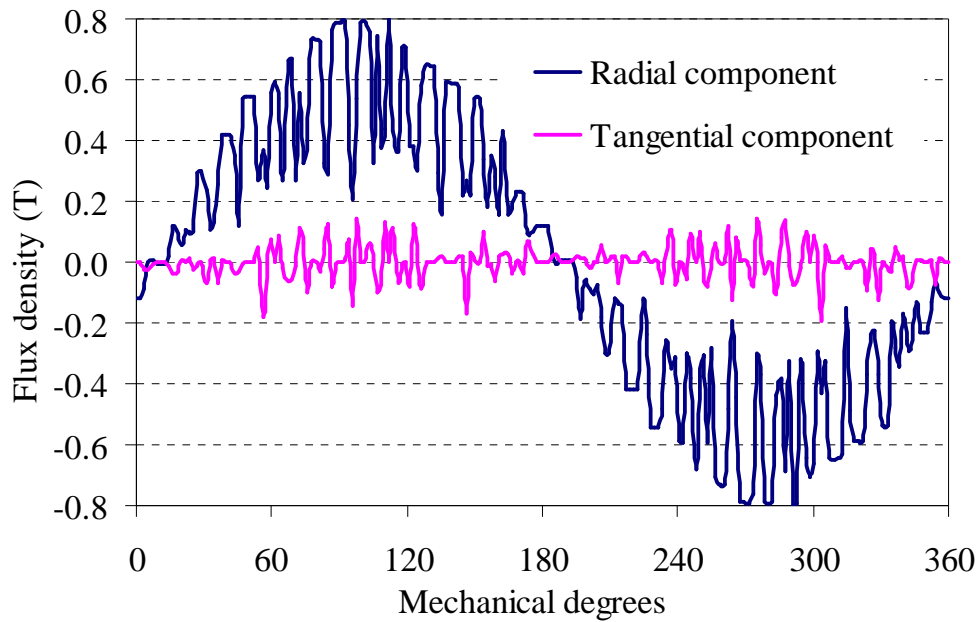
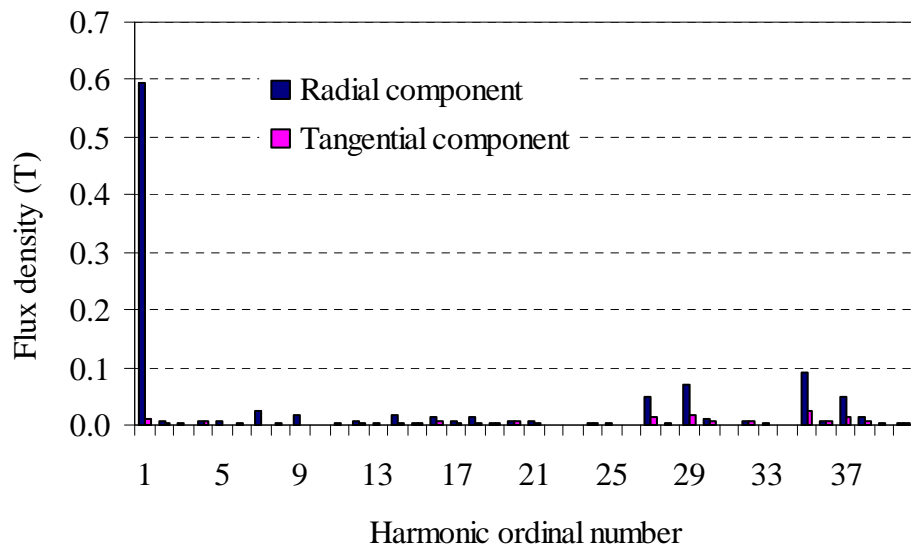


Figure 4.3: Time stepping FEM field solutions (field lines plot and magnetic flux density distribution in Tesla) of the 2-pole SRIM at the line-to-line voltage $U_s = 330$ V, $f_s = 400$ Hz, a) at no-load condition with $I_s = 19.5$ A, b) at full-load condition with $I_s = 65.8$ A.

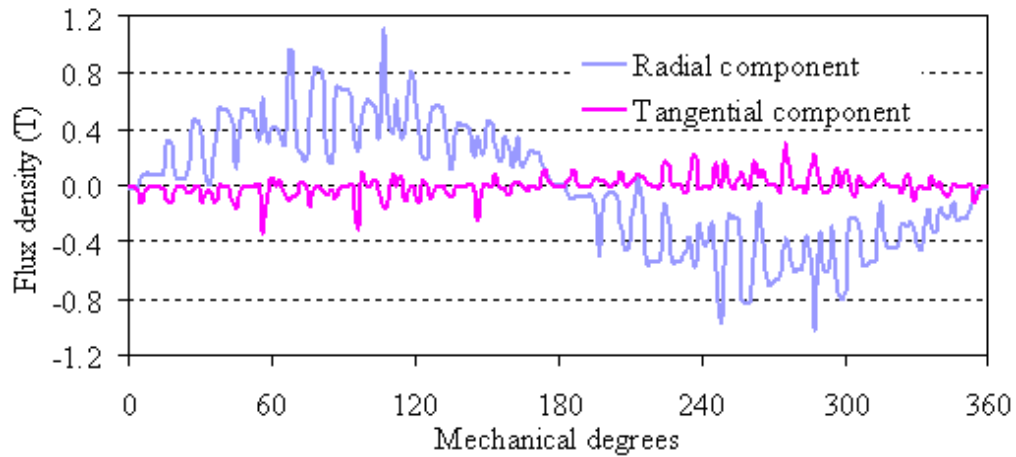


a)

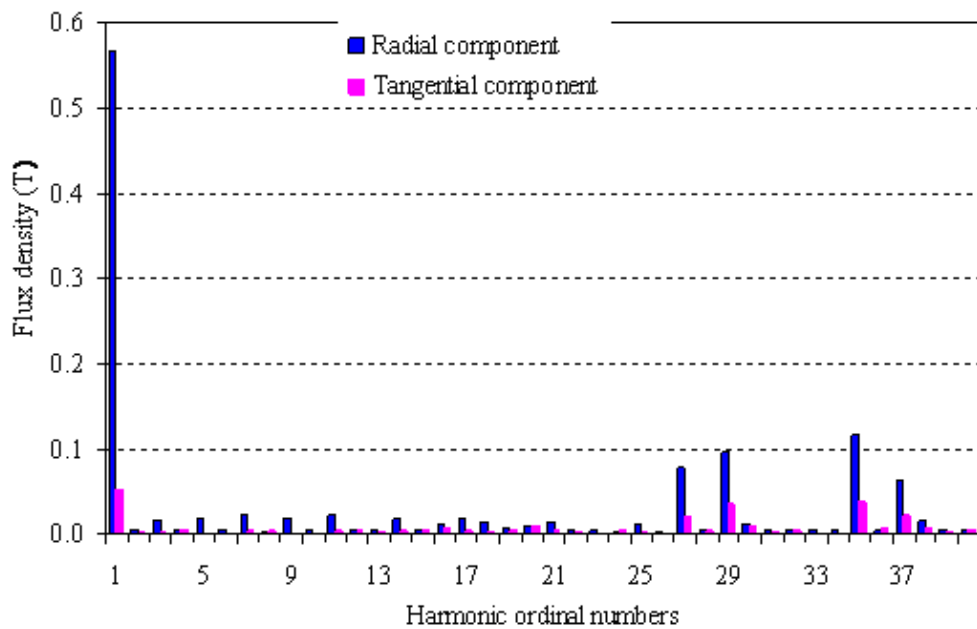


b)

Figure 4.4: Calculated radial and tangential air-gap flux density components of the 2-pole SRIM at the no-load condition with the line-to-line voltage $U_s = 330$ V, $f_s = 400$ Hz, $I_s = 19.5$ A, a) wave forms for two pole pitches, b) their harmonic spectrum.



a)



b)

Figure 4.5: Calculated radial and tangential air-gap flux density components of the 2-pole SRIM at the full-load condition with the line-to-line voltage $U_s = 330$ V, $f_s = 800$ Hz, $s = 1.9$ %, $I_s = 65.8$ A and an electromagnetic torque of $M_e = 12$ Nm, a) wave forms for two pole pitches, b) their harmonic spectrum.

The *Fourier* spectrum analysis of the fields given, in Fig. 4.4b and Fig. 4.5b, show that the dominant slot harmonics are with the ordinal numbers -27, 29, -35 and 37, which are given by (4.2) and (4.3),

$$\nu = 1 + \frac{Q_s}{p} \cdot g, \quad (4.2)$$

$$\mu = 1 + \frac{Q_r}{p} \cdot g, \quad (4.3)$$

where ν is the stator harmonic ordinal number, μ is the rotor harmonic ordinal number of the slit harmonics, Q_s is the number of stator slots, Q_r is the number of the rotor slits, p is the number of the pole pairs and g is an integer number ($g = \pm 1, \pm 2, \pm 3, \dots$). The stator higher slot harmonics field waves cause additional rotor eddy current losses, which can be computed in time stepping FEM [20], and the results are given in the following tables.

Table 4.4: Analytically calculated stator fundamental and additional copper losses of the 2-pole SRIM at the stator winding temperature $\vartheta_{\text{Cu,s}} = 100^\circ\text{C}$, $R_{\text{s},20^\circ} = 0.036 \Omega$ and an electro-magnetic torque of $M_e = 12 \text{ Nm}$

f_s / Hz	U_{Ph} / V	$s / \%$	I_s / A	$P_{\text{Cu,s}} / \text{W}$ as per (3.4)	$P_{\text{Cu,Ft,a}} / \text{W}$ as per (3.6)	$P_{\text{Cu,Ft,b}} / \text{W}$ as per (3.12)	$P_{\text{Cu,ad}} / P_{\text{Cu,s}}$
400	191	1.9	65.8	617.2	3.09	2.10	0.008
300	143	2.6	66.7	634.2	1.90	1.36	0.005
200	95	3.9	66.8	636.1	0.89	0.60	0.002

Table 4.5: Stator core losses of the 2-pole SRIM at the stator winding temperature $\vartheta_{\text{Cu,s}} = 100^\circ\text{C}$ and a load torque $M_e = 12\text{ Nm}$ with radial grooves in the rotor surface.

f_s / Hz	U_{Ph} / V	$s / \%$	I_s / A	$P_{\text{Fe,Y}} / \text{W}$	$P_{\text{Fe,d}} / \text{W}$	$P_{\text{Fe,s}} / \text{W}$
400	191	1.9	65.8	237.4	382.8	620.2
300	143	2.6	66.7	148.4	233.8	382.2
200	95	3.9	66.8	77.2	110.4	187.6

Table 4.6: Computed total rotor eddy current losses of the 2-pole SRIM at the rotor temperature $\vartheta_{\text{Rotor}} = 200^\circ\text{C}$ and a load torque $M_e = 12\text{ Nm}$, with radial grooves on the rotor surface.

f_s / Hz	U_{Ph} / V	$s / \%$	I_s / A	$P_{\text{Ft,r,d}_e} / \text{W}$	$P_{\text{Ft,r,d}} / \text{W}$	$P_{\text{Ft,r,Y}} / \text{W}$	$P_{\text{Fe,r}} / \text{W}$
400	191	1.9	65.8	394.2	578.8	135.0	1108.0
300	143	2.6	66.7	255.6	581.8	139.2	976.6
200	95	3.9	66.8	128.8	557.9	139.4	826.1

The stator winding fundamental and additional copper losses of the 2-pole SRIM are calculated analytically, using the current obtained from the magnetic transient FEM computation results. According to the results given in the Table 4.4, the additional copper losses due to the 1st and 2nd order current displacements constitute only 0.8 %, 0.5 % and 0.2 % for 400 Hz, 300 Hz and 200 Hz operating frequencies, respectively. On the other hand, the total copper losses are only about 30 % of the total motor losses, which is typical for high speed machines. The stator core losses, which depend on the operating frequency are reduced, because of low loss

lamination type M270-35A is used. But they still contain a significant percentage of about 16 % for 400 Hz operation of the total losses. From the loss calculation, it is observed that for a 2-pole high speed SRIM, the rotor eddy current losses are high in comparison with the other losses, which increases the rotor heating and endangers the life span of the bearings. For 400 Hz operation the rotor eddy current losses are 40 % of the total losses as given on Fig.4.6.

Table 4.7: Analytically calculated bearing-friction, air-friction (windage) and total mechanical losses at the rotor temperature of $\vartheta_{\text{Rotor}} = 200 \text{ }^\circ\text{C}$, and an electromagnetic air-gap torque of $M_e = 12 \text{ Nm}$.

f_s / Hz	$n_{\text{syn}} / \text{min}^{-1}$	$s / \%$	I_s / A	P_{fr} / W	P_w / W	$P_{\text{fr+w}} / \text{W}$
400	24000	1.9	65.8	147.7	390.9	538.6
300	18000	2.6	66.7	95.3	169.2	264.6
200	12000	3.9	66.8	51.9	51.5	103.5

The mechanical losses, which are highly dependent on the rotor speed, also constitute a significant portion of 20 % of the total losses at the rated operating frequency 400 Hz, which is in concordance with the study given in [59].

4.4 Comparisons of Computed Results of the 4- and 2-pole SRIM

4.4.1 Comparison of Simulations

The comparison of the 4- and 2-pole SRIM transient magnetic simulations, which are given in the figures Fig 4.7 and Fig. 4.8, show the magnetic field lines and flux density distribution solutions.

It is seen that at the given nominal operation the two pole motor is more saturated on the rotor ($B_{\text{sat}} = 3.05\text{T}$) than the 4-pole motor ($B_{\text{sat}} = 2.67\text{T}$), which would cause more rotor eddy current losses. But due to the half operating frequency, the rotor eddy current electrical losses are less than to that of the 4-pole SRIM.

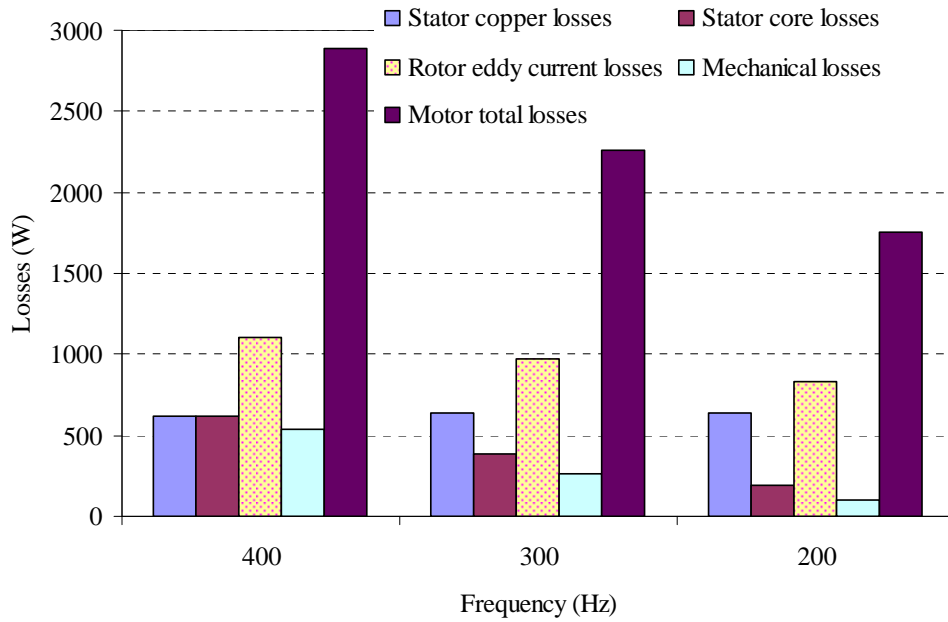


Figure 4.6: Comparison of the calculated losses of the 2-pole SRIM for different operating frequencies, rotor surface with radial grooves, and operation at an electromagnetic torque of $M_e = 12\text{ Nm}$.

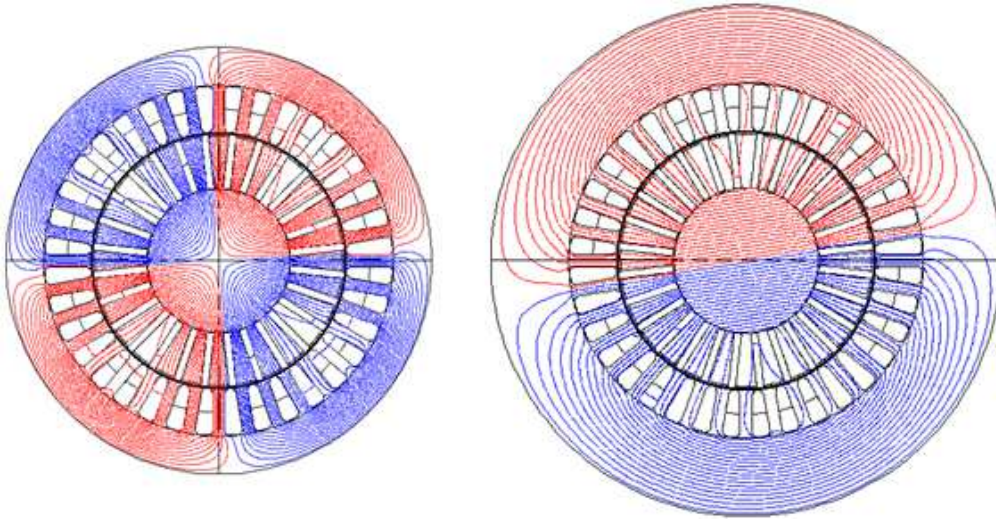


Figure 4.7: Cross-sectional geometry and flux plot at the no-load condition and at a line-to-line voltage $U_s = 330 \text{ V}$, $n_s = 24000 \text{ min}^{-1}$, a) 4-pole SRIM ($f_s = 800 \text{ Hz}$), and b) 2-pole SRIM ($f_s = 400 \text{ Hz}$).

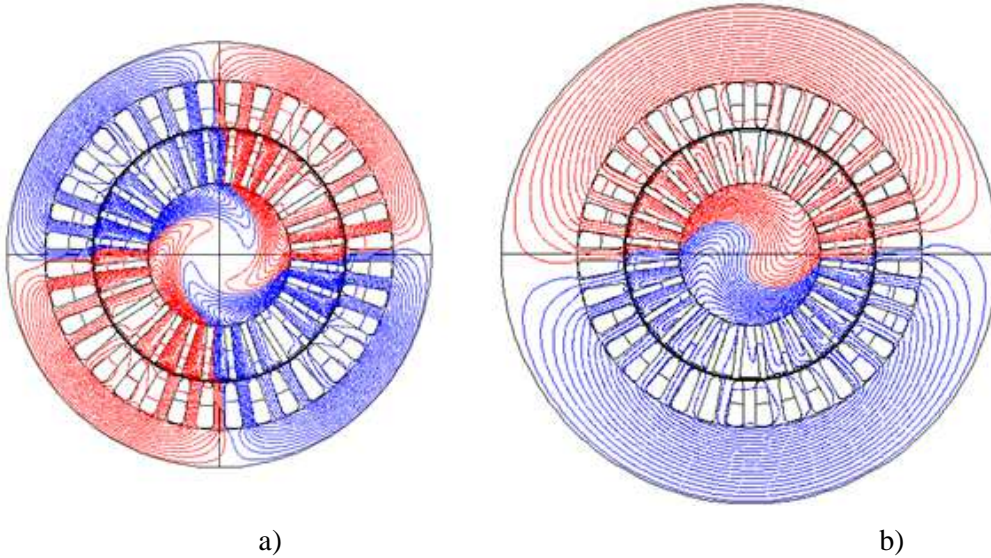


Figure 4.8: Cross-sectional geometry and flux plot for a) the 4-pole SRIM at a line-to-line voltage $U_s = 330 \text{ V}$, $f_s = 800 \text{ Hz}$, $I_s = 88.7 \text{ A}$, $s = 2 \%$, and $M_e = 13 \text{ Nm}$, and b) the 2-pole SRIM at $U_s = 330 \text{ V}$, $f_s = 400 \text{ Hz}$, $I_s = 68.7 \text{ A}$, $s = 2 \%$, and $M_e = 12.6 \text{ Nm}$.

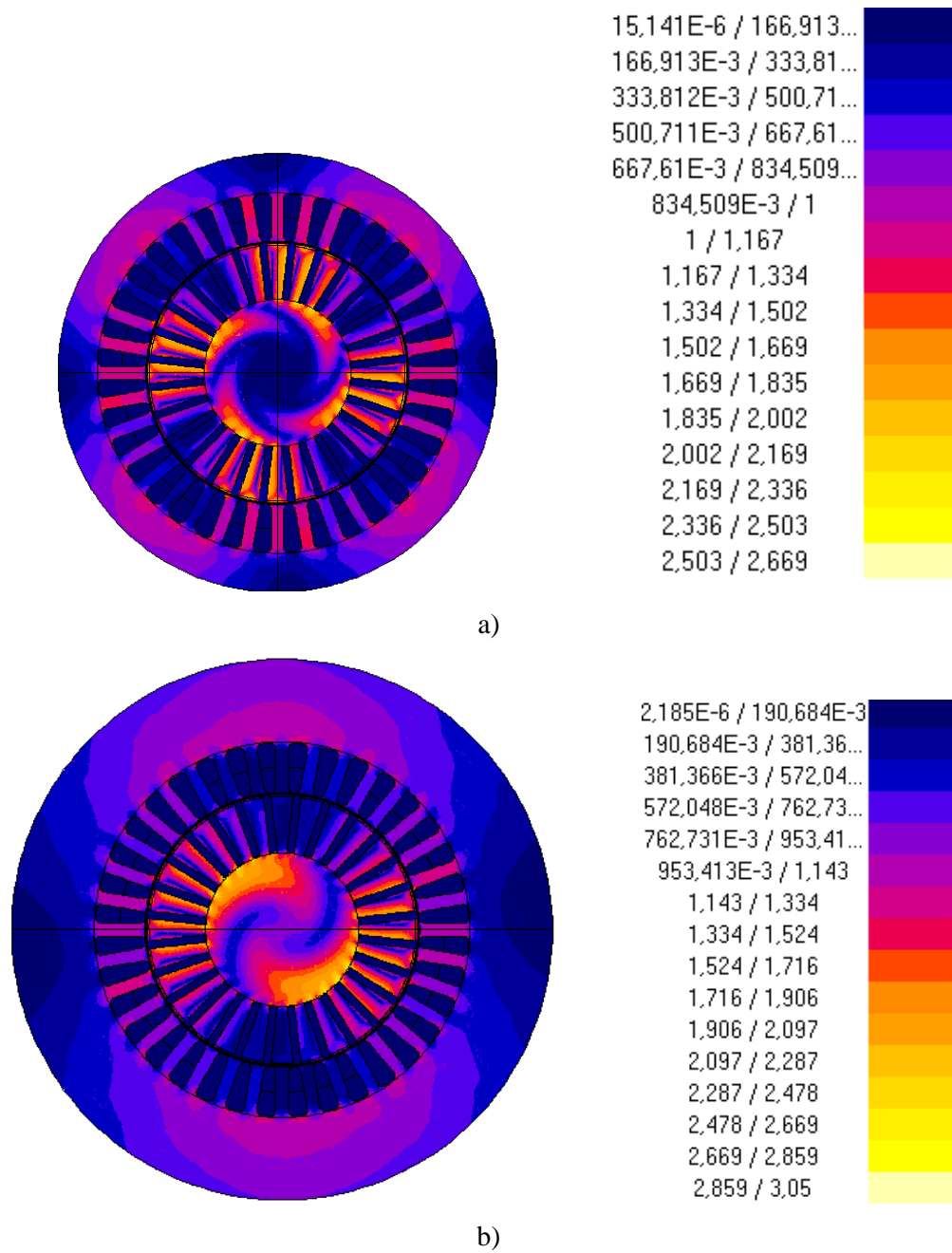


Figure 4.9: Cross-sectional geometry and flux density distribution in Tesla for a) the 4-pole SRIM at line-to-line voltage $U_s = 330$ V, $f_s = 800$ Hz, $I_s = 88.7$ A, $s = 2$ %, and $M_e = 13$ Nm, and b) for the 2-pole SRIM at $U_s = 330$ V, $f_s = 400$ Hz, $I_s = 68.7$ A, $s = 2$ %, and $M_e = 12.6$ Nm.

4.4.2 Losses for different U/f -operations

The calculated losses for the optimized *Rotor B* with radial grooves for operation at different U/f -ratios (Table 4.8) show, that the 2-pole motor has less total losses than the 4-pole motor. This is because of the lower operating frequency and lower magnetizing current in the case of the 2-pole operation of the given high speed SRIM.

Table 4.8 Calculated losses for the Rotor B with radial grooves for operation at different U/f -ratios

$\frac{n_{\text{syn}}}{\text{min}^{-1}}$	$\frac{2p}{-}$	$\frac{f_s}{\text{Hz}}$	$\frac{U_s}{\text{V}}$	$\frac{M_e}{\text{Nm}}$	$\frac{s}{\%}$	$\frac{P_{\text{Cu,s}}}{\text{W}}$	$\frac{P_{\text{Fe,s}}}{\text{W}}$	$\frac{P_{\text{Fe,r}}}{\text{W}}$	$\frac{P_{\text{fr+w}}}{\text{W}}$	$\frac{P_{\text{d,total}}}{\text{W}}$
24000	2	400	330	12	1.9	622	620	1108	538	2888
	4	800	330	12	1.8	666	809	1369	541	3385
18000	2	400	248	12	2.6	637	382	977	265	2261
	4	800	248	12	2.4	654	492	1127	266	2539
12000	2	400	165	12	3.9	638	188	826	104	1756
	4	800	165	12	3.9	656	244	903	104	1907

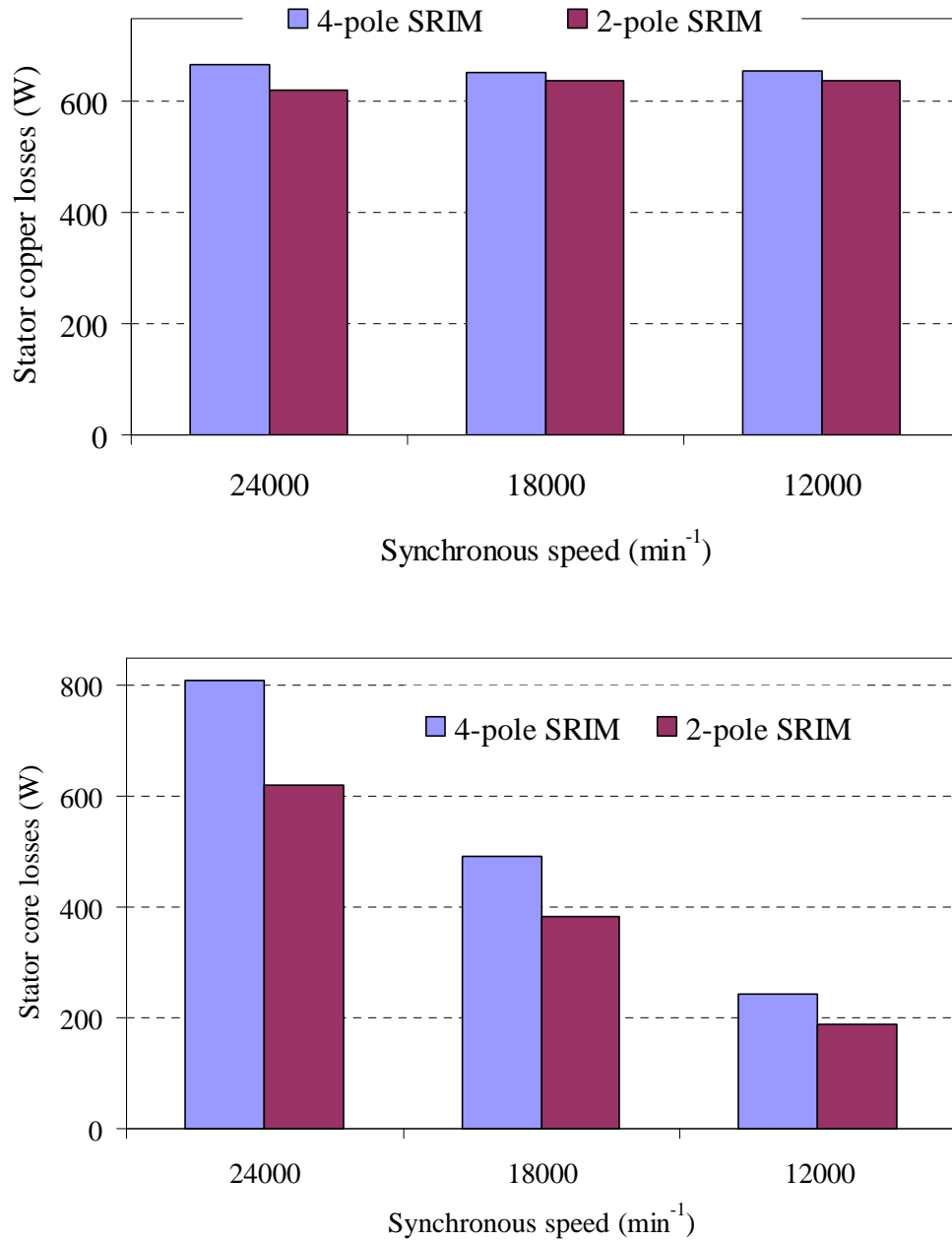
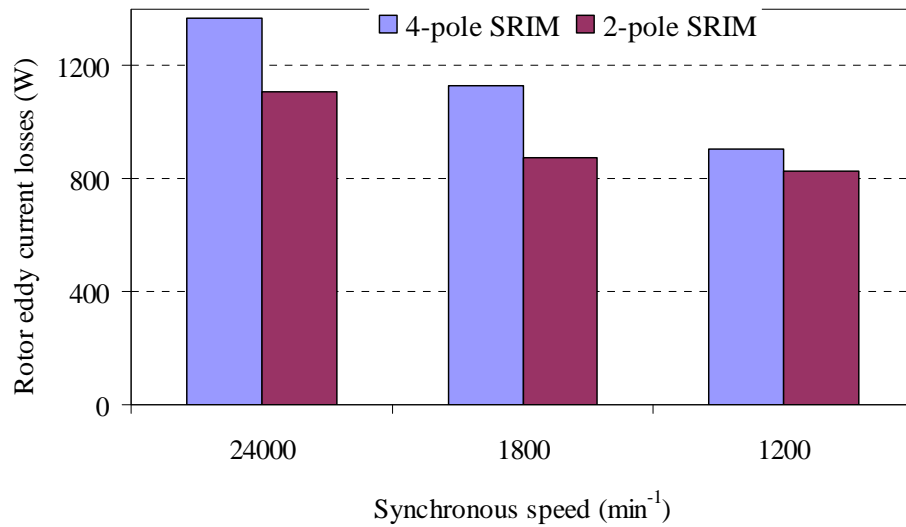
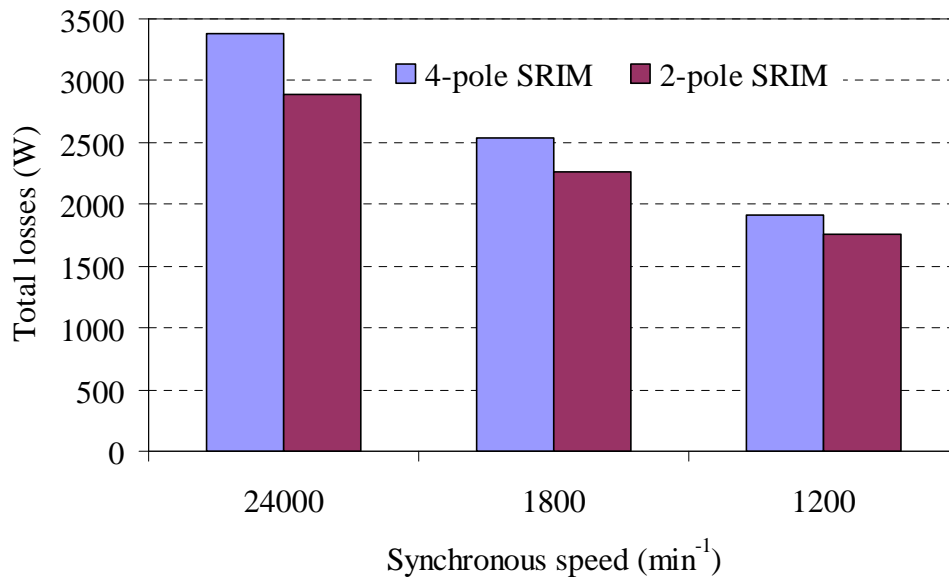


Figure 4.10: Comparison of the calculated losses of the 2-pole and 4-pole SRIM for different operating speeds: a) stator copper losses and b) stator core losses at the rated torque operating condition with the line-to-line voltage $U_s = 330 \text{ V} / 248 \text{ V} / 165 \text{ V}$ and $M_e = 12 \text{ Nm}$.



a)



b)

Figure 4.11: Comparison of the calculated losses of the 2- and 4-pole SRIM for different operating speeds: a) rotor eddy current losses, and b) total motor losses at the rated torque condition with the line-to-line voltage $U_s = 330 \text{ V} / 248 \text{ V} / 165 \text{ V}$ and $M_e = 12 \text{ Nm}$.

4.4.3 Performance Characteristics of the SRIM

The following losses and performance characteristics comparisons for the 2-pole and 4-pole SRIM are given on the illustrations of Fig.4.12, Fig.4.13, and Fig.4.14. The shaft torque M_s is calculated from the air-gap torque M_e (4.4), which is computed using the time stepping FEM, and which determines the mechanical output power P_{out} ,

$$M_s = M_e - \frac{(P_{fr+w} + P_{Ft,r,ad})}{\omega_m}, \quad (4.4)$$

$$P_{out} = M_s \cdot \omega_m, \quad (4.5)$$

where P_{fr+w} are the rotor total mechanical losses, which include the high speed bearing friction losses (P_{fr}) and the air-friction (*windage*) losses (P_w), ω_m is the angular rotor speed and $P_{Ft,r,ad}$ are the rotor additional eddy current losses, caused by the stator field wave slot harmonics (4.6).

$$P_{Ft,r,ad} = P_{Ft,r} - P_{Ft,r1} \quad (4.6)$$

$$P_{Ft,r1} = s \cdot P_\delta \quad (4.7)$$

$$P_\delta = P_{in} - P_{Cu,s} - P_{Fe,s} \quad (4.8)$$

The total rotor eddy current losses $P_{Ft,r}$ in (4.6) are computed in *FLUX 2D* FE simulation as an active dissipated power. In (4.6) $P_{Ft,r1}$ is the rotor fundamental electrical loss given in (4.7), where s is the rotor slip and P_δ is the supplied air-gap power, calculated as in (4.8).

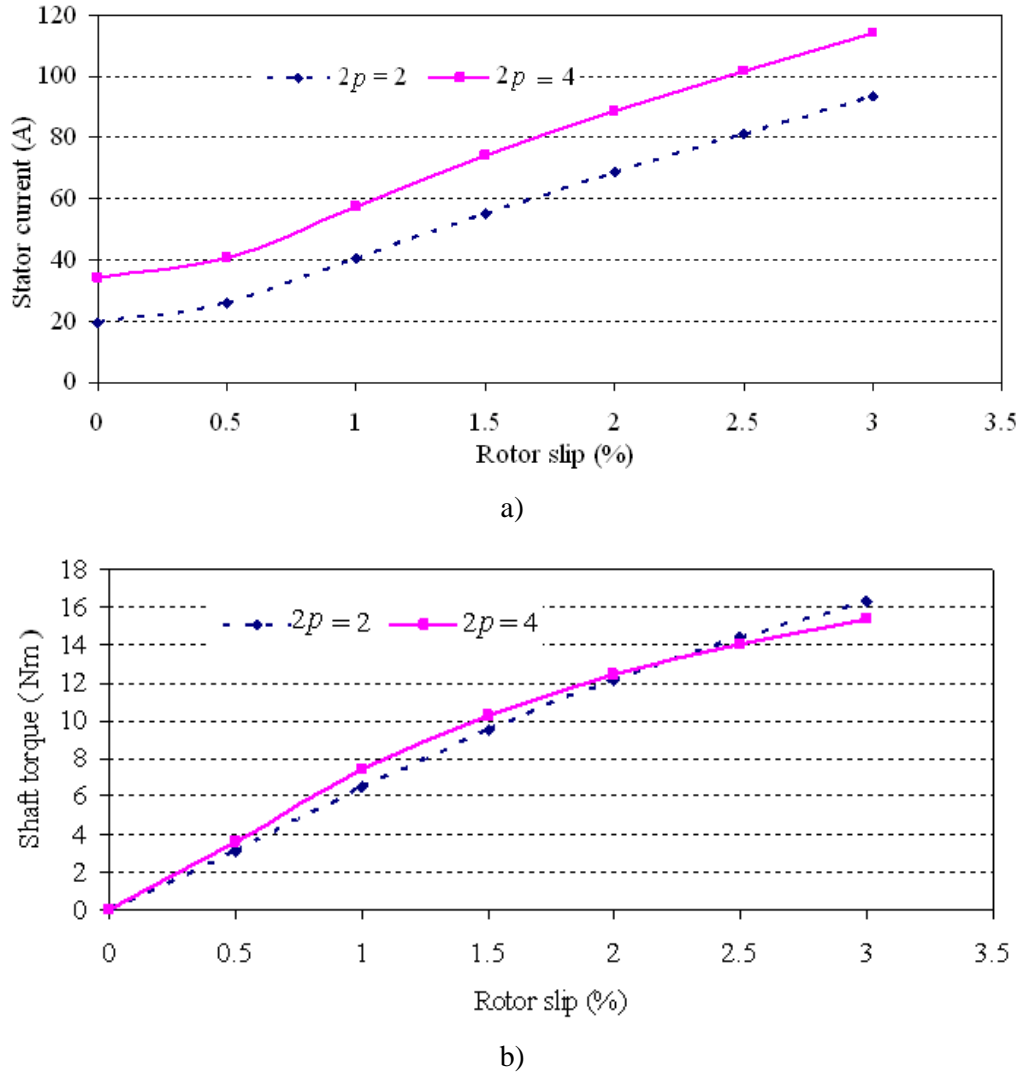


Figure 4.12: Calculated performance characteristics of the 4- and 2-pole solid rotor induction motors at a line-to-line voltage $U_s = 330$ V and $n_{\text{syn}} = 24000 \text{ min}^{-1}$, a) stator currents, and b) output shaft torque from the no-load condition up to $M_s = 16$ Nm loading conditions.

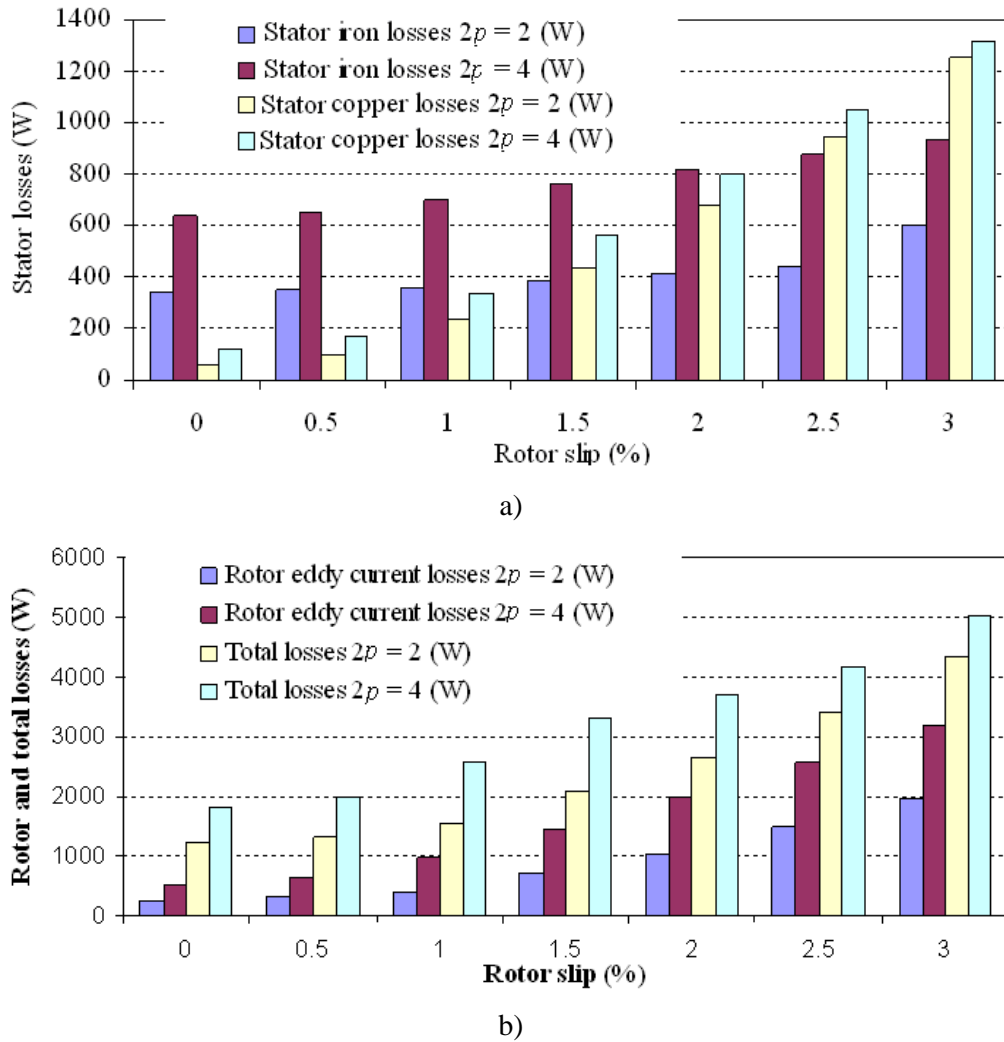


Figure 4.13: Comparison of all calculated motor losses of the 4- and 2-pole SRIM from the no-load to loading conditions at the line-to-line voltage $U_s = 330$ V and $n_{syn} = 24000$ min⁻¹, a) stator losses, and b) rotor eddy current and total motor losses.

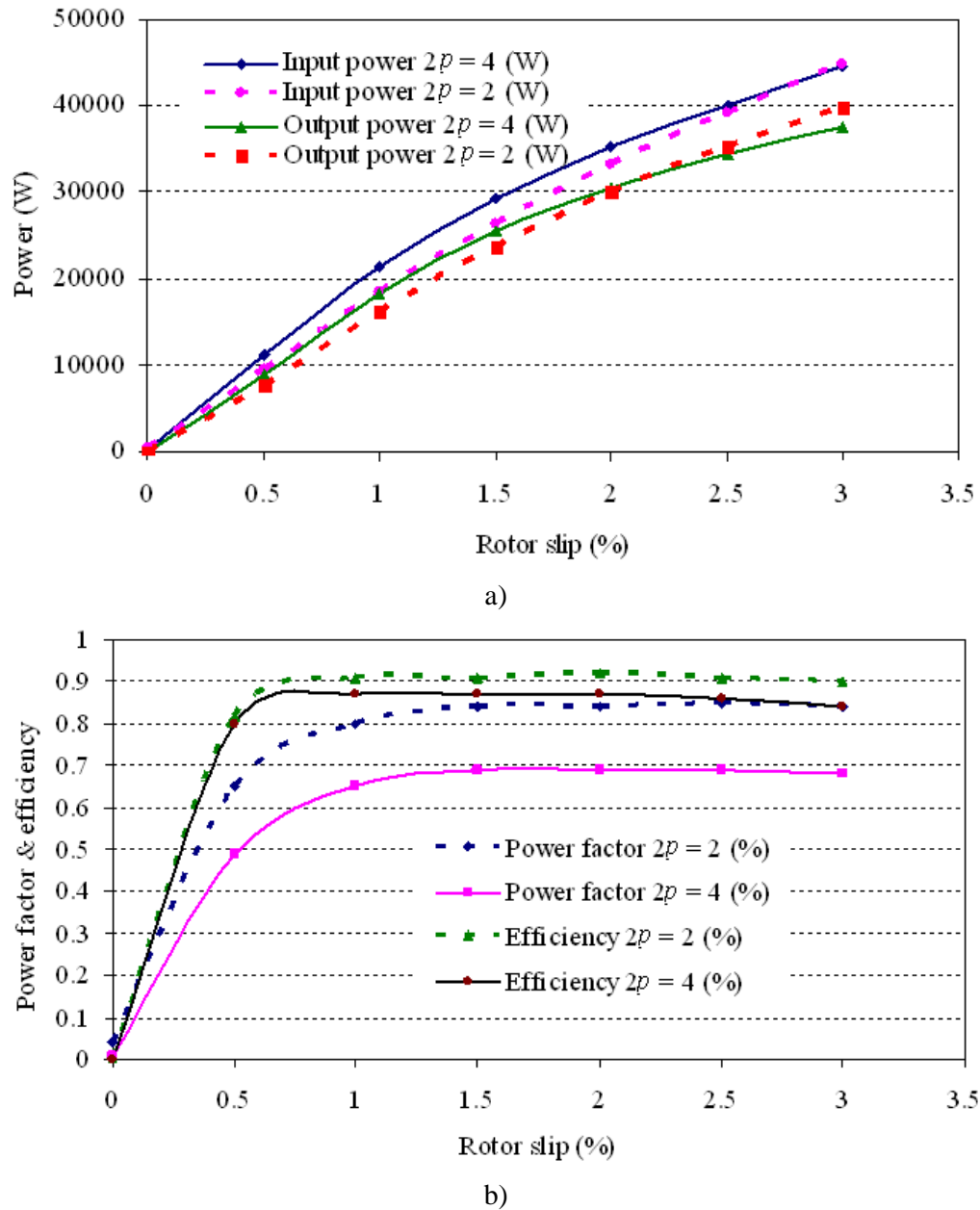


Figure 4.14: Comparisons of operating characteristics of the 4-pole and 2-pole SRIM from the no-load to loading conditions at the line-to-line voltage $U_s = 330$ V and $n_{syn} = 24000$ min⁻¹: a) input and output powers, and b) power factor and efficiency.

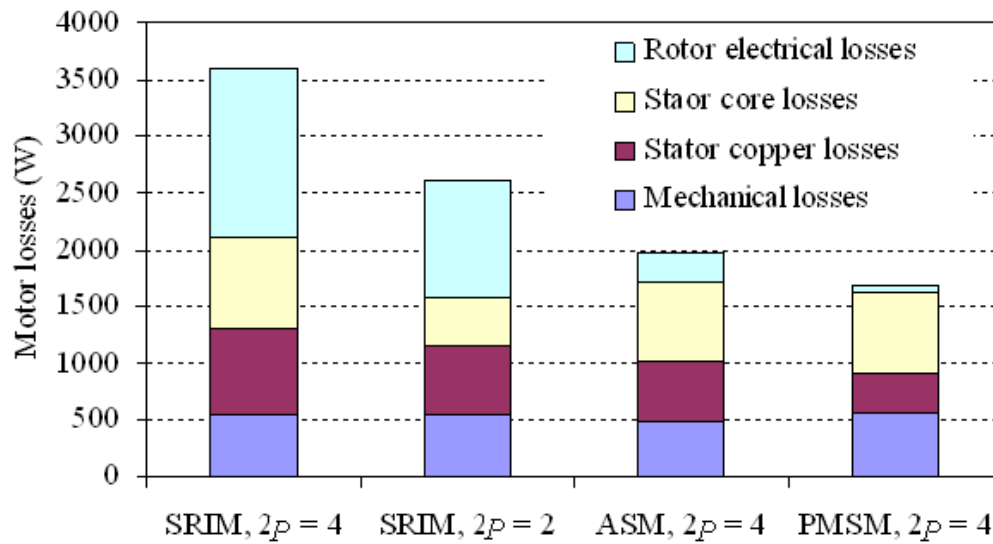


Figure 4.15: Comparison of measured losses for ASM and PMSM with the calculated losses of the SRIM at nominal load with a line-to-line voltage $U_s = 330\text{V}$, $n_{\text{syn}} = 24000/\text{min}$ and a shaft torque $M_s = 12\text{Nm}$.

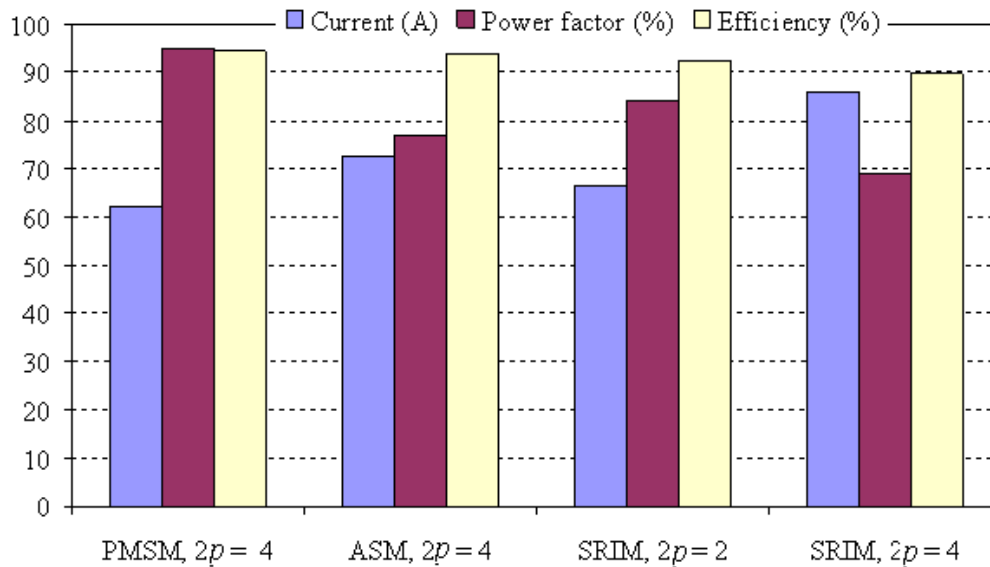


Figure 4.16: Comparison of performance characteristics (current, power factor and efficiency) of the analysed high-speed machines at nominal voltage $U_s = 330\text{V}$, nominal load torque of $M_s = 12\text{Nm}$, and speed $n_{\text{syn}} = 24000/\text{min}$.

4.5 Comparison of Performance Characteristics of High Speed Machines

The quantitative comparison of the examined high speed motor concepts, i.e. the PMSM, the ASM and the SRIM, was done and results are given in Table 4.8, based on the results from [33] for PMSM and ASM and the calculation results of the SRIM. The comparison shows the measured steady-state values of losses and temperatures for the PMSM and ASM with calculated losses and estimated temperatures for the two SRIM. So it is shown in the following chapters, that the stator water-jacket cooling, which was used for the ASM and PMSM, is not sufficient for a steady- state operation of the SRIM at 30kW, 24000 /min. The much higher losses on the rotor side of the SRIM yield too high rotor and bearing temperatures. Hence, an improved rotor cooling is essentially necessary. Hence the comparison given here is not really fair. On the other hand the mechanical limit for the rotor is for the SRIM considerably higher than for the ASM, if another bearing system like ABM (active magnetic bearings) is used. Anyways, the measured PMSM has the best performance characteristic at the nominal operation. It has an efficiency of 94.6 % and operated at a power factor of $\cos\varphi = 0.95$. The least performance result is shown by the 4-pole SRIM with an operating efficiency of only 89.7% and a power factor of $\cos\varphi = 0.69$. The 2-pole SRIM has an efficiency of 92.5 % and an increased power factor of $\cos\varphi = 0.84$, which shows its competitiveness for elevated high speed applications, if the rotor cooling challenge is solved, using e.g. a magnetic bearing system and implementing a direct rotor cooling mechanisms.

Table 4.9: Comparison of a measured 4-pole permanent magnet synchronous motor (PMSM) and a squirrel-cage asynchronous motor (ASM) with the simulated 4-pole and 2-pole solid rotor induction motors (SRIM)

Machine	PMSM $2p = 4$	ASM $2p = 4$	SRIM $2p = 2$	SRIM $2p = 4$
Stator frequency (Hz) / Pole count	800 / 4	800 / 4	400 / 2	800 / 4
Outer / inner diameter (mm)	150 / 90	150 / 90	177 / 90	150 / 90
Mechanical air gap / slot opening (mm)	0.7 / 2.3	0.7 / 2.3	0.6 / 2.3	0.6 / 2.3
Stack length (mm)	90	90	90	90
Number of stator slots	36	36	36	36
Stator copper / iron losses (W)	357 / 708	537 / 700	625 / 404	757 / 813
Rotor electrical / friction losses (W)	95 / 555	250 / 480	1070 / 537	1537 / 539
Stator winding / Rotor temperature (°C)	100 93	124 130	100* 200*	100* 200*
Shaft torque (Nm)	12	12	12	12
Rotational speed (1/min)	24000	23821	23520	23544
Rotor slip (%)	0	0.75	2.0	1.9
Input / Output power (kW)	31.9 / 30.2	31.9 / 29.9	32.2 / 29.6	33.0 / 29.6
Direct motor efficiency (%)	94.6	93.8	91.9	89.8

*) Estimated values, which are used for the calculation

5 Construction of Prototype Solid Rotor Motors

According to the design and optimization, the two 4- and 2-pole high speed solid rotor motors with one common rotor were constructed at the laboratory of the *Institute for Electrical Energy Conversion, Darmstadt University of Technology*, as shown in the constructional detail diagram of Fig.5.1.

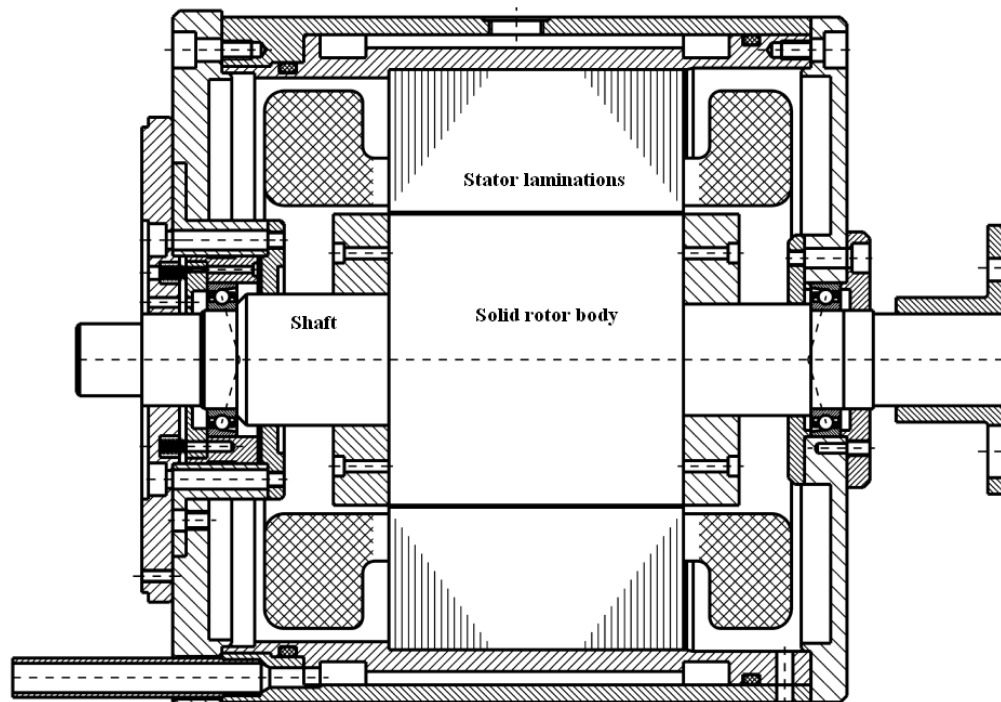


Figure 5.1: Construction detail of SRIM with copper end-rings ($2p = 2$).

5.1 Stator Construction

Both the 4- and 2-pole stators are constructed with a 36 slots stator core and a steel stator frame with water-jacket cooling system (detailed drawings see Appendix A). The current and power densities of the designed high-speed machines are high, so that the stator indirect water cooling of the winding was indispensable.

5.1.1 Stator Frame

The stator frame is made from massive steel with a water jacket cooling system, which is constructed with 24 longitudinal cooling ducts. Each duct has a width of 12 mm and a height of 7 mm with a distance of 5.3 mm between adjacent turns. Each six and six ducts are parallel to get the flow rate of 3.3 l/min as shown on the Fig. 5.2. At a flow rate of 3.3 l/min, the coolant (cold water) circulates with enough water velocity in the cooling ducts.

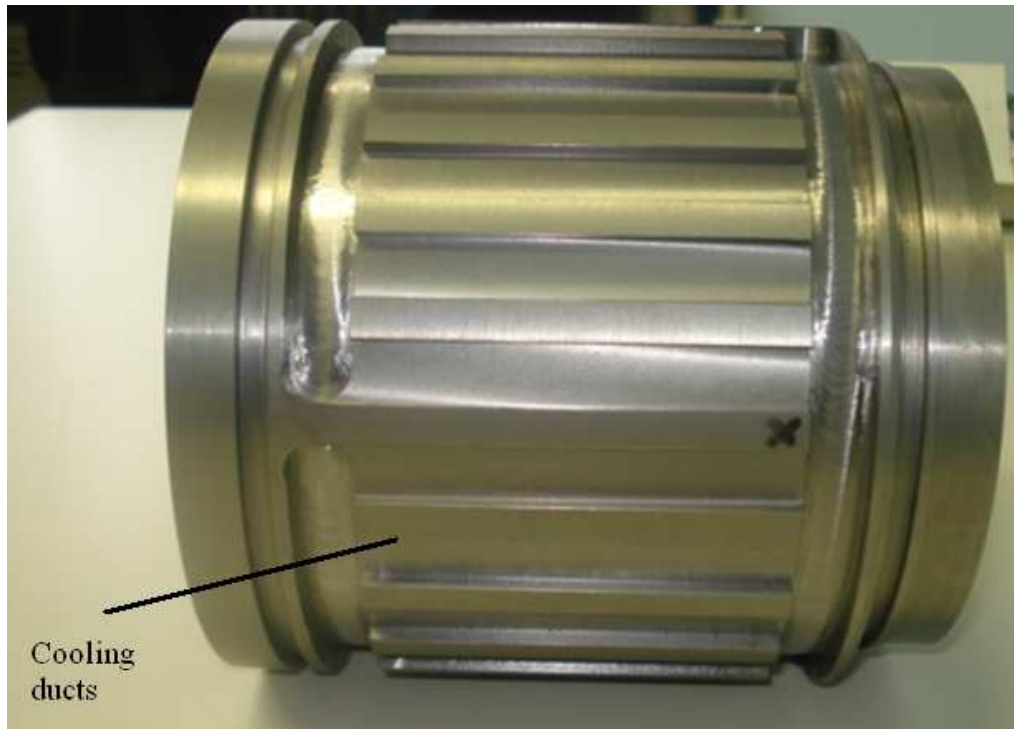


Figure 5.2: Stator frame with water jacket cooling ducts.

5.1.2 Stator Core

In high-speed machines the eddy current losses are dominant; therefore high quality thin stator iron laminations are required. Hence, the 4- and 2-pole high speed solid rotor induction motors are constructed with special low loss steel stator core

laminations *M330-35A* ($2p = 4$) and *M270-35A* ($2p = 2$) respectively. The laminations have 0.35 mm sheet thickness. The specific core losses are given in Table 5.1. The core losses depend on the operating frequency and on the applied voltage. The calculated magnetic flux density level is as given in Fig. 5.3.

Table: 5.1 Specific core losses of the stator core laminations [16]

Material	Frequency / Hz	Specific losses at 1T / W	Specific losses at 1.5T / W
<i>M330-35A</i>	50	1.22	2.94
	400	23.5	57.8
	1000	106	279
<i>M270-35A</i>	50	1.01	2.47
	400	17.3	41.8
	1000	73.0	192

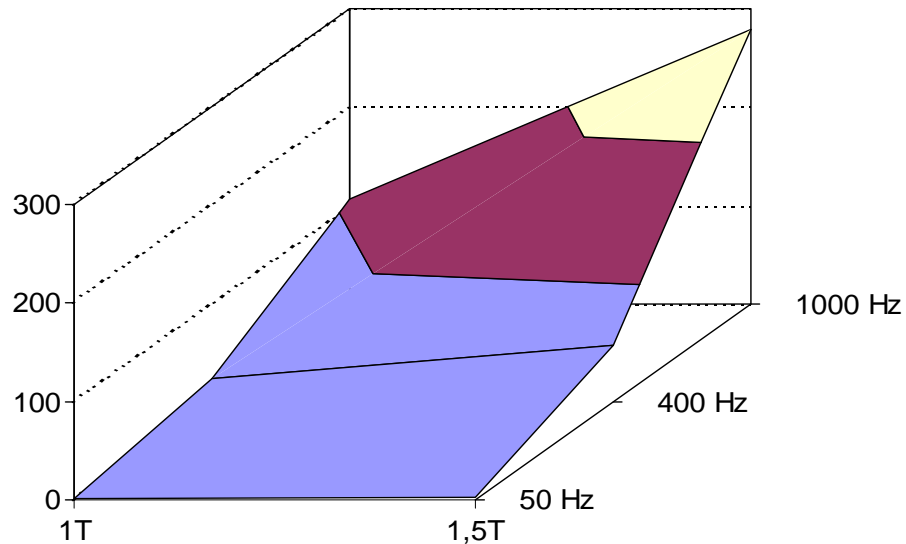


Figure 5.3: Specific core losses of the stator lamination material *M330-35A* in W/kg as a function of the frequency and of the flux density [16].

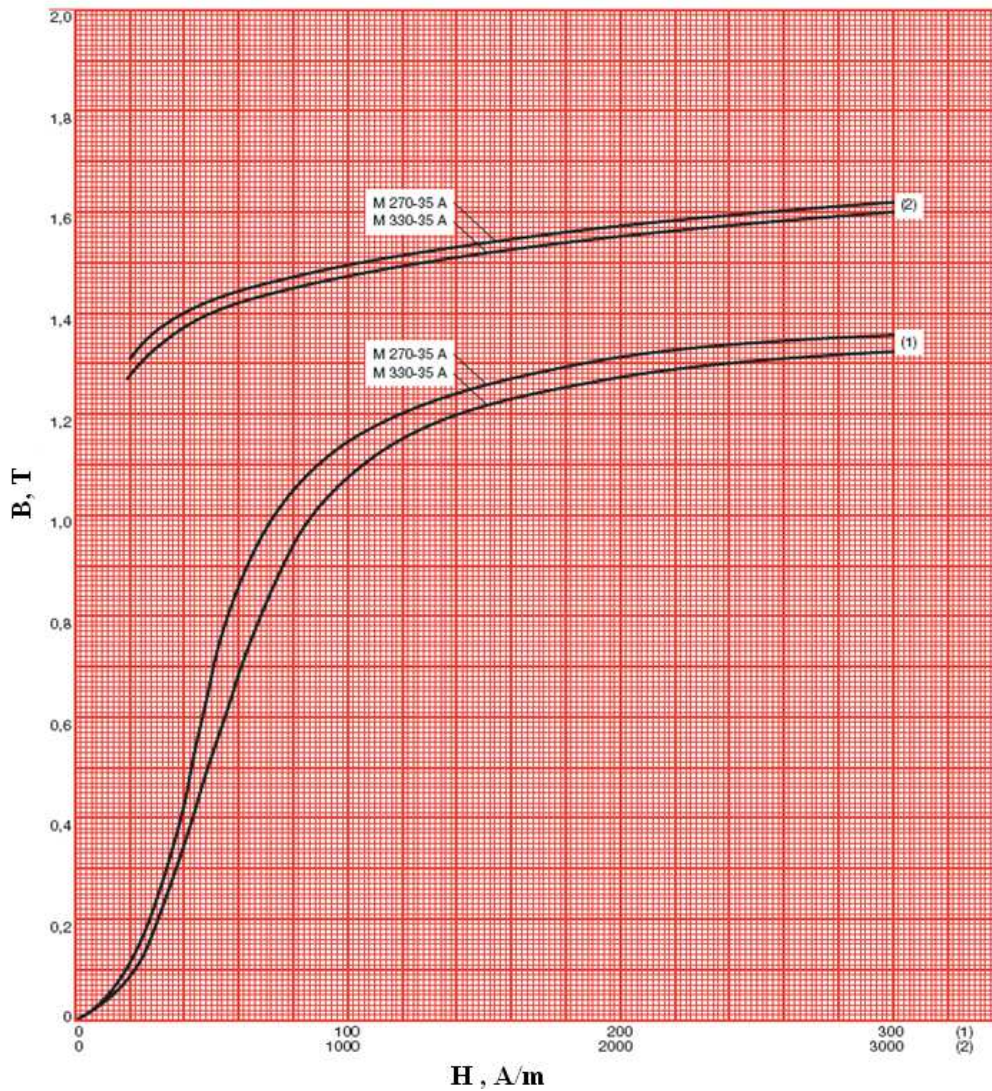


Figure 5.4: DC magnetization characteristics of the implemented stator core laminations [Source: *STANZWERK*].

5.2 Stator Windings Design and Construction

According to the design parameters, the three phase double layer integer slot stator windings with the winding data, given in Table 5.2, and developed winding diagrams (Fig. 5.5 and Fig. 5.6), were constructed for both the 4-pole and 2-pole SRIM.

Table: 5.2 Winding data of the analysed solid rotor induction motors

Machine	$2p = 4$	$2p = 2$
Chording W/τ_p	7/9	14/18 = 7/9
Slot count Q_s	36	36
Turns per coil and per phase N_c, N_s	8, 24	4, 24
Parallel wires and branches a_i / a_a	3 / 4	3 / 2
Overhang length l_b (mm)	115	230
Slots per pole and phase q	3	6
Round wire diameter d_{Cu} (mm)	0.9	1.25
Stator winding resistance R_s (Ω), 20 °C	0.024	0.036

The stator winding losses $P_{Cu,s}$ in the 3-phase winding comprise the I^2R losses plus the 1st order current displacement losses $P_{Cu,Ft,b}$ due to unbalanced current sharing between the a_i parallel wires per turn plus the 2nd order current displacement losses $P_{Cu,Ft,a}$ due to the skin effect within each wire. The maximum number of parallel branches $a_a = 2p$ allows the minimum number of turns per coil N_c according to (4.1). So the current per parallel branch $I_c = I_s / a_a$ is minimum; in the same way the number of parallel wires a_i per turn for a given wire diameter d_{Cu} is minimum, which allows a minimization of the 1st order eddy current losses due to unequal current sharing. By minimizing the diameter d_{Cu} , the 2nd order eddy current losses are reduced, so for a given turn cross-section area $A_{Cu} = a_i \cdot d_{Cu}^2 / 4$ an optimum combination between a_i and d_{Cu} was found, which results in low total stator winding additional copper losses.

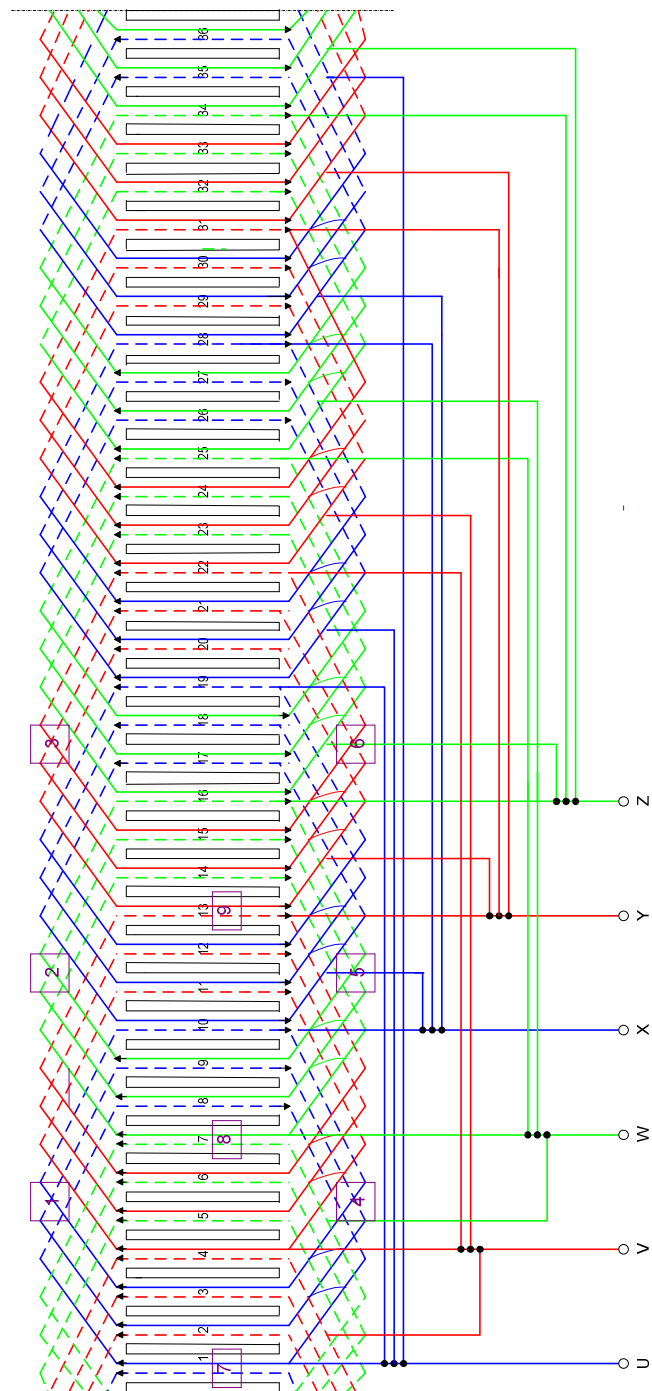


Figure 5.5: Distributed stator winding diagram of the constructed prototype high speed solid rotor induction motor (Table 5.2) for $2p = 4$. The numbers in rectangular frames denote the locations of the thermocouples.

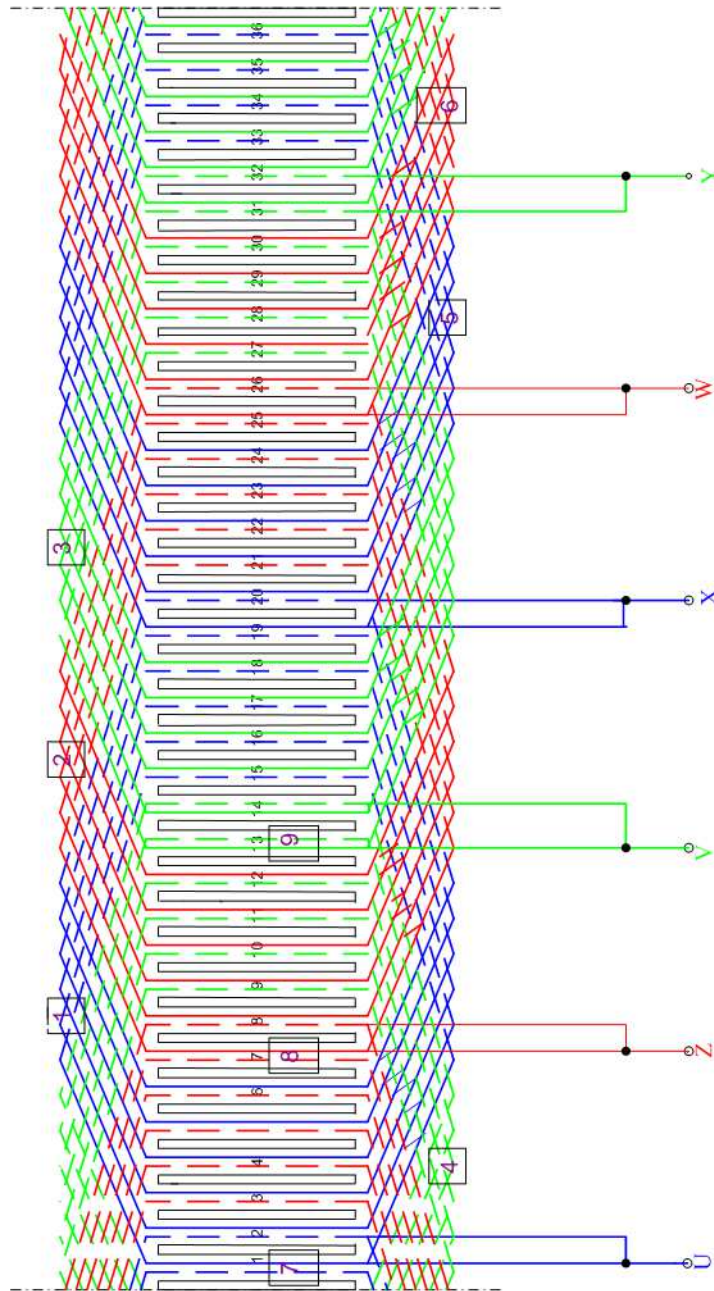


Figure 5.6: Distributed stator winding diagram of the constructed prototype high speed solid rotor induction motor (Table 5.2) for $2p = 2$. The numbers in rectangular frames denote the locations of the thermo-couples.

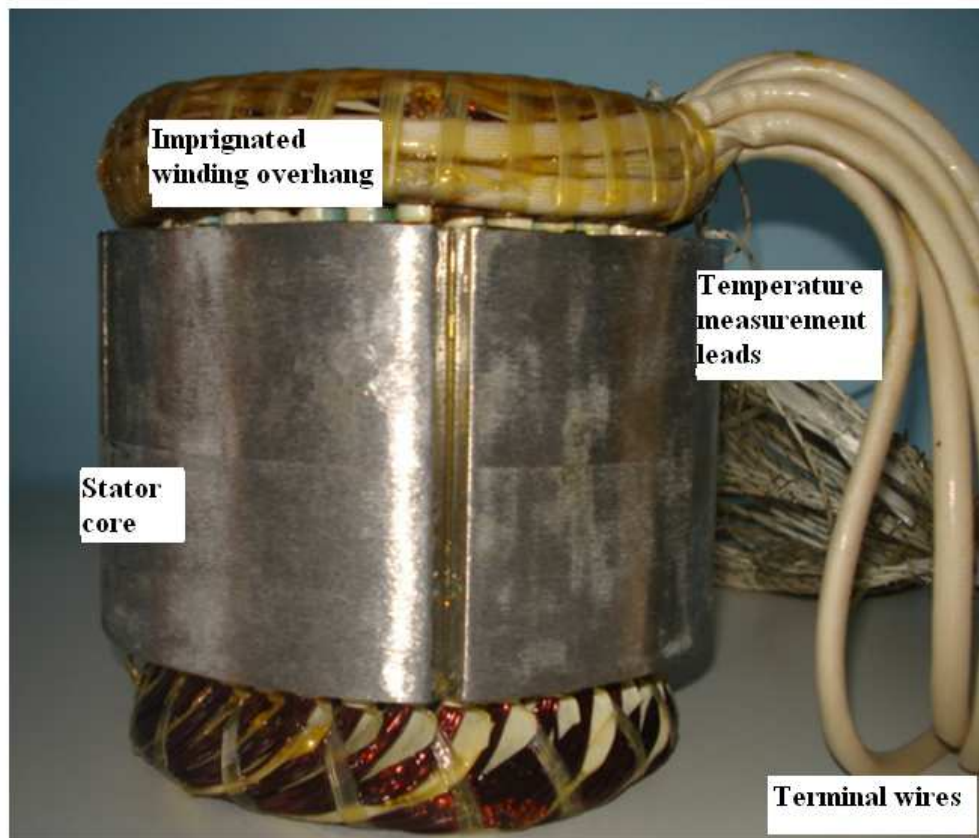


Figure 5.7: Stator winding inside stator core.

The stator winding temperature rise was measured using, 9 temperature sensors (thermocouples), made from Fe-Cu-Ni, mounted at different positions in the windings. The first 6 sensors are mounted at the winding overhangs with each 3 for drive and non-drive ends, and the remaining 3 are mounted in the slot middle, as shown on the winding diagrams Fig. 5.5 and Fig. 5.6. Generally, the water jacket cools effectively the winding parts, which are placed in the slots, but not the winding overhangs. Hence the winding overhangs are the hot spots. In order to strengthen them against the mechanical and thermal stresses, these parts were sealed, using an epoxy resin encapsulation at *Siemens AG Bad Neustadt / Saale*.

5.3 Solid Rotor Technology

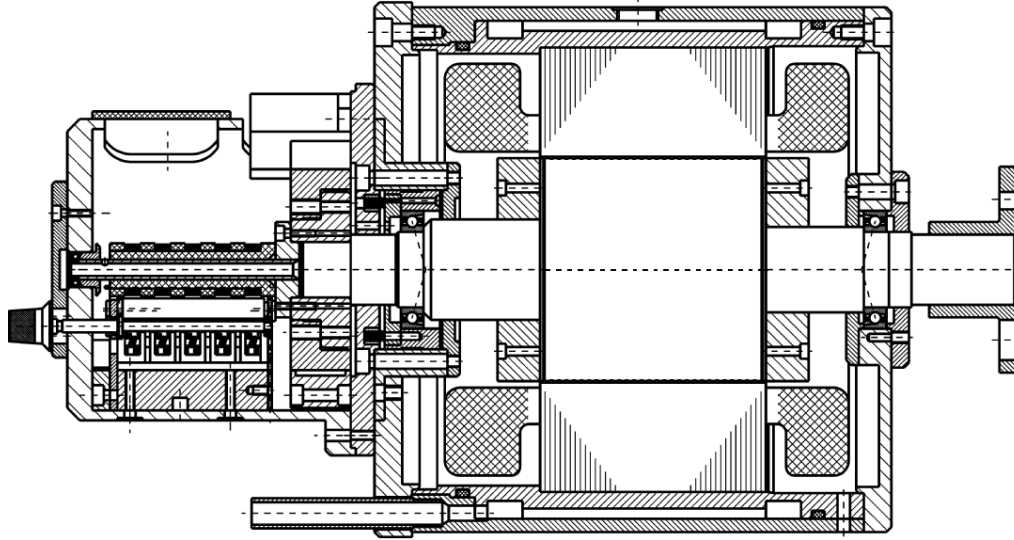
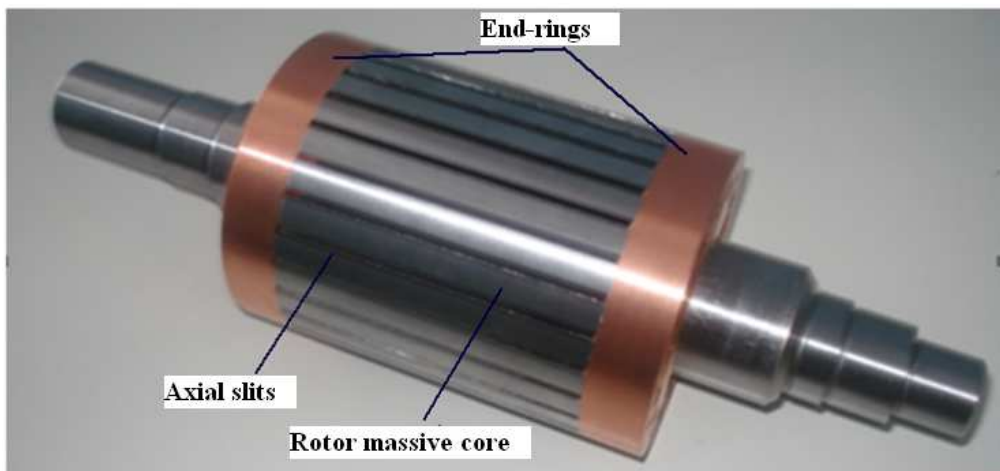


Figure 5.8: Solid rotor motor construction with rotor temperature measurement mechanism via slip-rings (left).

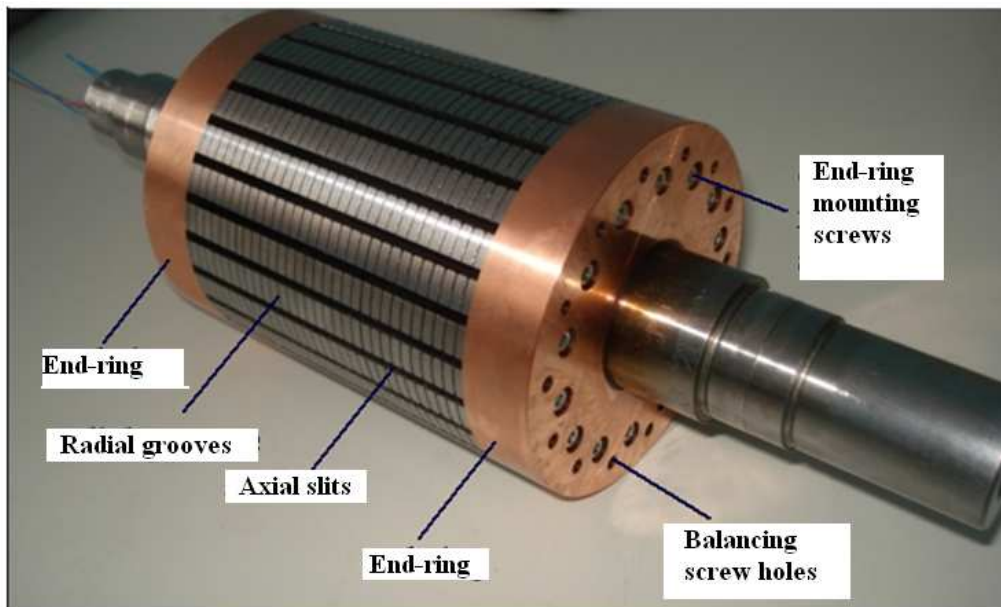
The first prototype axially slitted rotor with copper end-rings was constructed for the application for both 4- and 2-pole solid rotor induction motors (Fig. 5.9a). The rotor end-rings were screwed to the solid rotor side faces in order to ensure a high mechanical strength at high speed operation against the rotor centrifugal forces as shown in the Fig. 5.9b. To decrease the rotor eddy current losses, the first rotor was modified to the next rotor version (Fig.5.9b) with radial grooves, higher air-gap distance and deeper slit (Tab.5.3).

Table: 5.3 Rotor geometry parameters (see Appendix B)

Rotor parameters	Rotor A	Rotor B
Rotor outer diameter (mm)	89.2	88.8
Radial air gap distance (mm)	0.4	0.6
Slit width / slit depth (mm)	2.5 /13	2.5 /19
Radial grooves width /depth (mm)	-	0.5 & 0.7
Rotor & Copper end-ring length (mm)	90 & 15	90 & 15



a)



b)

Figure 5.9: Constructional cross-sectional view of the two solid rotor designs: a) *Rotor A*, b) *Rotor B*.

5.3.1 Rotor Core Material

In solid rotor high-speed machines the developed rotor torque strongly depends on the rotor material properties. In [1], [17], [18], [25] it is shown, that a slitted rotor produces a higher torque, when the rotor core material has a high saturation flux density and a low resistivity. Accordingly, the constructed prototype motor rotors are made from the material VACOFER S1, which is nearly pure iron [57]. VACOFER S1 is the material name of iron manufactured by means of sintering (powder metallurgy). It is a process of blending the metal powders followed by hot static compaction to produce the desired shape and size. The given compact material is then sintered by heating at elevated temperature, preferably below the melting point to get a product of desired density, structure and properties. The two stages of compaction and sintering are combined in to a single hot pressing. The high purity of the material (99.98 % pure iron) leads to a very low coercive force. It is used in applications that require achieving high induction values with low field strength as well as ones that require low residual induction in magnetic circuits with an air gap after the field is switched off (soft magnetic characteristic) [57]. VACOFER S1 offers distinct advantages for numerous applications, because of its purity and lack of pores. It has a high conductivity and saturation limit, but is characterised by a low tensile strength as shown on its physical properties in Table 5.4. So the mechanical strength of the rotor is checked at 20 % over-speed ($1.2 \cdot 24000 = 28800$ /min), using a 2D FEM simulation with ANSYS (Fig. 5.10 and Fig.5.11) [6]. The maximum calculated *von Mises* equivalent stresses for *Rotor A* and *Rotor B* are 87 MPa and 125 MPa respectively. It acts at the roots of the slits, but it is within the yield strength limit of the material 200 MPa with a margin of 1.6 for the maximum stress case of *Rotor B* with deeper slits.

Table: 5.4 Electromagnetic and mechanical parameters of *VACOFER S1* [41], [57]

Mass density (kg/m ³)	Resistivity at 20 °C (μΩcm)	Saturation flux density (T)	Young modulus (GPa)	Yield strength (MPa)	Tensile strength (MPa)
7860	9.8	2.15	200	200	320

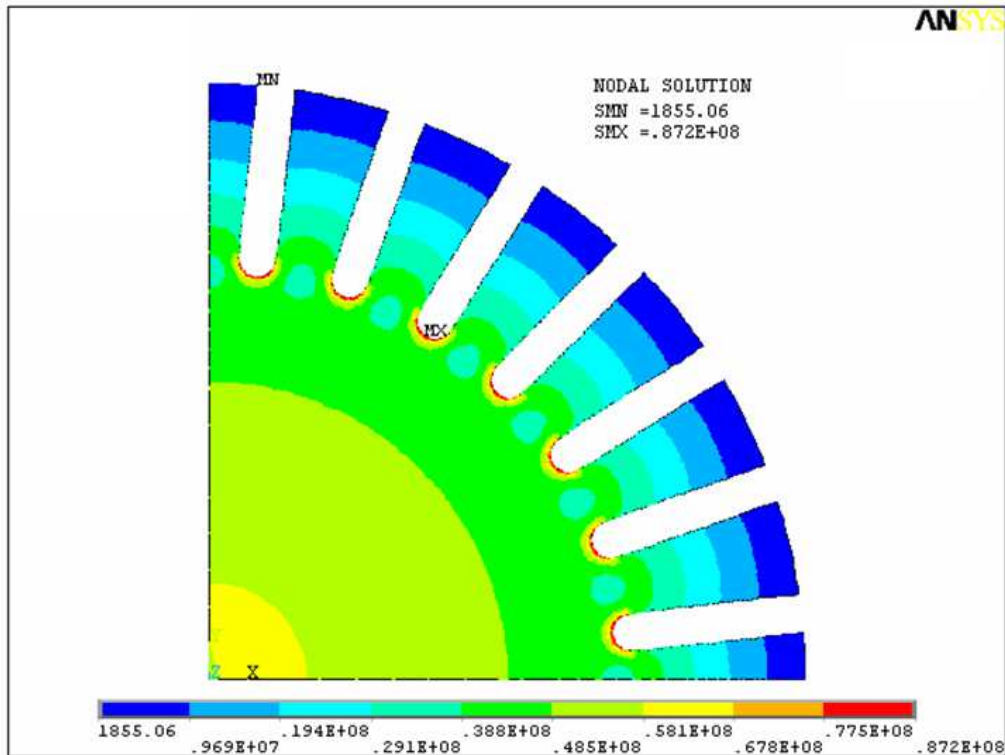


Figure 5.10: Calculated 2D stress distribution in the solid *Rotor A* at 20% overspeed 28800/min (MX: Maximum Value: 87 MPa).

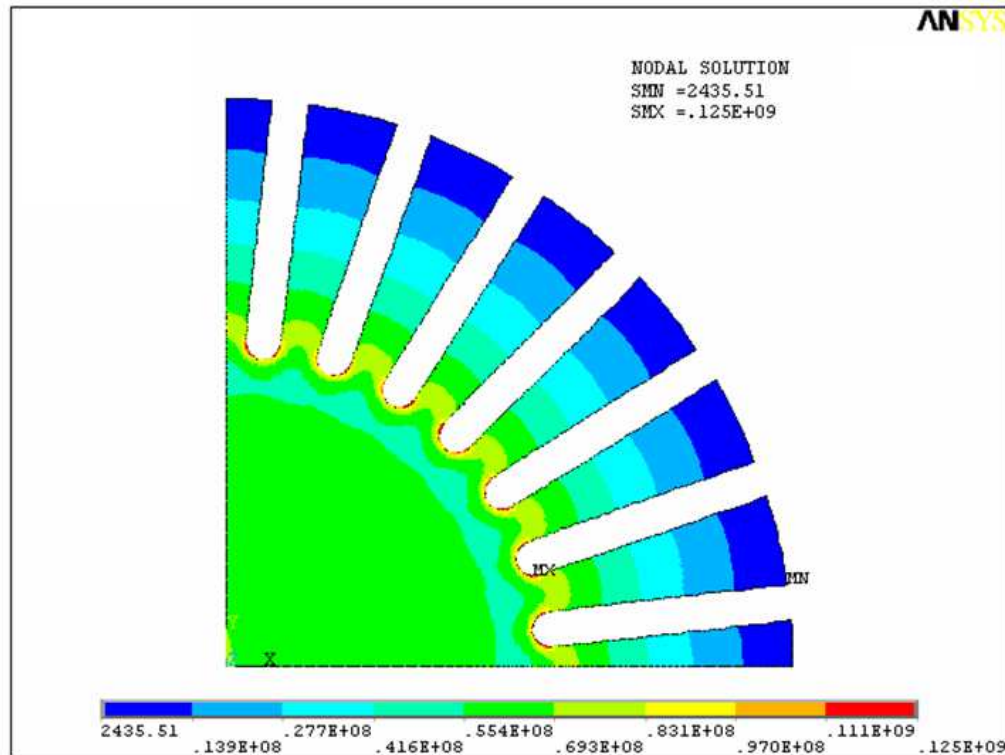


Figure 5.11: Calculated 2D stress distribution in the solid *Rotor B* at 20% overspeed 28800/min (MX: Maximum Value: 125 MPa)

5.3.2 Rotor End-Rings

The rotor end-ring geometry parameters were calculated in the design and optimisation stage in Chapter 2. The end-rings are made from specially treated copper. Copper in its pure form is a well-known material that is widely used in industrial applications, mainly because of its high electrical and thermal conductivities. It has also an excellent corrosion resistance and is easy to fabricate. However, the major drawback of pure copper is its low tensile and yield strengths at room temperature and as well as at high temperatures, like 220 MPa and 70 MPa at room temperature of 20 °C respectively. Generally copper can be strengthened mainly by alloying it with other elements, but alloying causes a significant loss in conductivity. But it can also be strengthened by incorporating fine particles of a second compound in its matrix, causing only a small loss in conductivity. The

second compound can be a stable oxide, added to the copper matrix. Copper systems strengthened with stable oxide particles, which are referred to as *Dispersion Strengthened Copper*; do not experience oxide particle growth or dissolution of the oxide particles into the copper matrix. Therefore their strength is not significantly affected by exposure to high temperature. The effectiveness of these oxide particles as strengtheners depends upon particle size (finer is better), particle distribution (well dispersed is better), particle density (more per unit volume is better), and particle spacing (closer is better). One such material made by the internal oxidation techniques, which fulfils the above advantages, is *GLIDCOP AL-15*. Hence, the rotor end-rings of the machine are made from *GLIDCOP AL-15* (0.3 % of Aluminium oxide content), which is a low aluminium oxide content grade of dispersion strengthened copper. It consists of a pure copper matrix, containing finely dispersed sub-microscopic particles of Al_2O_3 , which act as a barrier to the dislocation movement. The dispersed Al_2O_3 is thermally stable; it retards the recrystallization of the copper. So, no significant softening occurs at a high temperature exposure in the solid rotor due to the high rotor losses P_r . Along with superior strength retention, the thermal and electrical conductivities are higher than the conventional copper alloys, as it is given for the physical properties in Table 5.5. [22], [53]. The stress acting on the end ring is calculated with ANSYS (Fig. 5.12) and also analytically, when the end ring is considered as a thick rotating shell. The tangential stress due to rotation depends on the radius [10]. For the inner radius $r_i = 18\text{mm}$, where the tangential stress is maximum, it is given by the expression (5.2) and is found to be equal to 136 MPa.

$$\sigma_{t,\omega} = 0.4125 \cdot \rho_{\text{ring}} \cdot \omega_m^2 \cdot (0.424 \cdot r_i^2 + 2 \cdot r_a^2) \quad (5.1)$$

In (5.1) ρ_{ring} is the mass density, ω_m is the 20 % angular over-speed, $r_a = 44.4\text{ mm}$ is the outer and $r_i = 18\text{mm}$ are the inner ring radii.

Table 5.5: Electrical and mechanical properties of *GLIDCOP AL-15* [22]

Mass density (kg/m^3)	Resistivity at 20 °C ($\mu\Omega\text{cm}$)	Young modulus (GPa)	Yield strength (MPa)	Tensile strength (MPa)
8900	1.86	130	255	365

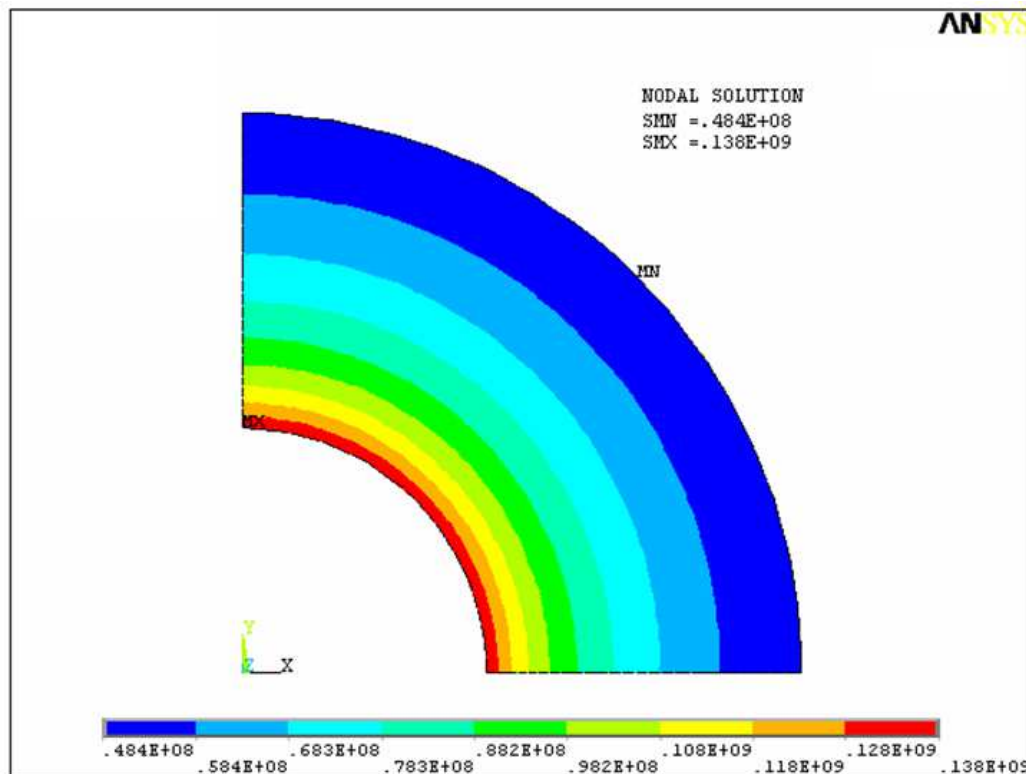


Figure 5.12: Calculated stress distribution of the copper end-rings shell at 20 % over speed $n = 28800/\text{min}$ (MX: Maximum *von Mises* stress: 138 MPa, MN: Minimum *Von Mises* stress: 48.4 MPa).

5.3.3 Rotor Balancing and Over-Speed Test

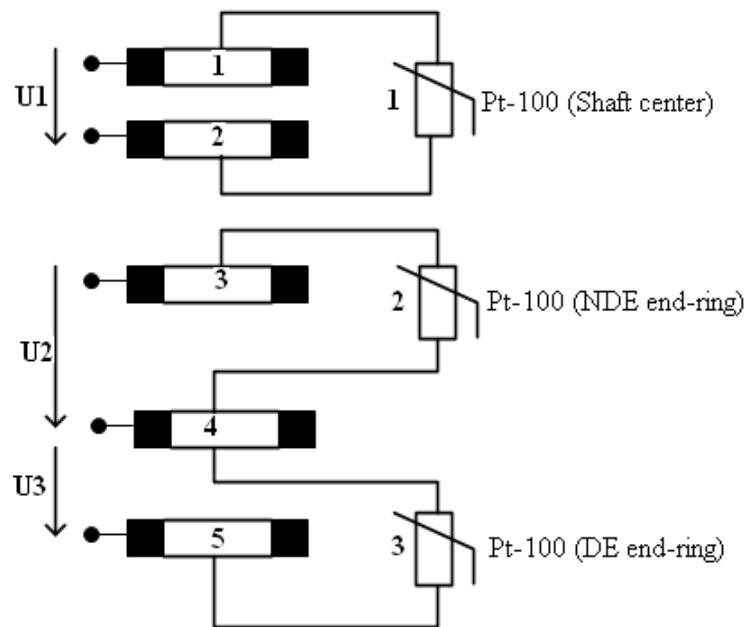
An unbalanced rotating rotor will cause vibrations and stresses of the rotor itself and its supporting structure. Balancing of the rotor is therefore necessary to minimize vibrations, audible noise, structural stress and power losses and on the other hand will help to increase the bearing life. Centrifugal forces act upon the entire mass of a rotating component. If the mass of the rotor is evenly distributed around its shaft axis, the rotor is balanced and rotates without vibration. However, if an excess of mass exists on one side of a rotor, the centrifugal force acting upon the heavy side exceeds the centrifugal force exerted by the light side and pulls the entire rotor in the direction of the heavy side. The centrifugal force increases proportionally to the square of the rotational speed. Hence especially for high speed applications the balance test must be performed accurately. The imbalance is measured in (g·mm), which is the total rotor mass, concentrated in its center of gravity, multiplied by its distance from the shaft rotational axis. The residual imbalance after the balancing process must stay below certain standard limits, depending on the application of the rotor. This residual imbalance is defined as the circumference speed G of centre of gravity and is given by:

$$G = \Omega_m \cdot e_s, \quad (5.2)$$

where G is the standard grade (mm/s), Ω_m is the angular speed of the rotor (s^{-1}) and e_s is the distance of the center of gravity from the rotational axis. Accordingly the balancing test of the *Rotor A* was done according to *DIN ISO 1940* [12], [27], [29], Grade 2.5, which allows the residual imbalance of 2.5 mm/s, at the company *SCHENK RoTec GmbH*. An over-speed spinning test was also successfully performed up to 34000/min for about 2 minutes without visible damage or deformation of the rotor. In addition, after the geometry optimization and machining of the *Rotor A*, the resulting *Rotor B* with radial grooves and higher air-gap distance was also balanced, using the balancing screw masses (Fig. 5.9) at the electrical machine factory *Brenner GmbH, Bürstadt*.

5.4 Rotor Temperature Measurement Set-up

The rotor temperature measurement is accomplished via Pt-100 resistor sensors, which are fixed at different rotor parts as it is depicted on the Fig.5.14. One was mounted at the centre of the shaft and the other two were fixed at the inner parts of the drive-end and non drive-end end-rings. The three sensors were connected to five sliver made slip-rings, which are mounted on the shaft as shown on the Fig. 5.15a. The slip-rings are constructed with a reduced diameter of 21mm to be mechanically stable at high speed operation up to 30000 min^{-1} . The Pt-100 sensor voltage is supplied to a digital display as shown on the Fig. 5.13. It is obvious, that the wear of the carbon brush is high, due to the high speed operation. Accordingly, a pressing mechanism was constructed at the *Institute of Electrical Energy Conversion, Darmstadt University of Technology*, on the system to make a good and stable brush contact with the ring, which keeps the contact resistance low and increases the accuracy of the measurement result [24].



- $U1$, $U2$ and $U3$ are the sensed voltages via the slip-rings.
- 1, 2, 3, 4 and 5 are the five slip-rings.

Figure 5.13: Schematic diagram of rotor temperature sensors (Pt-100) connected to the slip-rings.

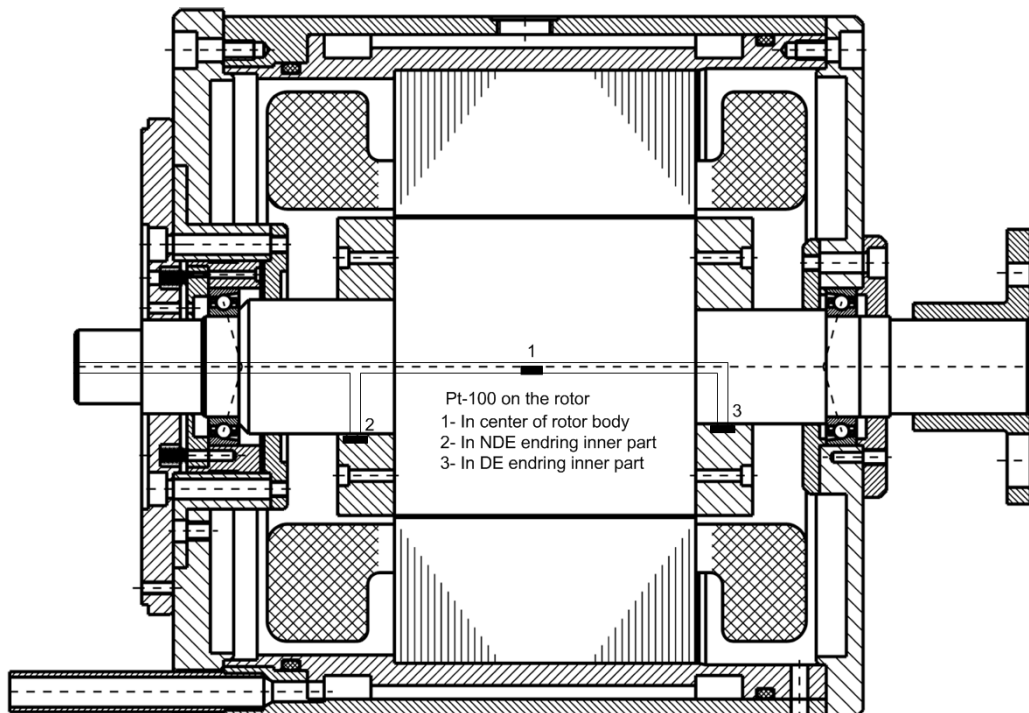


Figure 5.14: Mounted temperature sensors (Pt-100) on the rotor parts.

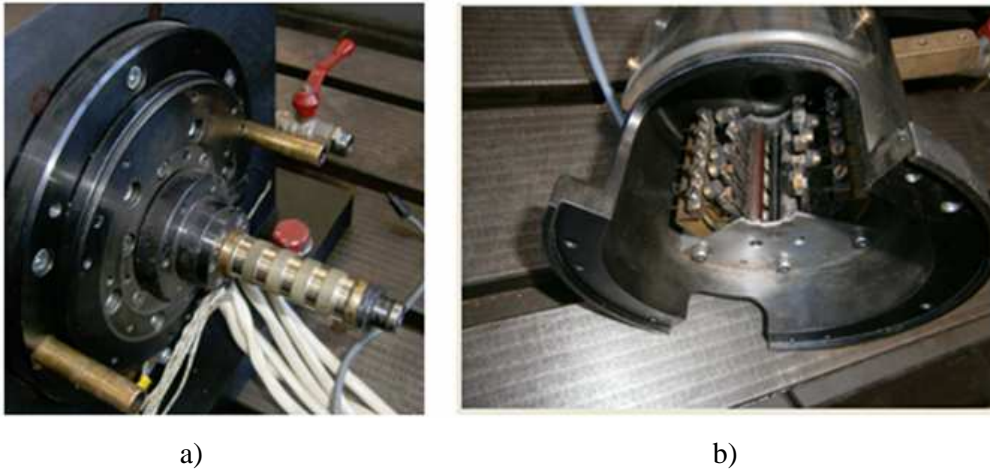


Figure 5.15: Slip-ring arrangement for the rotor temperature measurement [29]: a) slip-rings and, b) brushes with the mounting holder.

5.5 High Speed Spindle Bearings

Bearings, which are implemented in high-speed machines, need to fulfil important requirements with regard to load carrying capability, running accuracy, high speed capability, rigidity, vibration behaviour and available space. The first natural bending frequency of the rotor must be at least 30 % higher than the maximum rotational frequency of the rotor to avoid the excitation of a bending vibration resonance by the residual unbalance force. To get a high natural bending frequency, the space between the two bearings is made to be minimum (180mm), as shown in the illustration Fig. 5.1. Since the bearings are not ideally rigid, the natural bending frequency is typically 10 % lower than for stiff bearings. For the given rotor, the first natural bending frequency was roughly estimated as in (5.3) $f_b = 1390$ Hz, with a corresponding natural bending critical speed $\omega_c = 8737$ s⁻¹ much less than the rotor nominal angular speed $\omega_r = 2513$ s⁻¹ [34].

$$f_b = \frac{1}{2 \cdot \pi} \cdot \sqrt{\left(\frac{d_r}{D_r}\right)^4 \cdot \frac{3 \cdot E \cdot D_r^2}{\rho \cdot l_r^4}} \quad (5.3)$$

In (5.3) E is the *Young's* modulus, D_r and d_r are outer and inner diameters of the rotor respectively, l_r is the length of the rotor core including the end-rings and ρ is mass density. For the high speed application high precision with angular contact 15° ball spindle-bearings are used (Type: *SKF 71906 CD*). These bearings have an outer ring shoulder guided cage, made of a glass fibre reinforced material called *polyetheretherketone* (PEEK). These light-weight cages keep centrifugal forces low and are designed to enable a good lubricant supply to the ball contact areas, as shown in Fig. 5.15. These bearings are designed with grease lubricant can be implemented up to the maximum speed of 30000/min with a speed factor of $n \cdot d_{b,av} = 1.155 \cdot 10^6$ mm/min [24], [33]. The lubrication was applied once for the lifetime operation and maintenance free under normal operation condition. Before the bearings are mounted, the bearing seats are coated with a synthetic

polytetrafluoroethylene (PTFE) which is commonly known with its brand name *TEFLON*. Due to the low friction coefficient of *PTFE*, the bearings can operate with lowest friction moment. In addition, above the *TEFLON*, the seats are coated with a *MOLYKOTE* dispersion product *M55 plus*, which is a quick acting penetrating agent. It is used for corrosion protection, increasing load carrying capacity and reducing wear. According to the motor shaft diameter, the following bearing dimensions: bore diameter $d_b=30$ mm, outer diameter $D_b=47$ mm, bearing width $b_b=9$ mm were selected and implemented. As it was shown in section 3.5.2, that the applied radial and axial bearing loads were calculated to be $F_r=60$ N and $F_a=283$ N respectively with the actual axial preload of 94 N They attain the maximum possible speed with a small space for installation. The large number of balls, which are 20, of reduced size, used in these bearings, has the positive effect of an increased stiffness and ensures a lower rolling friction. The single row angular contact ball bearings can accommodate axial forces in one direction only and are therefore mounted oppositely (see Fig.5.8), facing each other in a back to back bearing arrangement, which provides a relatively stiff bearing load characteristic.



Figure 5.16: High speed bearing components [52].

6 Testing of Solid Rotor Prototype Motors

The constructed 4- and 2-pole prototype solid rotor induction motors were tested to confirm the validation of the *FLUX 2D* FEM simulation results. The time harmonics of the current, caused by inverter supplied modulated voltage, are well damped by a low pass LC sine filter, which gives an almost sinusoidal current supply to the motor terminals. Due to this sinusoidal current, it was possible to make a comparison of the measured and the simulated characteristics at sinusoidal voltage supply, because in both cases the current system was close to a symmetrical three-phase sinusoidal system.

6.1 Test Bench Overview

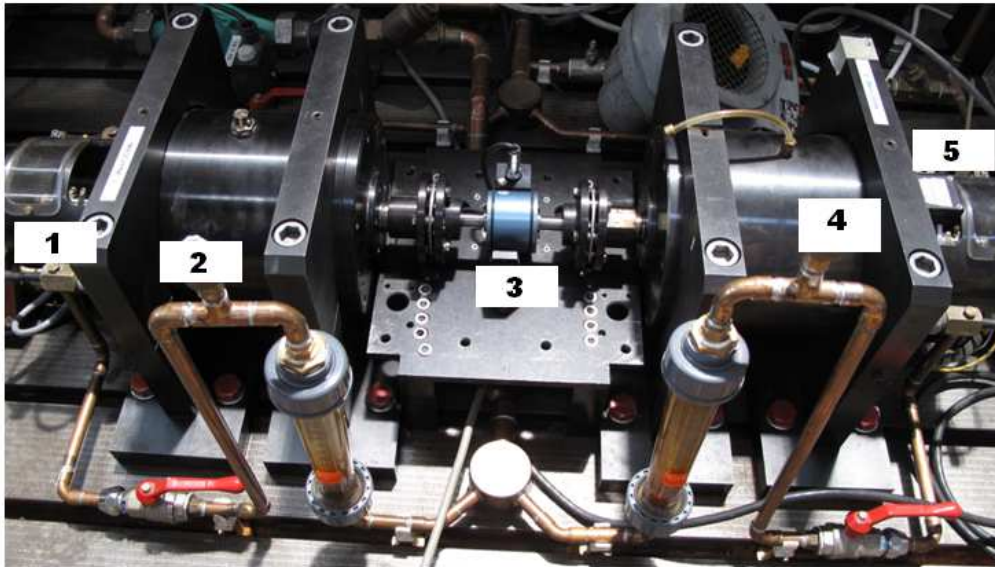


Figure 6.1: Test-rig for high speed motors with 24000 /min, 30 kW: 1) slip rings for rotor temperature measurement, 2) solid rotor induction machine to be tested, 3) mechanical coupling via a torque sensor, 4) permanent magnet synchronous machine as a load and 5) incremental encoder for the operation of 4).

Figure 6.1 shows the constructed test bench at the laboratory of the *Institute of Electrical Energy Conversion, Darmstadt University of Technology* [24]. In the test rig the examined machine is taken in operation from no-load to loading condition. The left-side machine is the solid rotor induction motor with a voltage source pulse width modulation (PWM) converter system *SIMODRIVE 611u* [51]. As a load machine, a permanent magnet synchronous machine (PMSM) [33] with the same power rating and construction volume as the tested SRIM is used [65], [66], [67].

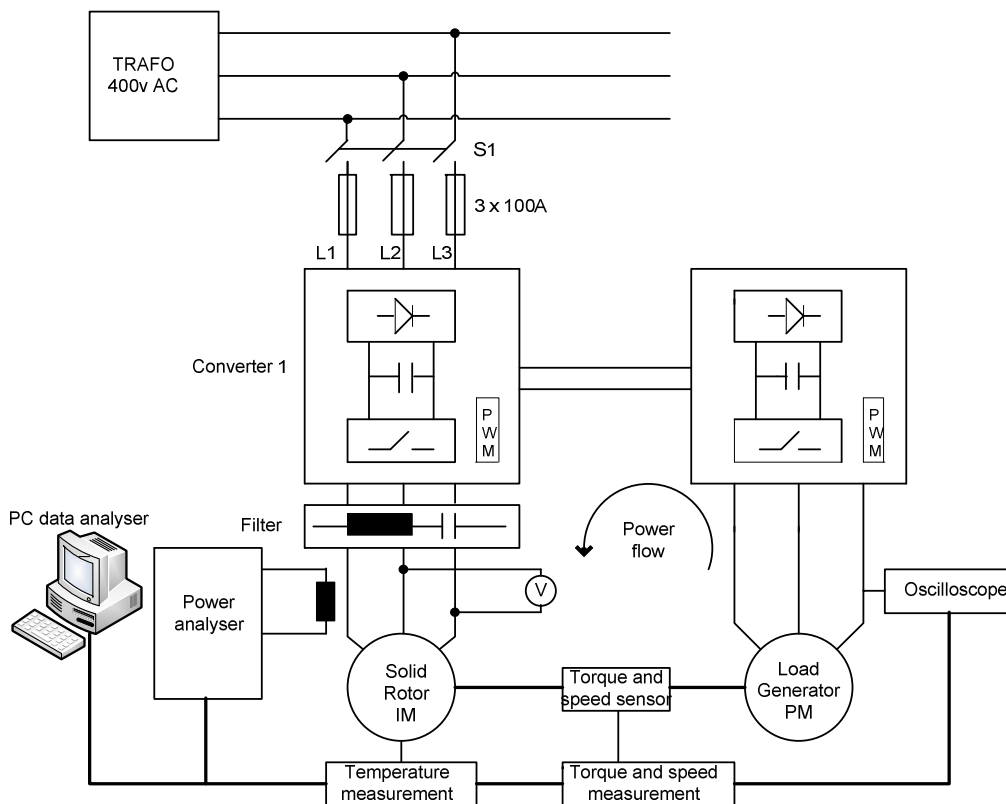


Figure 6.2: Basic setup of the test bench.

The performance characteristics of the prototype solid rotor motors are measured, using the measurement arrangement of Fig. 6.2. During the load tests the shaft of the SRIM and the load PMSM are mechanically coupled via a torque measurement sensor. The output of the load machine inverter is supplied back into the tested motor inverter DC link, as indicated in the power flow diagram of Fig. 6.2. Due to

this back-to-back configuration, only the losses of the system were taken from the grid.

6.2 Converter System Voltage Supply

The *SIMODRIVE 611u* converter system is a modular system, which comprises a line filter, a commutating reactor, infeed modules, motor-side power modules, control units and a cooling system as shown in the Fig. 6.3. It is used as a power supply with variable amplitude of the fundamental sine wave voltage and its corresponding variable frequency. The converter system is designed for direct operation at the grid with rated voltages of 400 V, 415 V and 480 V, as a 3-phase AC system. A low resistance galvanic connection is necessary between the reference potential to ground of the feeding grid and the protective conductor potential of the electrical inverter equipment [51].

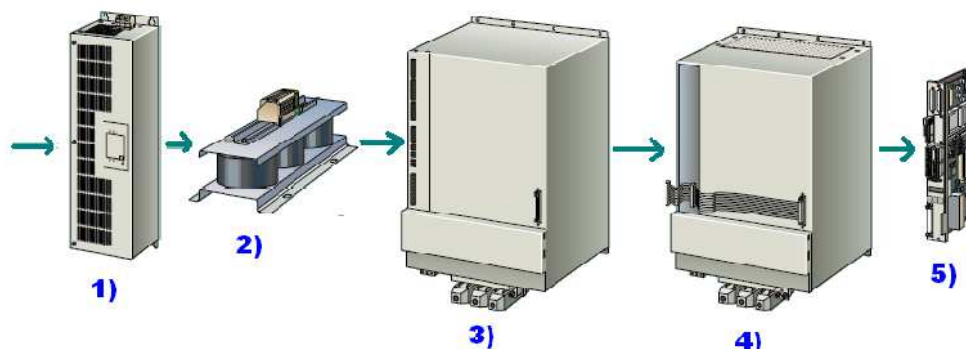


Fig 6.3: *SIMODRIVE 611 universal* converter system: 1) line filter, 2) commutating reactor, 3) in-feed/ regenerative feedback module, 4) power module, 5) control unit [51].

The line filter works together with the reactor coil to restrict the conducted interference, emitted from the power module, to the limit value and to effectively protect the converter system against line-side disturbances. The damping characteristic of the wideband filter for the converter power supply does not only

conform with requirements of electromagnetic compatibility (EMC) standards for the frequency range of 150 kHz to 30 MHz, but also includes a filtering of low frequencies up to 2 kHz. As a result, the line filter has an extended scope of functions, which means that it can, to a certain extent, be used regardless of the machine installation location, where the line properties (e.g. line impedance) are usually unknown. The line commutating reactance has to limit the current harmonics, fed back to the line supply, and has to store energy for the dc link controller operation in conjunction with the infeed and regenerative feedback modules. The in-feed module is used to connect the drive group to the power supply. The in-feed module rectifies the supply voltage and generates the dc voltage for the dc link from a 3-phase, 400V/AC $\pm 10\%$, 50Hz line supply. In addition, the electronic voltages ($\pm 24\text{ V}$, $\pm 15\text{ V}$, $\pm 5\text{V}$) for the control supply are made available to the drive module and the *SINUMERIK 840D* control via the equipment bus. The power module together with the control unit forms the total drive module.

The drive is parameterized and started via the *Simocom U* start-up software tool for personal computers, shown in Fig.6.4. In addition, the *Simocom U* performs the following tasks: i.e. checking the wiring by going into the online help connection diagrams, establish a connection to the drive to be parameterized, change parameters, boot the board, optimize the speed and current controller parameters, simulate terminal signals and enabling a diagnose of the drive status. The parameter changes in *Simocom U* are not automatically saved in the converter memory. Hence, the optimized drive settings must be saved in the converter Flash Erasable Programmable Read Only Memory (FEPRM) [51].

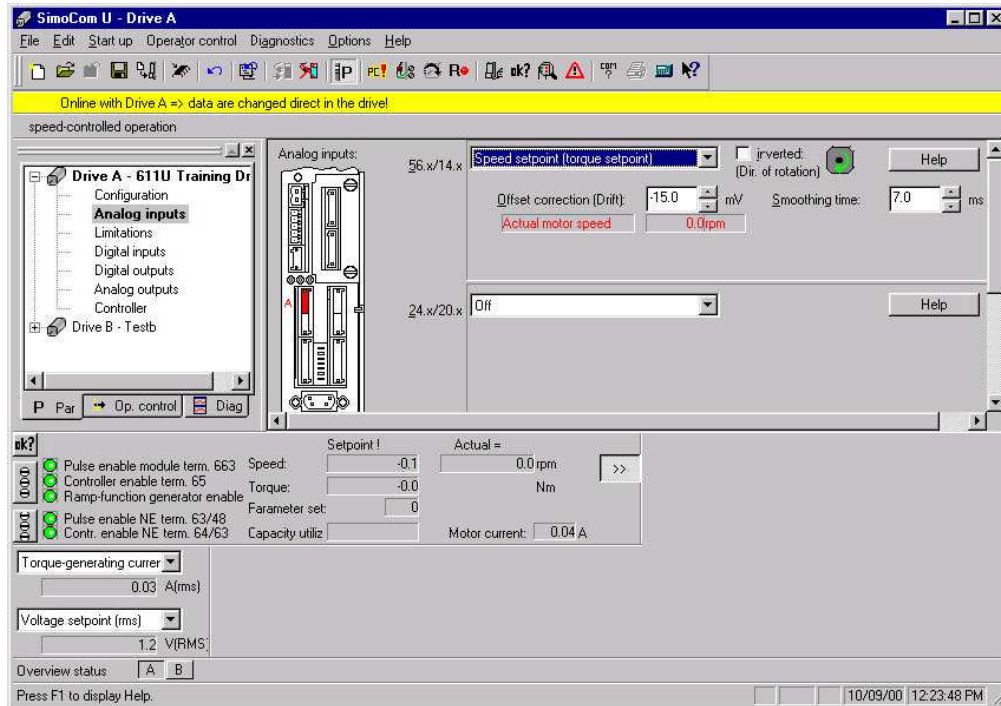


Figure 6.4: *Simocom U* starting and configuring software tool for *SIMODRIVE 611u* [51]

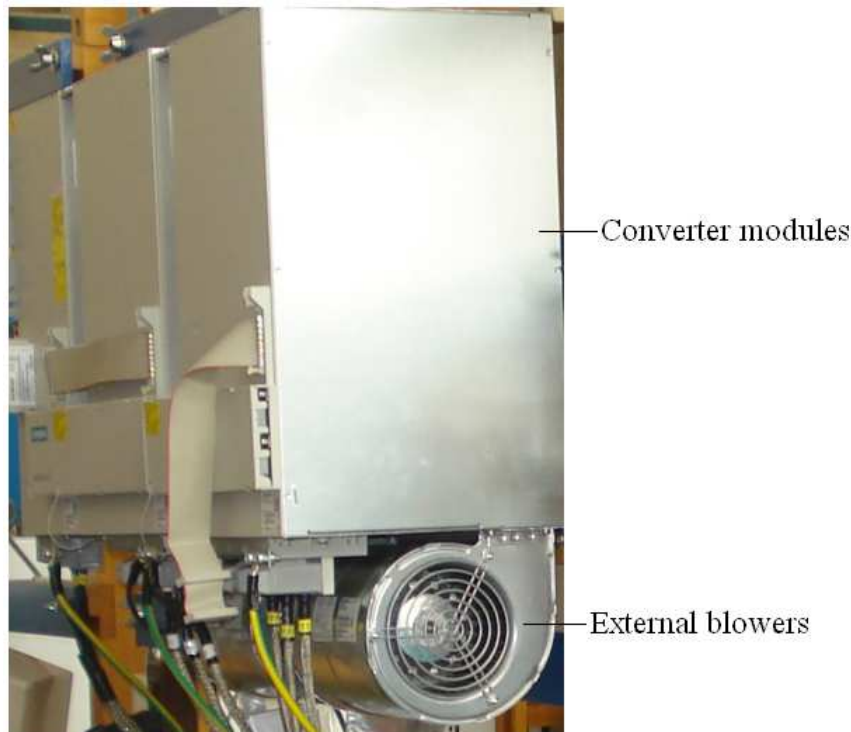


Figure 6.5: *SIMODRIVE 611u* cooling system [51].

The converter cooling is accomplished by separate fans, specially designed for the system, as shown in Fig. 6.5. With this cooling system, the power module losses are dissipated externally as heat, whereas the power loss of the control unit is dissipated internally. The external heat sink, as a mechanical interface, allows a degree of protection of IP54. The basic voltage source pulse width modulation (PWM) inverter system circuit is shown in Fig. 6.6. The dc voltage U_d is switched in the 3-phase PWM inverter by six IGBT and six free-wheeling diode switches in order to obtain pulses, forming the three phase AC voltages of the required fundamental frequency and fundamental voltage amplitude for motor supply as a U/f -control, as shown on Fig. 6.7 [34]. The IGBT is a semiconductor switch, which combines the advantageous properties of the power MOSFET and the bipolar transistor technology. Like a MOSFET, the gate of the IGBT is insulated and its driving power is low. It has also a similar conducting voltage as that of a bipolar transistor.

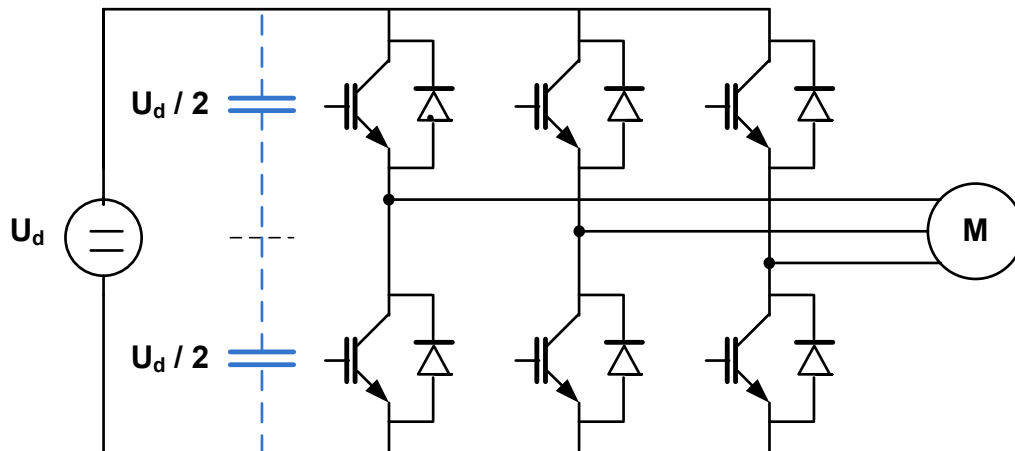


Figure 6.6: Two-level voltage source PWM inverter system.

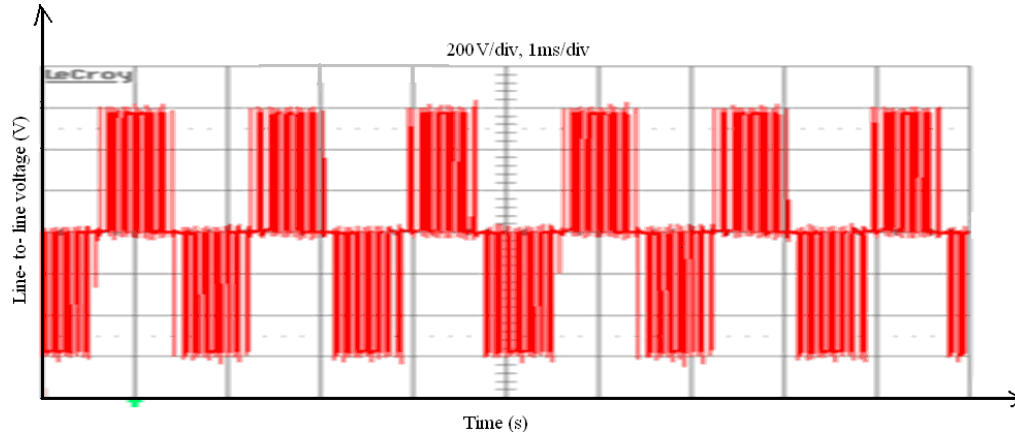


Figure 6.7: Measured PWM voltage output phase-phase at $f_s = 600$ Hz fundamental frequency and $f_T = 8$ kHz switching frequency, dc link voltage $U_d = 600$ V.

6.3 L-C Sine Filter

When the 4-pole axially slitted, radially grooved solid rotor induction motor with copper end rings was operated at no-load without any motor side filter, its rotor temperature increased rapidly, because of the very high rotor eddy current losses [67]. Generally, these losses are high due the current ripple, supplied from the converter system (*SIODRIVE 611u*), in addition to the higher space harmonics of the magnetic air-gap field. A switching frequency of 8 kHz causes a current ripple of 16 kHz (Fig. 6.10). Thus, the stator current and current-excited magnetic fields not only oscillate with fundamental frequency, but also, depending on the inverter switching frequency, with higher harmonic frequencies. The interaction of the fundamental stator air gap magnetic wave, which is excited by the fundamental current component at fundamental inverter frequency with the rotor current, results in the generation of the driving electromagnetic torque. The air gap field waves of the higher harmonic stator currents are rotating much faster than the rotor, which induce high frequency eddy current losses [11]. Hence, in order to overcome inverter switching caused rotor eddy current losses, the current ripple is filtered by a low pass L - C sinusoidal filter [21], [54] which leads to an almost sinusoidal line

current at motor side Fig. 6.10c. Hence, the no-load and load tests were performed with a sinusoidal L - C filter, connected in series, as shown in Fig. 6.8.

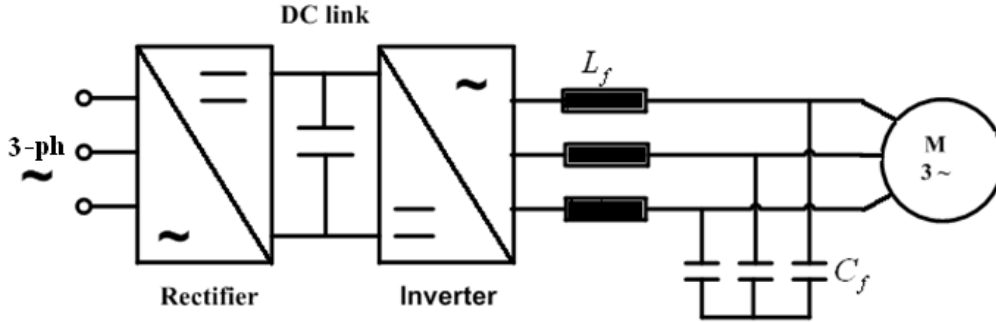


Figure 6.8: Schematic connection diagram of a series L - C sinusoidal filter with L_f (filter inductance) and C_f (filter capacitance).

The analysed solid rotor motors with a series L - C sinusoidal filter can be ideally represented with the per-phase T-Equivalent circuit, as shown in Fig. 6.9a. The motor inductance is estimated from the load test without the filter, for which the motor T-equivalent circuit is replaced by equivalent input impedance ($Z_{eq} = R_{eq} + jX_{eq}$) of the machine, Fig. 6.9a. Accordingly, the per-phase equivalent impedance for the fundamental harmonic parameters ($Z_{ph,HO1}$) is determined from the load test of the 4-pole SRIM at $f_s = 400$ Hz, $M_e = 5.8$ Nm, $n = 11959$ min⁻¹, as given in (6.1) and in Table 6.1. The values R_{eq} , X_{eq} depend on the slip s .

$$\underline{Z}_{eq} = \underline{Z}_{Ph,HO1} = \frac{U_{ph,HO1}}{I_{ph,HO1}} = Z_{Ph,HO1} \cdot (\cos \varphi + j \sin \varphi) \quad (6.1)$$

$$R_{eq} = Z_{eq} \cdot \cos \varphi, \quad (6.2)$$

$$X_{eq} = Z_{eq} \cdot \sin \varphi. \quad (6.3)$$

Hence, using the test data of Table 6.1, the equivalent motor inductance ($L_{eq} = 0.7$ mH) at the operating frequency $f_s = 400$ Hz is determined as in (6.4):

$$L_{\text{eq}} = \frac{X_{\text{eq}}}{2\pi f_s} \quad (6.4)$$

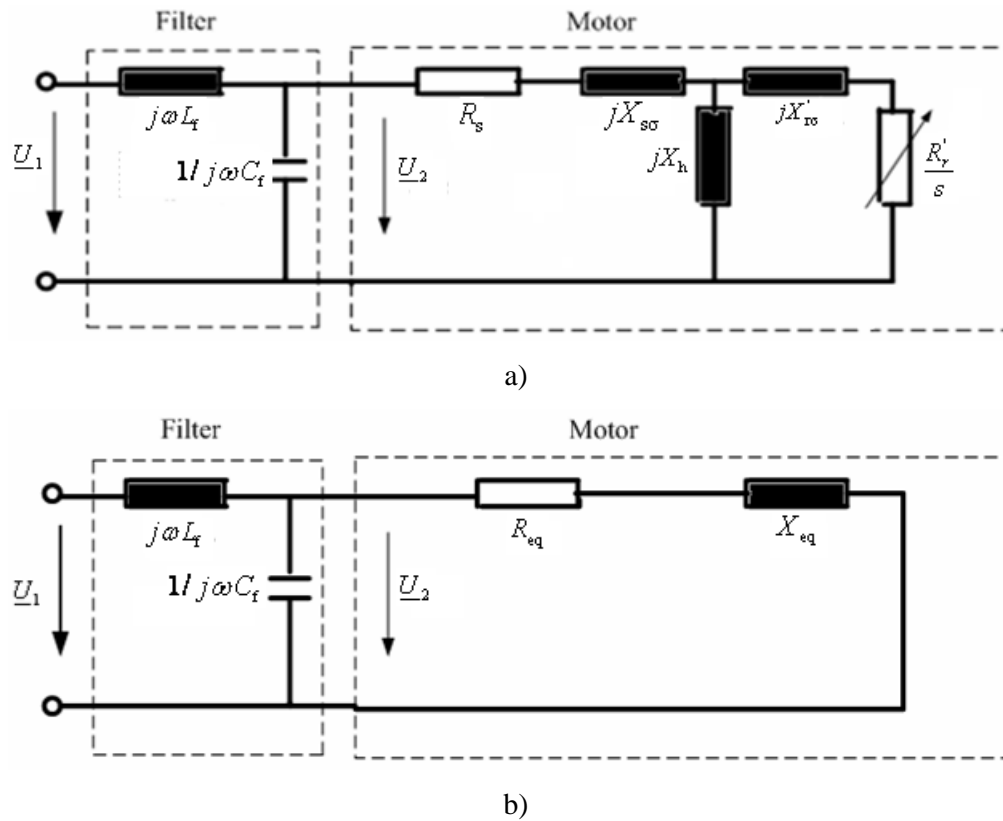


Figure 6.9: Induction motor T- equivalent circuit a) with a series low pass L-C sinusoidal filter, b) representation of the motor equivalent circuit as an equivalent impedance (Z_{eq}).

Table 6.1: Load test results of the 4-pole SRIM at $f_s = 400\text{Hz}$ (per-phase values) at the slip $s = 0.34\%$ (HO1: harmonic order 1)

$\frac{U_{\text{ph}}}{\text{V}}$	$\frac{U_{\text{ph,H01}}}{\text{V}}$	$\frac{I_{\text{ph}}}{\text{A}}$	$\frac{I_{\text{ph,H01}}}{\text{A}}$	$\frac{Z_{\text{ph,H01}}}{\Omega}$	$\frac{\varphi_{\text{H01}}}{^\circ}$
189	112	59.5	57.6	1.95	63

From the considered T-equivalent circuit of the motors (Fig. 6.9a), the voltage ratio of the filter as a function of the operating frequency is given in (6.5).

$$\frac{U_2}{U_1} = \frac{1}{\sqrt{\left(1 - \omega^2 L_f C_f + \frac{\omega^2 L_f L_{eq}}{R_{eq}^2 + (\omega L_{eq})^2}\right)^2 + \frac{\omega^2 L_f^2 R_{eq}^2}{(R_{eq}^2 + (\omega L_{eq})^2)^2}}} \quad (6.5)$$

Since $R_{eq}^2 \ll (\omega \cdot L_{eq})^2$ the voltage ratio can be approximately calculated as :

$$\frac{U_2}{U_1} \approx \frac{1}{1 - \omega^2 L_f C_f + \frac{L_f}{L_{eq}}} \quad (6.6)$$

As a result of it, the resonance frequency $f_{res} = 2.7$ kHz is calculated as in (6.7)

$$f_{res} = \frac{\omega_{res}}{2\pi} = \frac{1}{2\pi\sqrt{L_f C_f}} \cdot \sqrt{1 + \frac{L_f}{L_{eq}}} \quad (6.7)$$

Using the filter designed parameters ($L_f = 80 \mu\text{H}$, $C_f = 40 \mu\text{F}$), it is seen, that the sinusoidal current is supplied at the motor terminals as shown in Fig.6.10c. Higher harmonic current components are well damped, resulting in an almost sinusoidal current, which is supplied at the motor terminals, as shown in Fig. 6.10c. It is also pointed out, that $L_f = 80 \mu\text{H} \ll L_{eq} = 700 \mu\text{H}$, which implies that the resonance frequency f_{res} can be approximately determined as in (6.8).

$$f_{res} = \frac{1}{2\pi\sqrt{L_f C_f}} \quad (6.8)$$

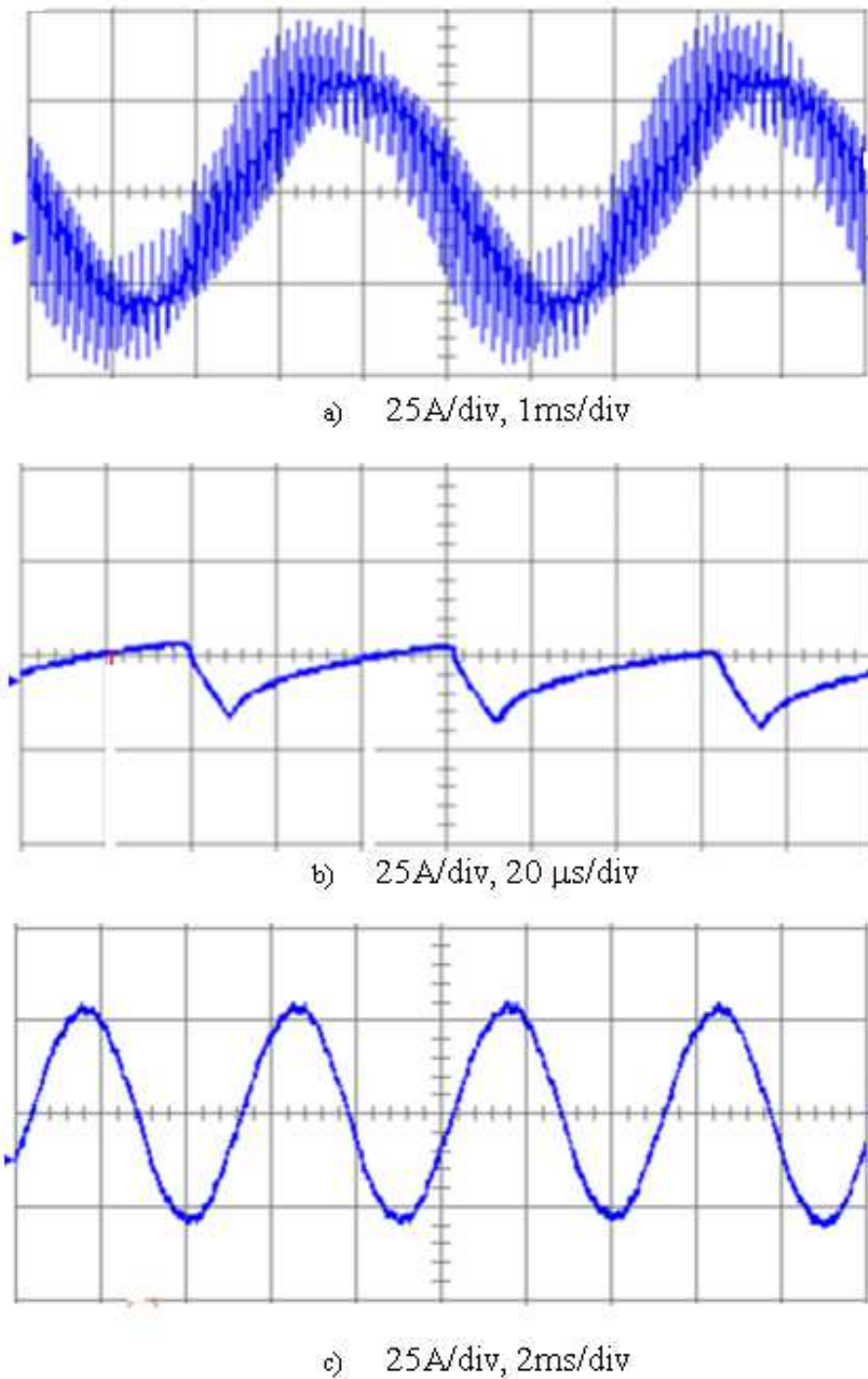


Figure 6.10: Measured motor current wave form of a 4-pole SRIM a) before the filter and b) current ripple with double switching frequency 16 kHz c) after the filter on the motor side with *Rotor A* at no-load and at line-to-line fundamental voltage $U_s = 165$ V and $f_s = 200$ Hz.

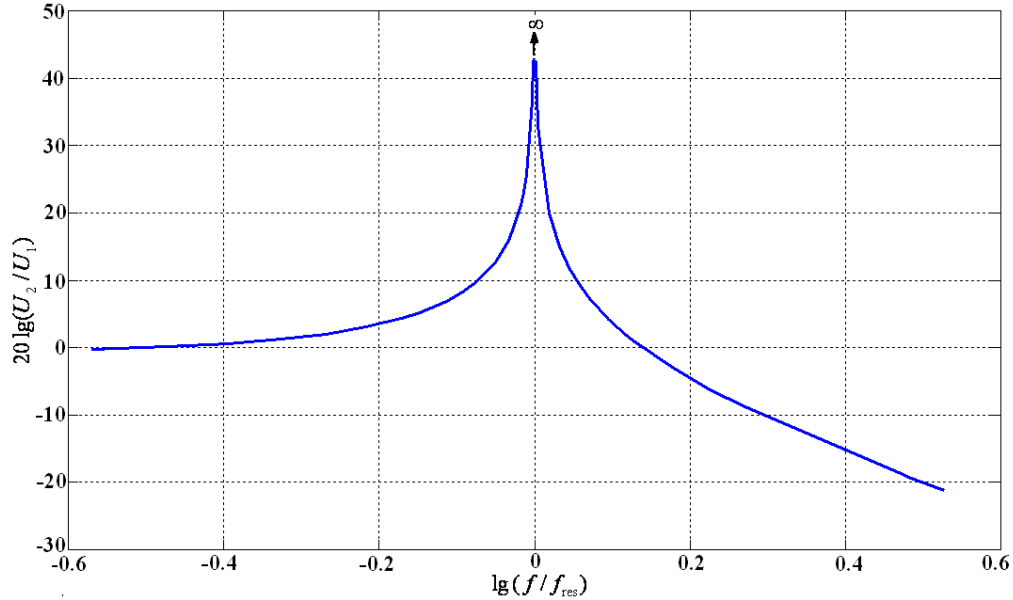


Figure 6.11: Amplification factor in dB of an ideal, undamped sinus filter as a function of the frequency according to the relation in (6.6).

6.4 Test Results

The 4-pole stator with the first version, axially slitted solid rotor with copper end rings (*Rotor A*), shown in Fig. 5.8a, is tested, using the sinusoidal filter in series to supply a sine wave current. After analyzing the test results and in accordance with the FEM simulated results, the rotor geometry was modified to *Rotor B* (Fig.5.8b), and the motor was tested again with *Rotor B*. The same *Rotor B* was implemented for testing of the 2-pole SRIM variant. The geometrical parameter values of both rotors, *Rotor A* and *Rotor B*, are given in Table 5.3 in Chapter 5.

6.4.1 Four-pole SRIM Test Results

The test results of a 4-pole SRIM with both rotor versions (*Rotor A* and *Rotor B*) for the operating fundamental frequency of $f_s = 400\text{Hz}$ ($n_{\text{syn}} = 12000\text{min}^{-1}$) are presented in the characteristics Fig. 6.12 - Fig. 6.14, which show that the 4-pole motor with *Rotor B* (with radial grooves, higher air-gap distance and deeper rotor slits) has less rotor losses and thereby is operated at a higher efficiency. But the input currents with *Rotor B* are higher than with *Rotor A* due to the high magnetizing current, caused by the wider radial air-gap distance. Accordingly, the fundamental power factor $\cos\varphi_{\text{H01}}$ of the motor with *Rotor B* is lower. The directly measured efficiency was calculated from the ratio of mechanically measured output power and electrically measured input power (without the losses in the filter). The strong increase of the rotor temperature due to the high rotor losses did not allow to operate the motor with rated torque 12 Nm even for a short time. All load points in Fig. 6.12 ÷ 6.14 could not be operated at steady-state as the temperature rise was too high.

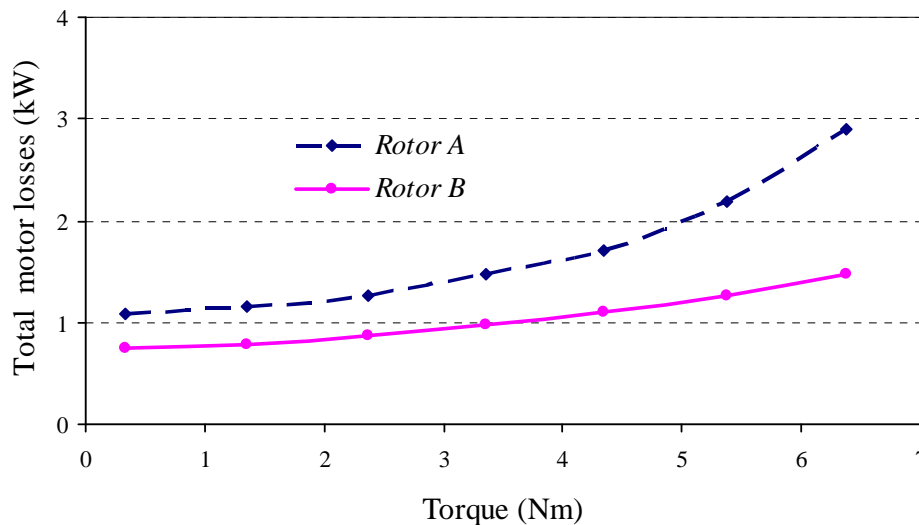
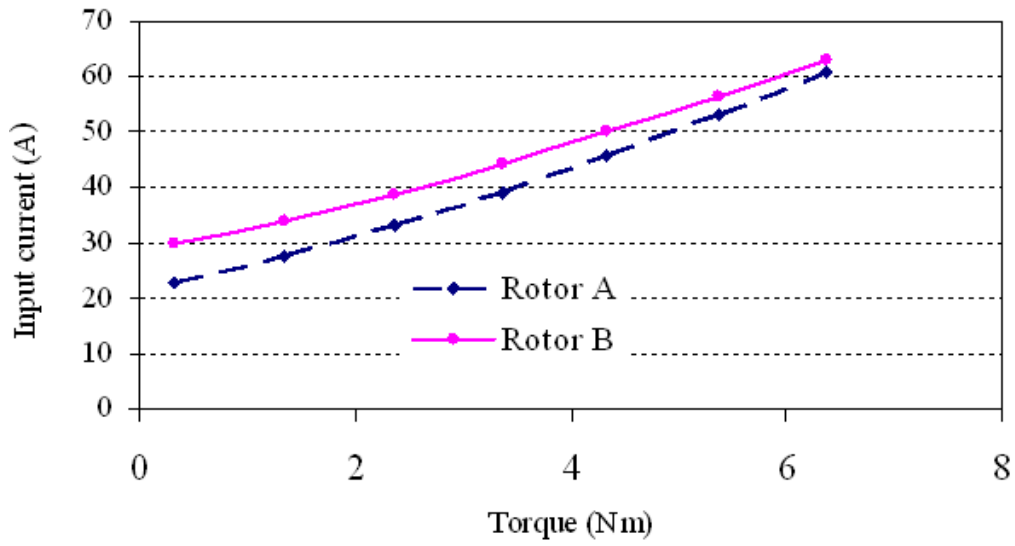
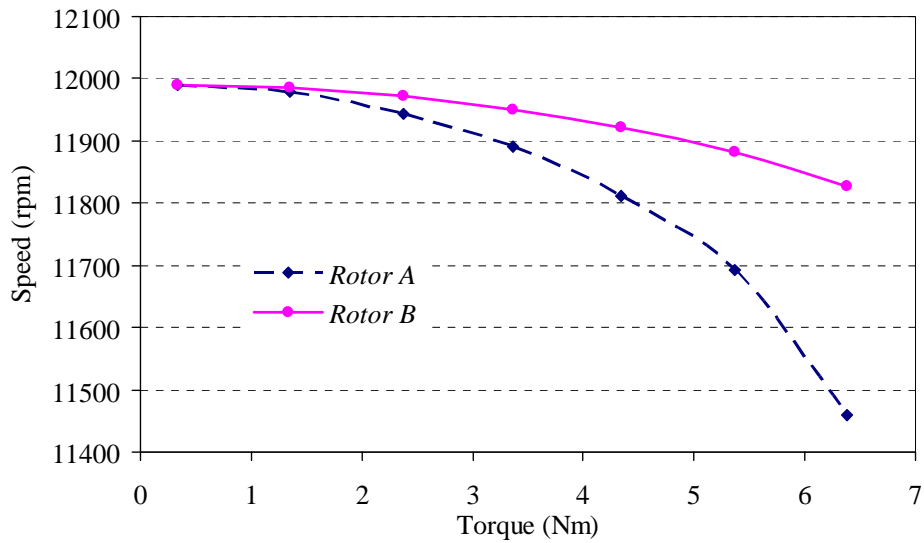


Figure 6.12: Measured total losses of the 4-pole SRIM with the two different rotor types *A* and *B* at the fundamental line-to-line voltage $U_s = 165\text{V}$ and $f_s = 400\text{ Hz}$ (Rated torque 12Nm).

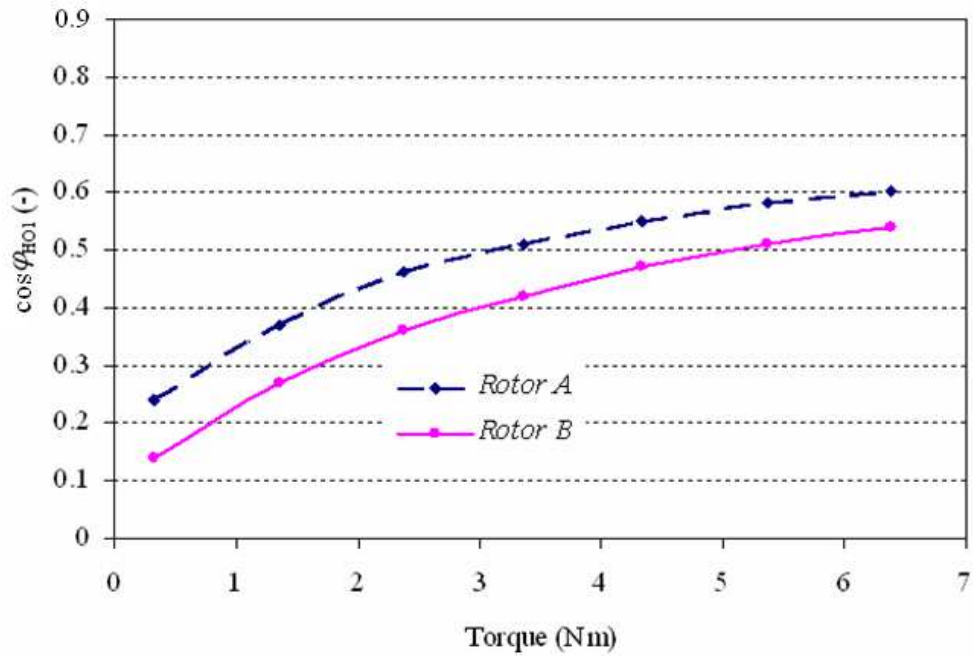


a)

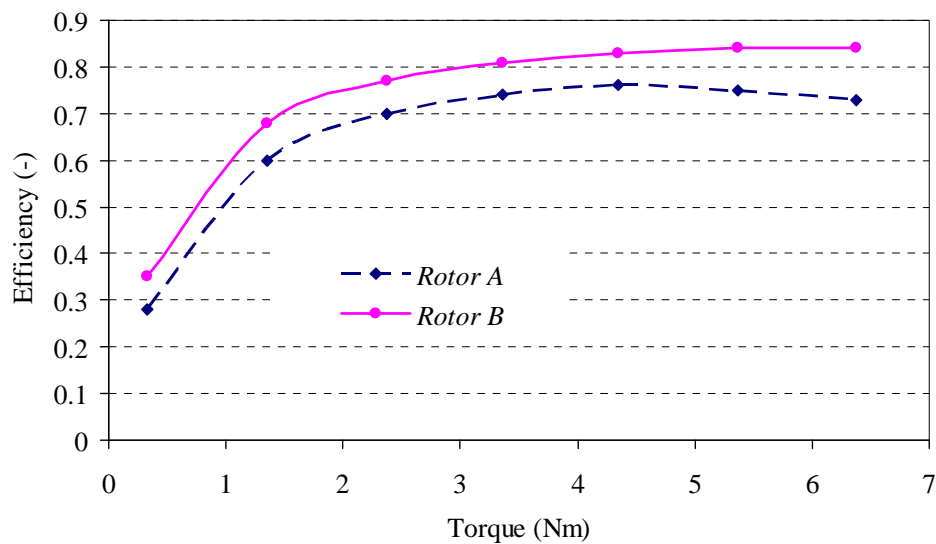


b)

Figure 6.13: Measured load performance characteristics of the 4-pole SRIM at the fundamental line-to-line voltage $U_s = 165$ V and $f_s = 400$ Hz : a) input current and b) operating speed as a function of load torque (Rated torque 12Nm).



a)



b)

Figure 6.14: Measured output performance characteristics of the 4-pole SRIM with the two rotor types A and B at the fundamental input frequency $f_s = 400\text{ Hz}$ and the line-to-line voltage $U_s = 165\text{ V}$, a) fundamental power-factor and b) directly measured efficiency.

The no-load and load output characteristics of the 4-pole axially slitted, radially grooved SRIM were performed and analysed with *Rotor B*. At the no-load test, the motor is made to run with almost no torque counteracting the driving motor torque, except the frictional torque, that must be overcome. Hence a linear no-load characteristic $U \sim f$ is obtained (Table 6.2). At the load test, the machine is coupled with the load PMSM of the same constructional volume [33] via a torque measurement sensor in a back-to-back arrangement. A load torque is applied to the tested SRIM by operating the load PMSM as generator in torque controlling mode. All the input electrical and output mechanical parameters are measured and analysed (Table 6.3).

Table 6.2: No-load test results of the 4-pole SRIM with *Rotor B* and Y-connection of the stator winding

$\frac{U_{s,HO1}}{V}$	$\frac{f_s}{Hz}$	$\frac{n}{\text{min}^{-1}}$	$\frac{I_{s,HO1}}{A}$	$\frac{P_{el,in}}{W}$	$\frac{P_{el,in,HO1}}{W}$	$\frac{\cos \varphi_{HO1}}{-}$
25	66.7	1993	27.2	420	375	0.11
55	133.3	3990	30.6	834	792	0.10
83	200.0	5996	30.8	1341	1308	0.10
112	266.7	7987	31.2	1950	1923	0.11
139	333.3	9985	31.2	2658	2631	0.12
167	400.0	11988	31.2	3459	3432	0.12
207	500.0	14978	31.0	4848	4821	0.14
246	600.0	17979	30.8	6480	6450	0.16
271	666.7	19973	30.5	7707	7674	0.18
300	733.3	21966	30.1	8946	8913	0.19
330	800.0	23963	30.6	10521	10482	0.20

Table 6.3: Load test results of the 4-pole SRIM with *Rotor B* at the fundamental frequency $f_s = 500$ Hz, line-to-line voltage $U_s = 206$ V, Y

$\frac{M}{\text{Nm}}$	$\frac{n}{\text{min}^{-1}}$	$\frac{I_{s,\text{HO1}}}{\text{A}}$	$\frac{P_{\text{el.in}}}{\text{W}}$	$\frac{P_{\text{el.in,HO1}}}{\text{W}}$	$\frac{\cos \varphi_{\text{HO1}}}{-}$
0.1	14984	30.9	1641	1607	0.15
1.0	14954	34.2	3121	3090	0.26
2.0	14918	38.6	4873	4842	0.35
3.0	14864	43.5	6380	6350	0.41
4.0	14801	49.4	8266	8235	0.47
5.0	14740	55.1	9969	9939	0.50

Table 6.4: Measured temperature of different machine parts of the 4-pole SRIM with *Rotor B* at the fundamental frequency $f_s = 500$ Hz, line-to-line voltage $U_s = 206$ V Y and for short time operation

$\frac{M}{\text{Nm}}$	$\frac{\vartheta_{\text{Cu,s}}}{^\circ\text{C}}$	$\frac{\vartheta_{\text{overhang}}}{^\circ\text{C}}$	$\frac{\vartheta_{\text{H}_2\text{O-in}}}{^\circ\text{C}}$	$\frac{\vartheta_{\text{H}_2\text{O-out}}}{^\circ\text{C}}$	$\frac{\vartheta_{\text{rotor}}}{^\circ\text{C}}$
0.1	40.3	38.1	29.6	29.7	52.6
1.0	42.8	43.9	30.7	30.9	63.2
2.0	49.9	48.7	31.7	32.1	73.7
3.0	53.0	54.0	32.5	33.0	91.8
4.0	60.3	64.2	33.8	34.5	102.5
5.0	66.5	67.5	34.7	35.5	110.0

Table 6.5: Measured characteristics of the 4-pole SRIM with *Rotor B* at the fundamental frequency $f_s = 500$ Hz, line-to-line voltage $U_s = 206$ V

$\frac{M}{\text{Nm}}$	$\frac{s}{\%}$	$\frac{P_{\text{m.out}}}{\text{W}}$	$\frac{P_{\text{el.in}}}{\text{W}}$	$\frac{P_{\text{d,total}}}{\text{W}}$	$\frac{\eta}{\%}$
0.1	0.11	157	1641	1484	10
1.0	0.31	1566	3121	1555	51
2.0	0.55	3124	4873	1749	65
3.0	0.91	4670	6380	1710	74
4.0	1.33	6200	8266	2066	75
5.0	1.73	7718	9969	2251	78

6.4.2 Two-Pole SRIM Test Results

The no-load tests of the 2-pole and 4-pole solid rotor motors with *Rotor B* show the linear characteristics $U_s \sim f_s$ (fundamental values) up to the rated voltage $U_s = 330$ V (Fig. 6.16a). The no-load input power, which is supplied to overcome the no-load losses, is presented on the graph Fig.6.16b, which shows almost the same no-load losses for the 2-and for the 4-pole motor. The measured no-load input currents are sinusoidal, which are shown on the oscilloscope wave Fig. 6.15.

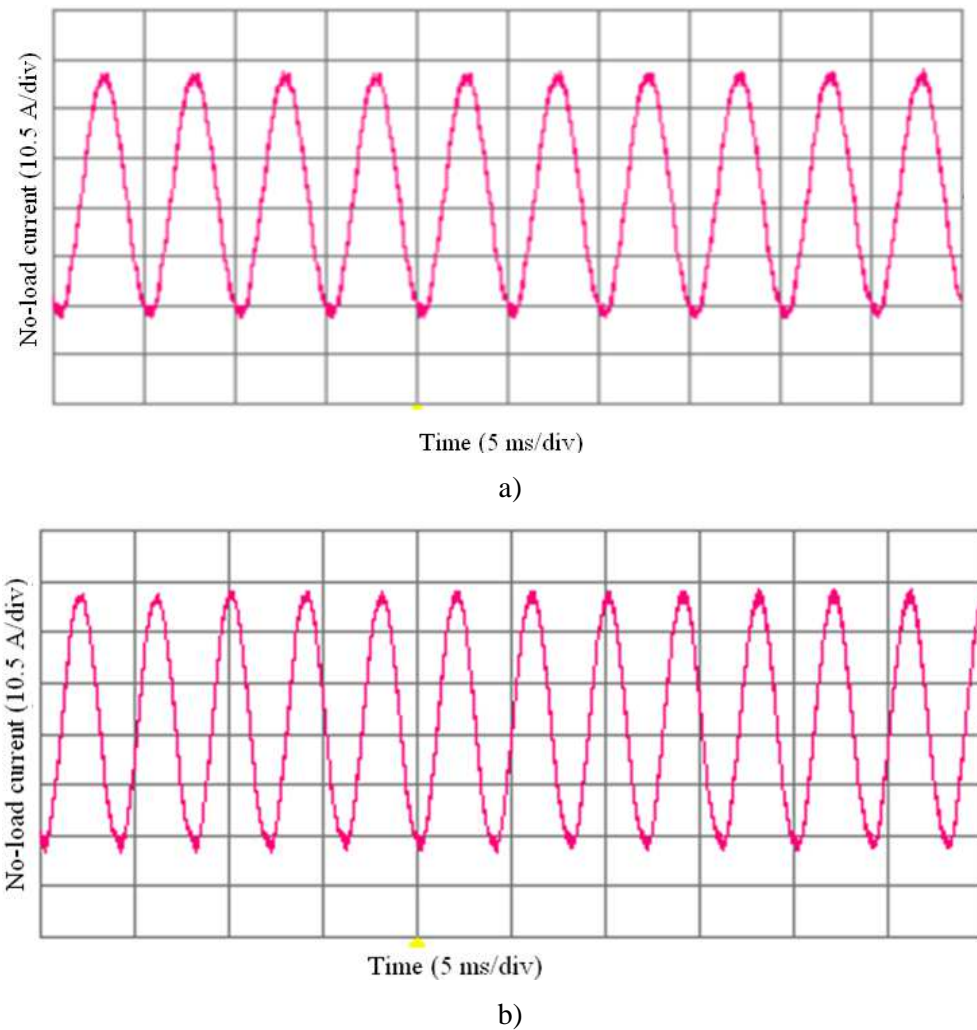
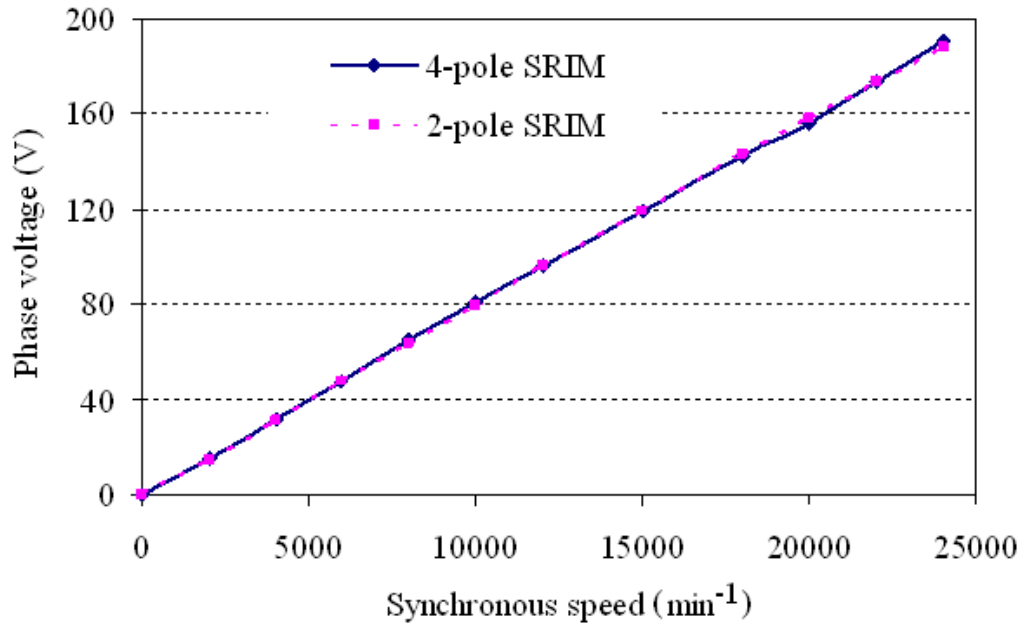


Figure 6.15 Measured no-load input current wave forms of the 2-pole SRIM with *Rotor B* for fundamental frequencies: a) $f_s = 200$ Hz and b) $f_s = 250$ Hz.

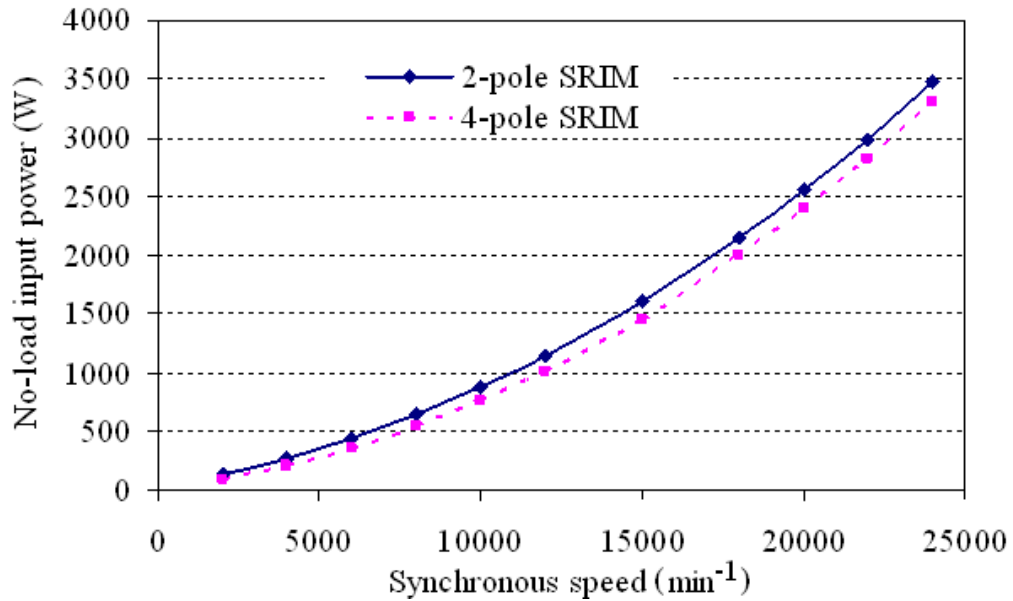
Table 6.6: No-load test results of the 2-pole SRIM with *Rotor B*

$\frac{U_{s,HO1}}{V}$	$\frac{f_s}{Hz}$	$\frac{n_{syn}}{\text{min}^{-1}}$	$\frac{I_{s,HO1}}{A}$	$\frac{P_{el,in,HO1}}{W}$	$\frac{\cos \varphi_{HO1}}{-}$
25	33.3	2000	14.0	249	0.14
54	66.7	4000	15.6	597	0.14
82	100.0	6000	16.1	1059	0.15
110	133.3	8000	16.4	1614	0.17
138	166.7	10000	16.7	2271	0.19
165	200.0	12000	16.9	3021	0.21
206	250.0	15000	17.1	4353	0.24
248	300.0	18000	17.4	6000	0.27
274	333.3	20000	17.6	7167	0.29
300	366.7	22000	17.7	8448	0.31
326	400.0	24000	17.9	9879	0.33

Fig. 6.18 shows the temperature rises of different parts of the 2-pole SRIM, from which it is seen that the machine is overheated after 7 min at rated operating frequency and at no-load, which endangers the normal operation of the bearing. Hence, all the load tests are performed for lower frequency, partial loading and for short time operation, as the water-jacket cooling of the stator was not sufficient to remove the high rotor losses. Hence, a direct rotor cooling via a hollow rotor shaft would have been necessary.



a)



b)

Figure 6.16: Measured no-load characteristics of a 4- and 2-pole solid rotor motors with *Rotor B*: a) fundamental phase voltage as a function of the fundamental frequency (U_s/f_s -characteristic), b) total electrical input power, which is supplied to overcome the total no-load losses.

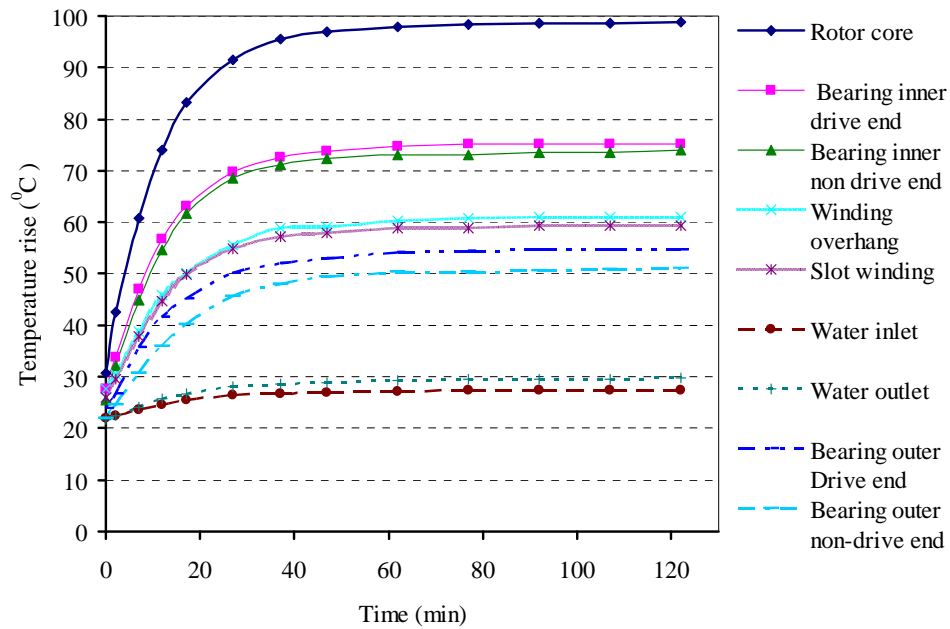


Figure 6.17: Measured temperature rises of different parts of the 2-pole SRIM with *Rotor B*, at no-load and at fundamental frequency $f_s = 200\text{Hz}$, $n_{\text{syn}} = 12000 \text{ min}^{-1}$.

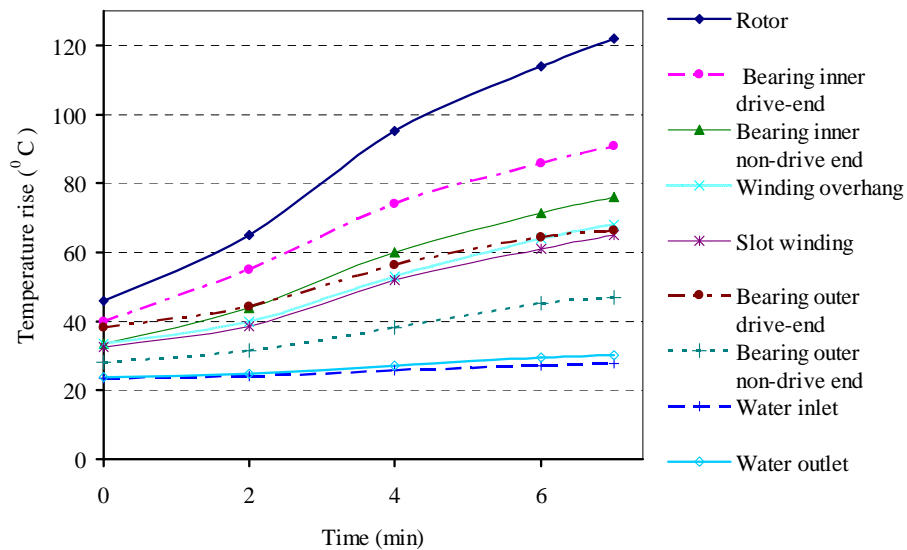


Figure 6.18: Measured temperature rises of different parts of the 2-pole SRIM with *Rotor B* at no-load and at fundamental frequency $f_s = 400\text{Hz}$, $n_{\text{syn}} = 24000 \text{ min}^{-1}$.

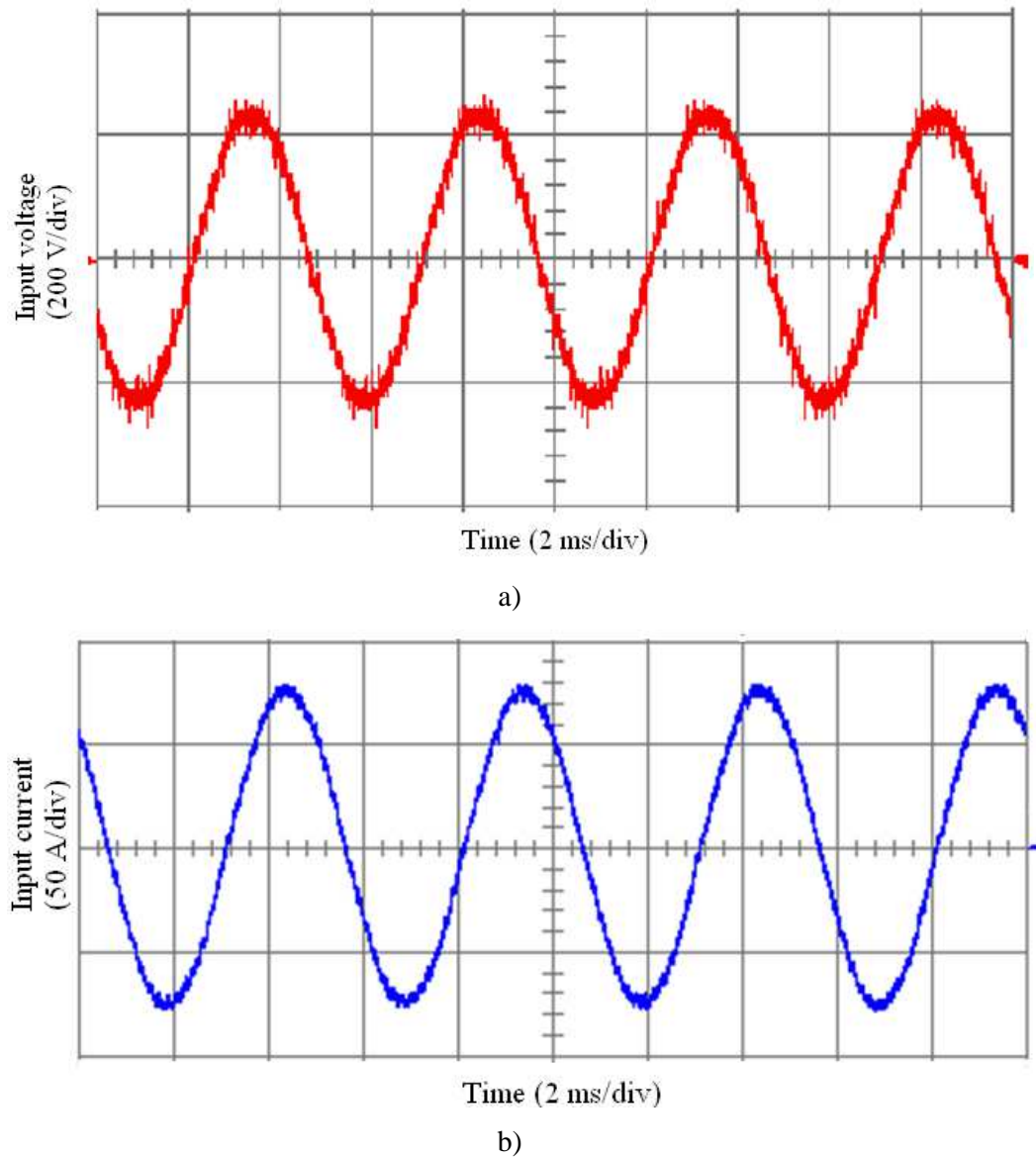


Figure 6.19: Measured wave forms of the 2-pole SRIM with *Rotor B* at fundamental line-to-line voltage $U_s = 165$ V, $f_s = 200$ Hz at the loading of $M_s = 8$ Nm: a) input line-to-line voltage, b) input line current.

Table 6.7: Load test results of the 2-pole SRIM with *Rotor B* at the fundamental frequency $f_s = 200$ Hz, (line-to-line voltage $U_s = 165$ V, Y)

$\frac{M}{\text{Nm}}$	$\frac{n}{\text{min}^{-1}}$	$\frac{I_s}{\text{A}}$	$\frac{I_{s,\text{HO1}}}{\text{A}}$	$\frac{P_{\text{el.in}}}{\text{W}}$	$\frac{P_{\text{el.in,HO1}}}{\text{W}}$	$\frac{\cos \varphi_{\text{HO1}}}{-}$
0.3	11990	16.8	16.8	1009	1002	0.21
1.0	11962	19.5	19.5	1986	1977	0.36
2.0	11942	24.1	24.1	3292	3285	0.48
3.0	11902	29.2	29.2	4634	4626	0.56
4.0	11862	34.8	34.8	6010	6000	0.62
5.0	11810	40.8	40.8	7432	7422	0.65
6.0	11745	46.9	46.9	8886	8877	0.67
7.0	11662	53.0	53.0	10348	10338	0.69
8.0	11582	59.1	59.1	11818	11808	0.71

Table 6.8: Measured temperature of different machine parts at load test of the 2-pole SRIM with *Rotor B* at the fundamental frequency $f_s = 200$ Hz, line-to-line voltage $U_s = 165$ V for short time operation

$\frac{M}{\text{Nm}}$	$\frac{\vartheta_{\text{Cu,s}}}{\text{°C}}$	$\frac{\vartheta_{\text{overhang}}}{\text{°C}}$	$\frac{\vartheta_{\text{H}_2\text{O-in}}}{\text{°C}}$	$\frac{\vartheta_{\text{H}_2\text{O-out}}}{\text{°C}}$	$\frac{\vartheta_{\text{rotor}}}{\text{°C}}$
0.3	29	30	21.7	21.5	46.0
1.0	33	34	22.5	22.3	53.6
2.0	37	38	23.3	23.2	61.2
3.0	42	43	23.9	23.9	68.9
4.0	45	46	24.4	24.5	73.0
5.0	51	52	25.0	25.1	82.0
6.0	57	58	25.7	25.8	93.2
7.0	64	65	26.2	26.5	107
8.0	74	75	26.7	27.3	120

Table 6.9: Measured output performance characteristics of the 2-pole SRIM with Rotor B at the fundamental frequency $f_s = 200$ Hz, line-to-line voltage $U_s = 165$ V

$\frac{M}{\text{Nm}}$	$\frac{s}{\%}$	$\frac{P_{m.out}}{\text{W}}$	$\frac{P_{el.in}}{\text{W}}$	$\frac{P_{d.total}}{\text{W}}$	$\frac{\eta}{\%}$
0.3	0.08	339	1009	670	34
1.0	0.32	1290	1986	696	65
2.0	0.48	2512	3292	780	76
3.0	0.82	3739	4634	895	81
4.0	1.15	4979	6010	1031	83
5.0	1.58	6190	7432	1241	83
6.0	2.13	7415	8886	1471	83
7.0	2.87	8598	10348	1750	83
8.0	3.48	9751	11818	2067	83

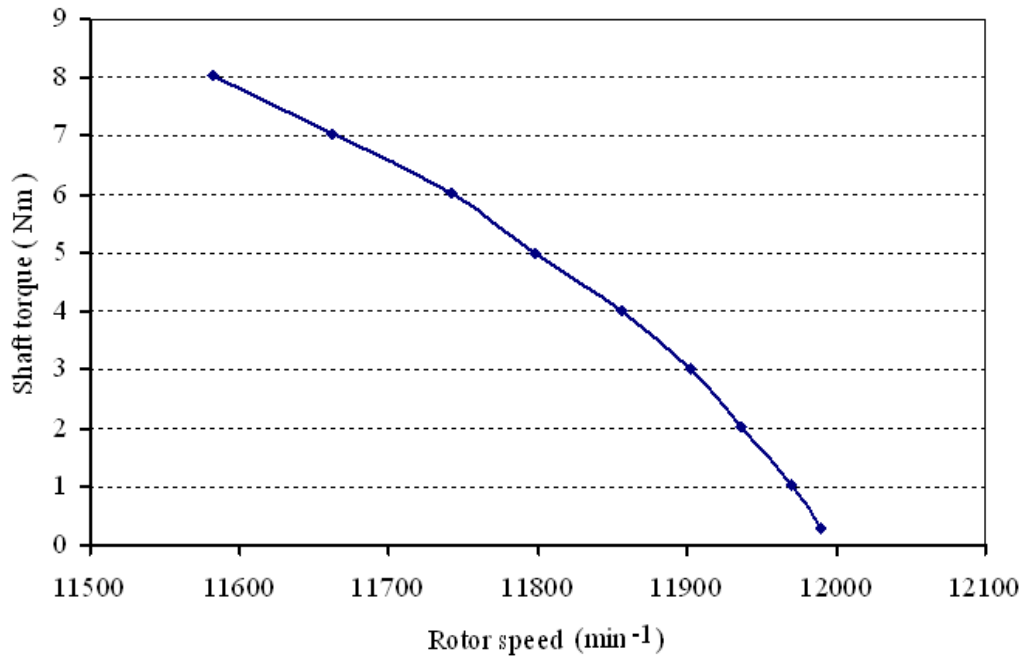


Figure 6.20: Measured mechanical characteristic of the 2-pole SRIM with Rotor B at the fundamental frequency $f_s = 200$ Hz, $n_{syn} = 12000$ /min, and line-to-line voltage $U_s = 165$ V.

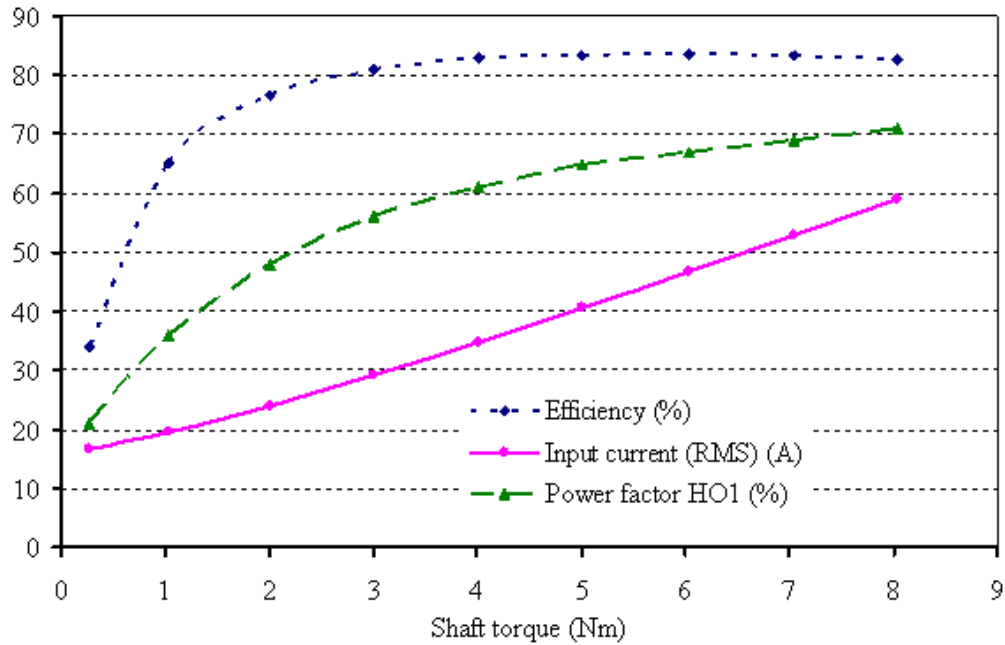


Figure 6.21: Measured output performance characteristics of a 2-pole SRIM at the fundamental line-to-line voltage $U_s = 165$ V, fundamental frequency $f_s = 200$ Hz, $n_{\text{syn}} = 12000$ /min.

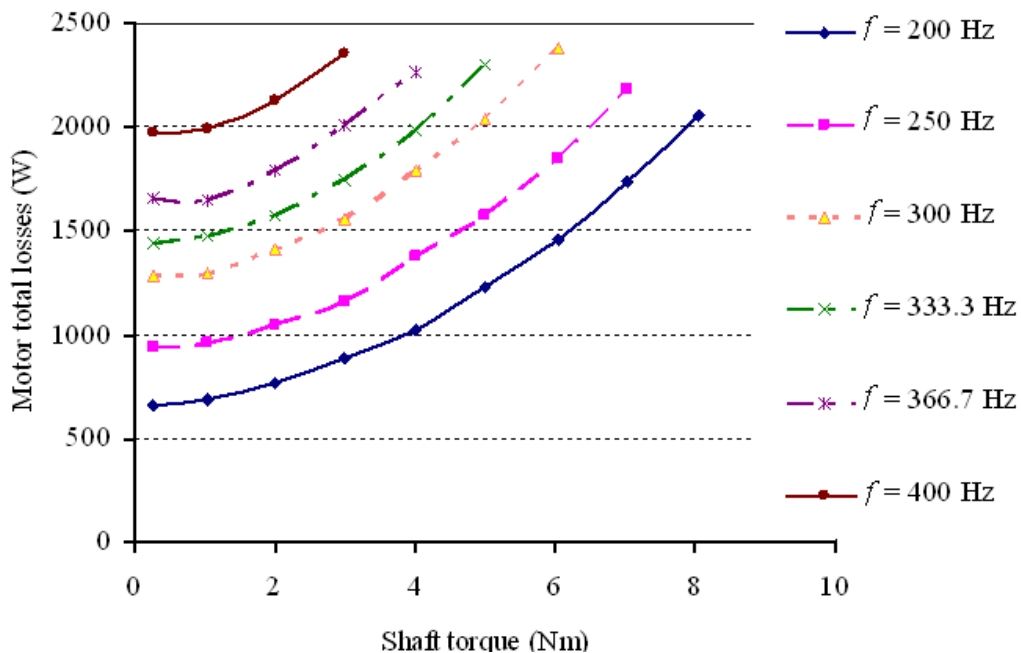


Figure 6.22: Measured total motor losses of the 2-pole SRIM with Rotor B at different operating fundamental frequencies.

Table 6.10: Load test results of the 2-pole SRIM with *Rotor B* at the fundamental frequency, $f_s = 250$ Hz, line-to-line voltage $U_s = 206$ V, Y

$\frac{M}{\text{Nm}}$	$\frac{n}{\text{min}^{-1}}$	$\frac{I_s}{\text{A}}$	$\frac{I_{s,\text{HO1}}}{\text{A}}$	$\frac{P_{\text{el, in}}}{\text{W}}$	$\frac{P_{\text{el, in, HO1}}}{\text{W}}$	$\frac{\cos \varphi_{\text{HO1}}}{-}$
0.3	14986	17.3	17.3	1467	1458	0.24
1.0	14961	19.9	19.9	2595	2587	0.37
2.0	14935	24.4	24.4	4202	4193	0.49
3.0	14891	29.4	29.4	5891	5882	0.57
4.0	14847	34.9	34.9	7619	7608	0.62
5.0	14800	40.7	40.6	9371	9355	0.65
6.0	14734	46.6	46.6	11136	11125	0.67
7.0	14654	52.8	52.7	12968	12958	0.69

Table 6.11: Measured temperature of different machine parts at the load test of the 2-pole SRIM with *Rotor B* at the fundamental frequency $f_s = 250$ Hz, line-to-line voltage $U_s = 206$ V Y for short time operation

$\frac{M}{\text{Nm}}$	$\frac{\vartheta_{\text{Cu, s}}}{^\circ\text{C}}$	$\frac{\vartheta_{\text{overhang}}}{^\circ\text{C}}$	$\frac{\vartheta_{\text{H}_2\text{O-in}}}{^\circ\text{C}}$	$\frac{\vartheta_{\text{H}_2\text{O-out}}}{^\circ\text{C}}$	$\frac{\vartheta_{\text{rotor}}}{^\circ\text{C}}$
0.3	29	29	22.0	22.1	40.8
1.0	35	36	22.9	23.1	55.5
2.0	42	43	23.7	24.0	66.0
3.0	45	47	24.5	24.9	75.2
4.0	56	57	26.0	26.7	93.6
5.0	61	62	26.6	27.4	101
6.0	68	69	27.1	27.9	110
7.0	73	74	27.8	28.8	125

Table 6.12: Measured output performance characteristics of the 2-pole SRIM with *Rotor B* at the fundamental frequency $f_s = 250$ Hz, line-to-line voltage $U_s = 206$ V Y

$\frac{M}{\text{Nm}}$	$\frac{s}{\%}$	$\frac{P_{m,\text{out}}}{\text{W}}$	$\frac{P_{\text{el},\text{in}}}{\text{W}}$	$\frac{P_{\text{el},\text{in.HO1}}}{\text{W}}$	$\frac{P_{d,\text{total}}}{\text{W}}$	$\frac{\eta}{\%}$
0.3	0.10	518	1467	1458	940	36
1.0	0.26	1629	2595	2587	957	63
2.0	0.43	3144	4202	4193	1049	75
3.0	0.73	4725	5891	5882	1157	80
4.0	1.02	6235	7619	7608	1373	82
5.0	1.33	7780	9371	9355	1574	83
6.0	1.77	9273	11136	11125	1852	83
7.0	2.31	10773	12968	12958	2185	83

6.5 Comparisons of Results

In this section, the measured performance characteristic results of the 4- and 2-pole solid rotor induction motors are compared in order to show the possible competitive industrial applications with other types of high speed motors. In addition, the measured and simulated results are compared in order to validate the 2D FE computations.

6.5.1 Comparisons of 4- and 2-pole Motors Test Results

Like the simulation results in Chapter 4, the 2-pole SRIM has less input current at the same torque and voltage because of less magnetizing current and is thereby operating with a higher power factor than of the 4-pole SRIM (Fig. 6.24) with the same *Rotor B*. The total losses, which are calculated from the difference of the input electrical and the output mechanical power, are smaller in the 2-pole machine. Hence it is operating with a higher efficiency (Fig. 6.25).

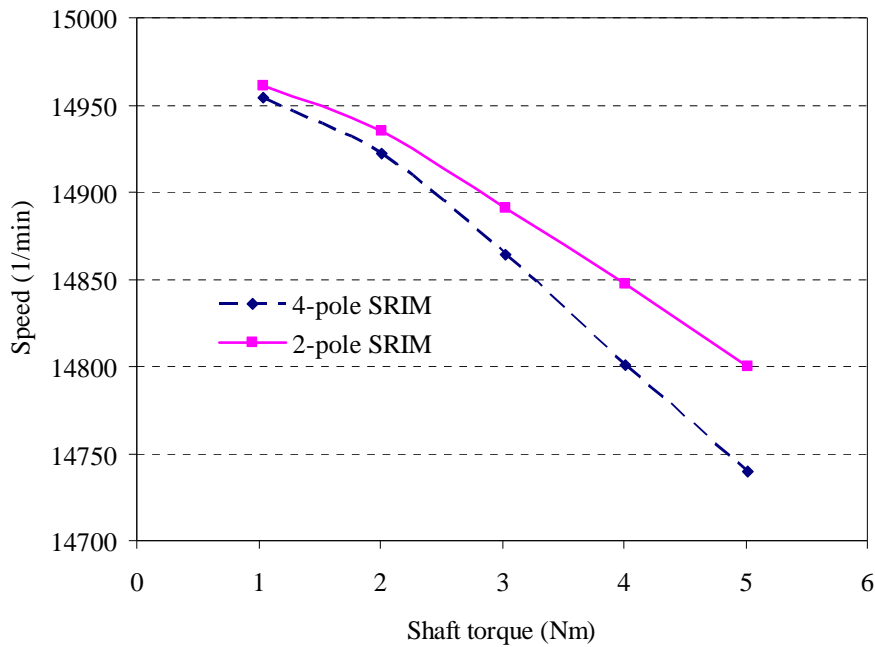
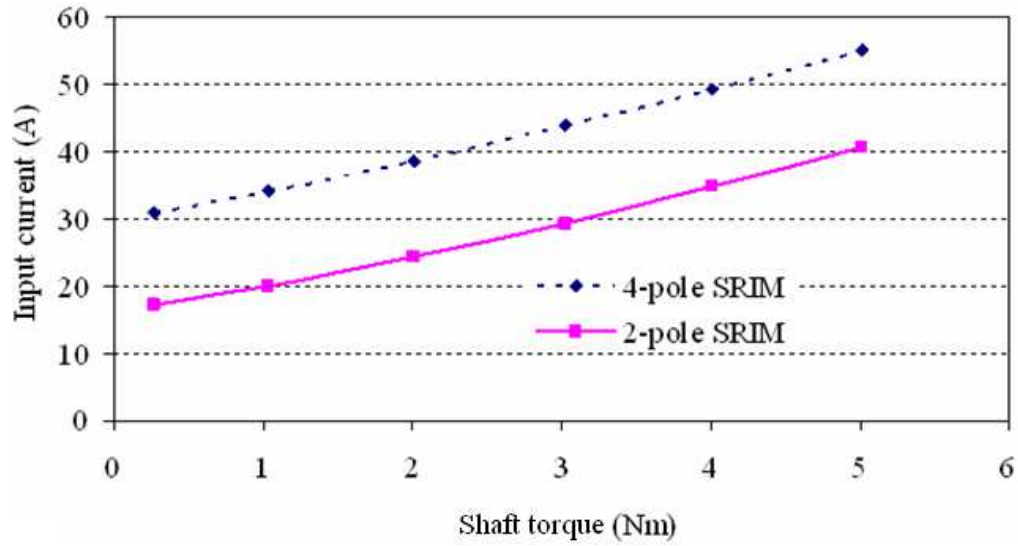
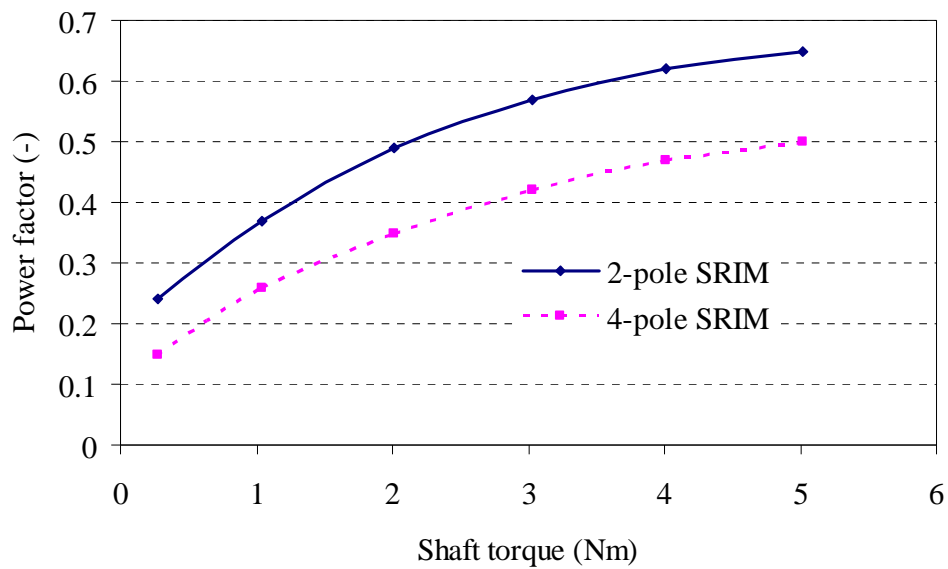


Figure 6.23: Measured mechanical characteristics of the 2-pole and 4-pole SRIM with *Rotor B* at a fundamental line-to-line voltage $U_s = 206 \text{ V Y}$ and $n_{\text{syn}} = 15000 \text{ min}^{-1}$.

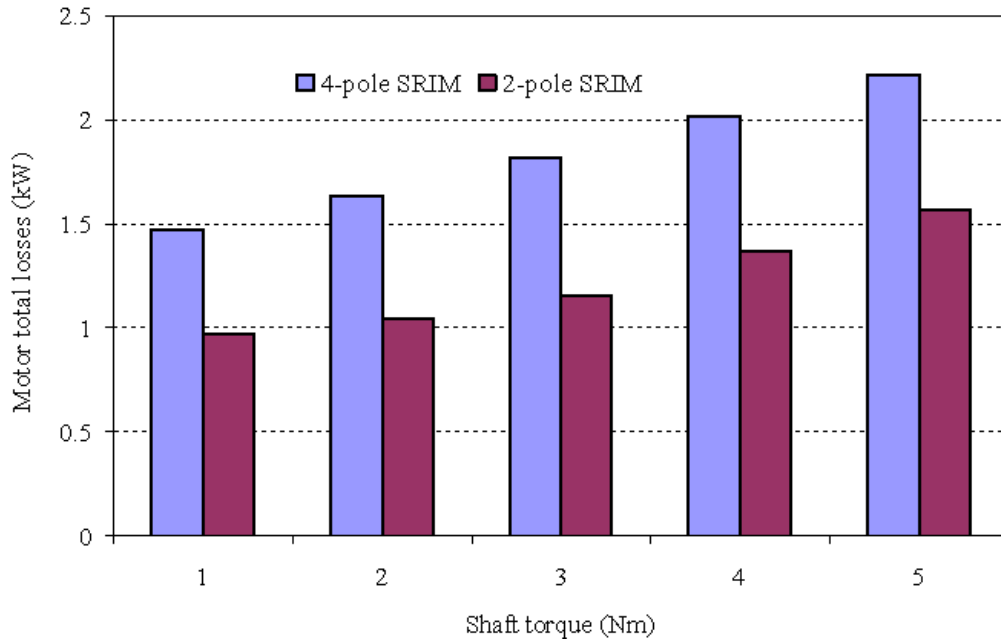


a)

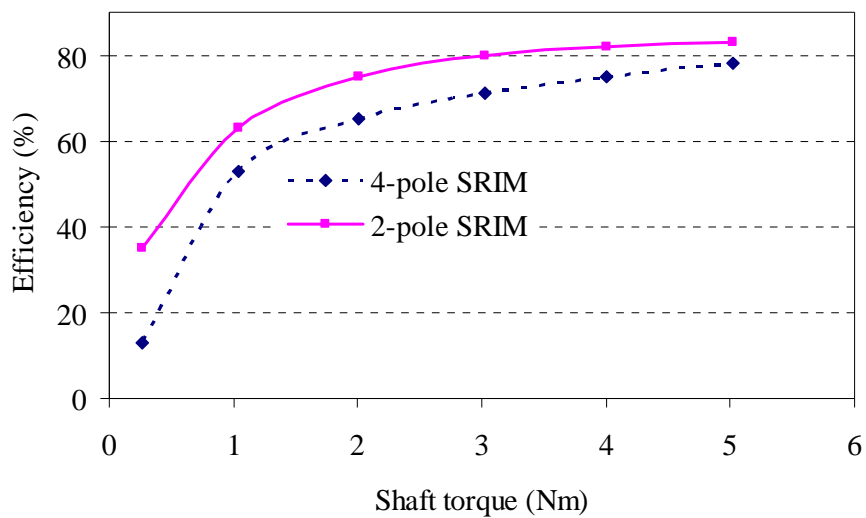


b)

Figure 6.24: Measured performance characteristics of the 2-pole and 4-pole SRIM with *Rotor B* at the fundamental line-to-line voltage $U_s = 206$ V, Y, and $n_{\text{syn}} = 15000$ min^{-1} : a) input current (RMS), b) fundamental power factor (HO1).



a)



b)

Figure 6.25: Measured performance characteristic of the 2-pole and 4-pole SRIM with *Rotor B* at the fundamental line-to-line voltage $U_s = 206$ V, Y, and $n_{\text{syn}} = 15000$ min⁻¹ a) motor total losses, b) shaft torque and efficiency.

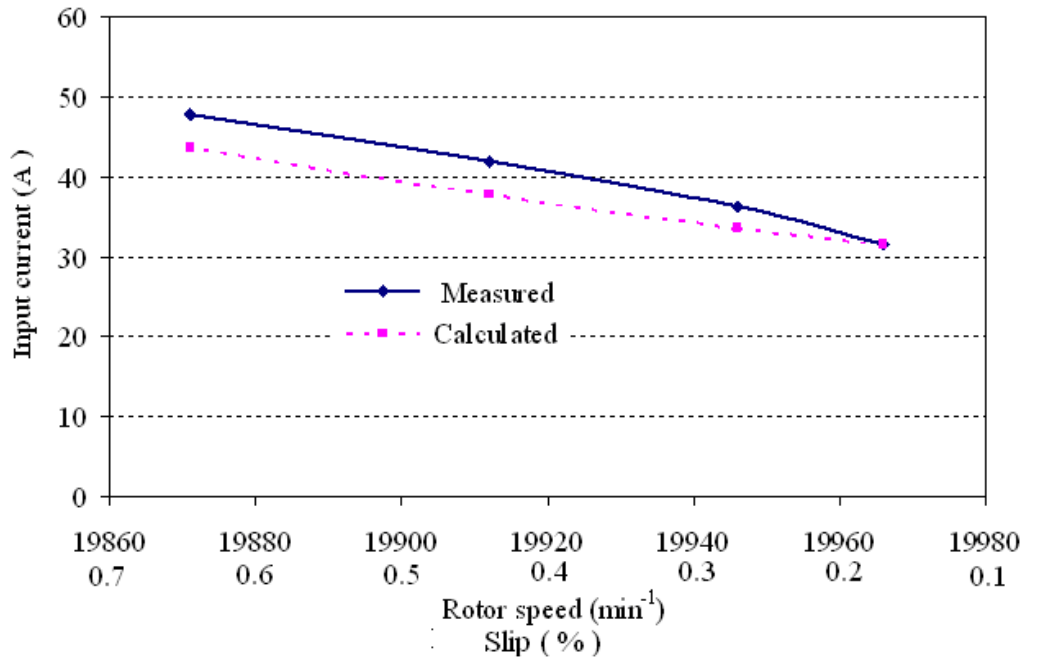
6.5.2 Comparison of Measured and Calculated Results

In this section, the comparison of the measured and 2D FEM simulated SRIM performance characteristics are presented. The main factor that complicates the comparison between the measured and numerically calculated results is the predetermined stator winding and rotor body temperature. Hence, the 4- and 2-poles SRIM are re-simulated using the actually measured stator winding and rotor temperatures. In addition to that, on the current simulation, a total end effect factor that considers the rotor end currents and the actual rotor end magnetic saturation condition is implemented. For axially slitted SRIM with copper end rings, the modified *Russell* end-effect factor given in (2.29) describes well the curved rotor current paths in the rotor ends by increasing the rotor resistivity, when the rotor is not heavily saturated. But it is investigated, that the rotor end region is the most saturated part of the rotor [30]. Hence, the end region of the solid rotor is causing a skin-effect to the rotor currents, which increases the apparent rotor resistance, when the slip increases. Thus, the effect of the operating slip must be considered by modifying the end-effect factor by a slip-dependent factor (k), given in (6.9) [1], [63].

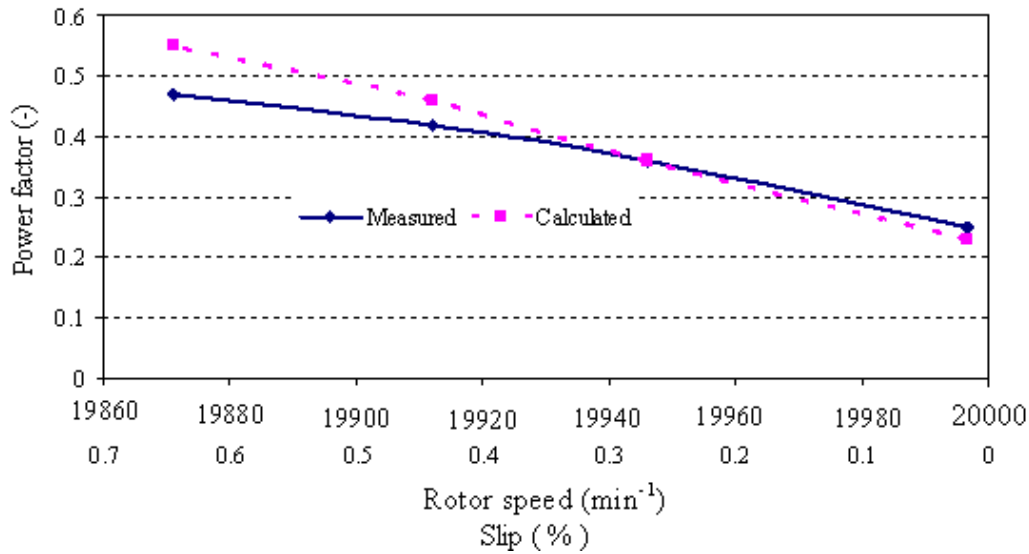
$$k = \left(\frac{n}{n_{\text{syn}}}\right)^4 \quad (6.9)$$

In (6.9) n and n_{syn} are the mechanical and synchronous rotating speed of the motors respectively. Therefore, the total end-effect factor k_{tot} , which takes into account the effect of increased slip, as the motor is loaded, is given in (6.10), as it is investigated in [1].

$$k_{\text{tot}} = k_{\text{R}} \cdot k \quad (6.10)$$



a)



b)

Figure 6.26: Measured and 2D time stepping FEM calculated characteristics of the 4-pole SRIM with *Rotor B* at the fundamental frequency $f_s = 666.7$ Hz, line-to-line voltage $U_s = 255$ V sinusoidal voltage supply a) input current and b) operating power factor.

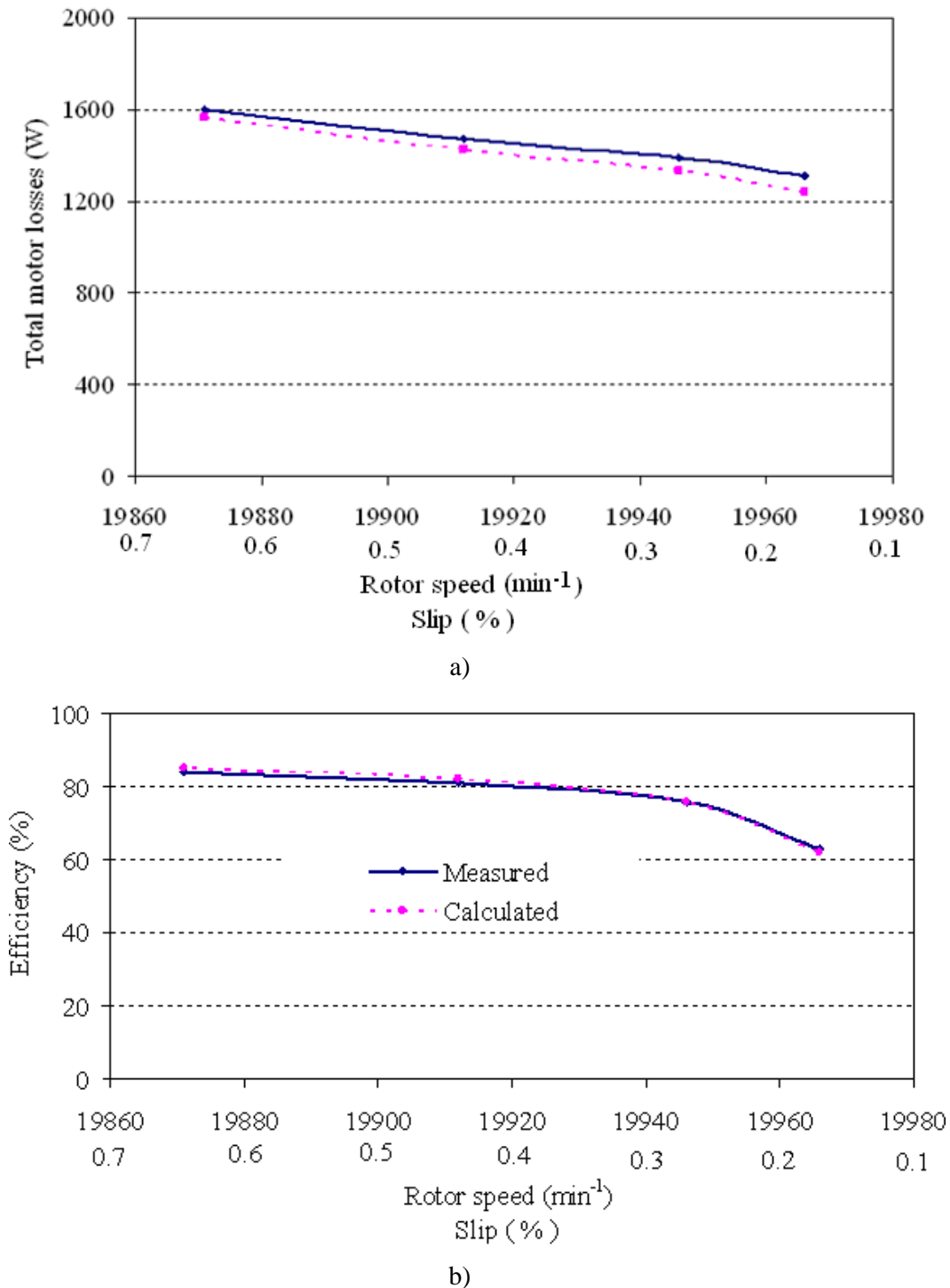


Figure 6.27: Measured and 2D time stepping FEM calculated characteristics of the 4-pole SRIM with *Rotor B* at the fundamental frequency $f_s = 666.7$ Hz, line-to-line voltage $U_s = 255$ V, sinusoidal voltage supply a) motor losses and b) operating efficiency.

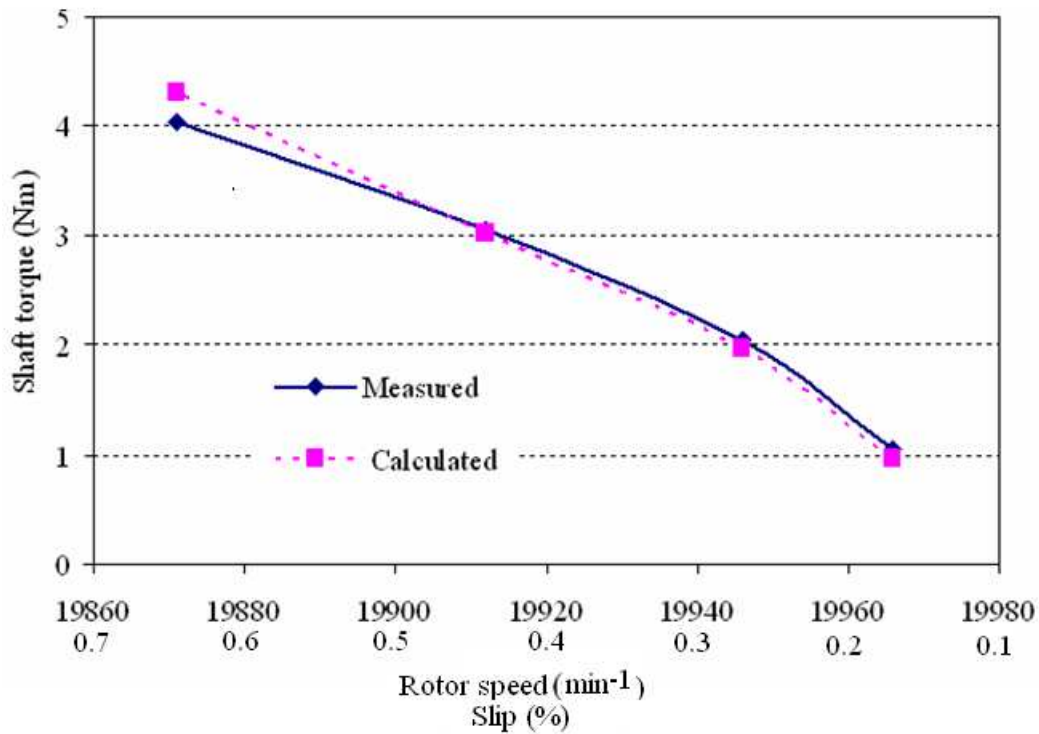


Figure 6.28: Measured and 2D time stepping FEM calculated mechanical characteristics of the 4-pole SRIM with *Rotor B* at the fundamental frequency $f_s = 666.7$ Hz, line-to-line voltage $U_s = 255$ V sinusoidal voltage supply

In (6.10) k_R the *Russell* end-effect factor, which is given in (2.29). Using the aforementioned correcting measures, the measured and simulated result comparisons are presented on the figures Fig. 6.26 ÷ Fig. 6.28. With the introduction of the slip dependent end-effect factor and considering the actual stator winding and rotor temperatures, the measured and simulated results are in concordance for the low slip operating region, which is basically the nominal working region of high speed solid rotor induction motors.

7 Conclusions and Recommendations

The FEM and experimental analysis show that the solid rotor induction motor constructed with *Rotor B* with radial grooves, higher air-gap distance and deep rotor slits has less rotor losses and thereby can be operated at higher efficiency than with *Rotor A*. But the input current with *Rotor B* is higher than with *Rotor A*, because the magnetizing current, caused by the relatively higher radial air-gap distance is bigger. Accordingly the power factor of the machine with *Rotor B* is lower than with *Rotor A*. For short-time operation $S2-10$ min the temperature of *Rotor A* increases up to $200\text{ }^{\circ}\text{C}$, whereas on *Rotor B* the increase is only $120\text{ }^{\circ}\text{C}$, which can be already dangerous for the implemented high-speed mechanical bearings. Thus, it is necessary to build such SRIM for increased speeds with magnetic bearings or implement a special direct rotor cooling construction.

For high speed solid rotor induction motors the supply frequency is so high that the choice of the pole numbers has to be made between two and four poles. A lower stator frequency and hence lower stator core and rotor losses are obtained in a 2-pole machine. However, the increased height of the stator yoke of the two-pole machine leads to a bigger machine and to higher stator copper losses due to the longer winding overhangs. Hence a $2/3$ -pitching of the stator coils is recommended.

The torque/volume density, obtained at the same calculated steady-state temperature rise of 85 K in the stator winding and at 24000 min^{-1} , is by 30 % bigger for 2-pole than the 4-pole solid rotor induction motor. The torque/volume density of the permanent magnet synchronous motor at 24000 min^{-1} and 80 K temperature rise is by 25 % bigger than for the 2-pole SRIM of the same geometry. The rotor temperature of the SRIM with *Rotor B* increases up to $240\text{ }^{\circ}\text{C}$ steady-state, which is much bigger than in the PMSM ($93\text{ }^{\circ}\text{C}$ steady-state), which may endanger the bearing life. But the high speed rotor may be used for increased speed, when operated with magnetic bearings.

The performance characteristic comparisons at the rated condition between the possible high speed machines show that the PMSM has the best performance characteristics at nominal operation. It has an efficiency of 94.6 % and operates at a power factor of $\cos\varphi = 0.95$ (HO1). The lowest performance result is shown by the 4-pole SRIM with *Rotor B* with an operating efficiency of 89.8 % and a power factor $\cos\varphi = 0.69$. On the other hand the 2-pole SRIM with *Rotor B* has an efficiency of 91.9 % and a $\cos\varphi = 0.84$, which shows its competitiveness for the elevated high speed applications, as a long as the rotor cooling challenge is solved.

The measured and 2D time stepping FEM computed performance parameters of the SRIM, i.e. shaft torque, efficiency and power factor, are in good agreement with allowable accuracy, especially at the low slip operating region. The rotor end currents and its 3D geometrical features are taken into consideration in the 2D FEM simulation by an equivalent end-effect factor. The current ripple, caused by the PWM voltage supply, is well damped by designing and implementing a low pass LC sinus filter. This also allows the comparison of the measured values with the simulated results, which were obtained using the 2D time stepping FEM at sinusoidal voltage supply.

Appendix A

Stator Frame and Stator Core Detail

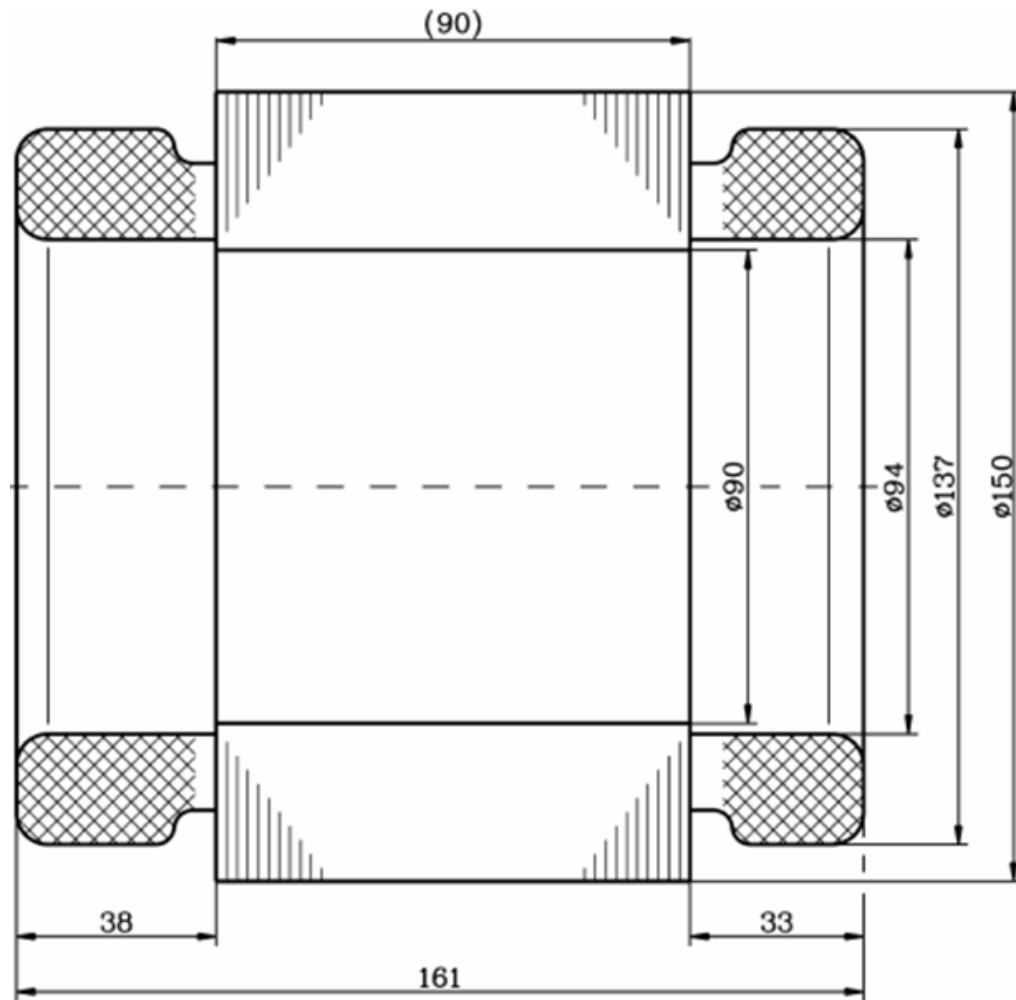


Figure A.1: Stator core with the winding for the 4-pole SRIM

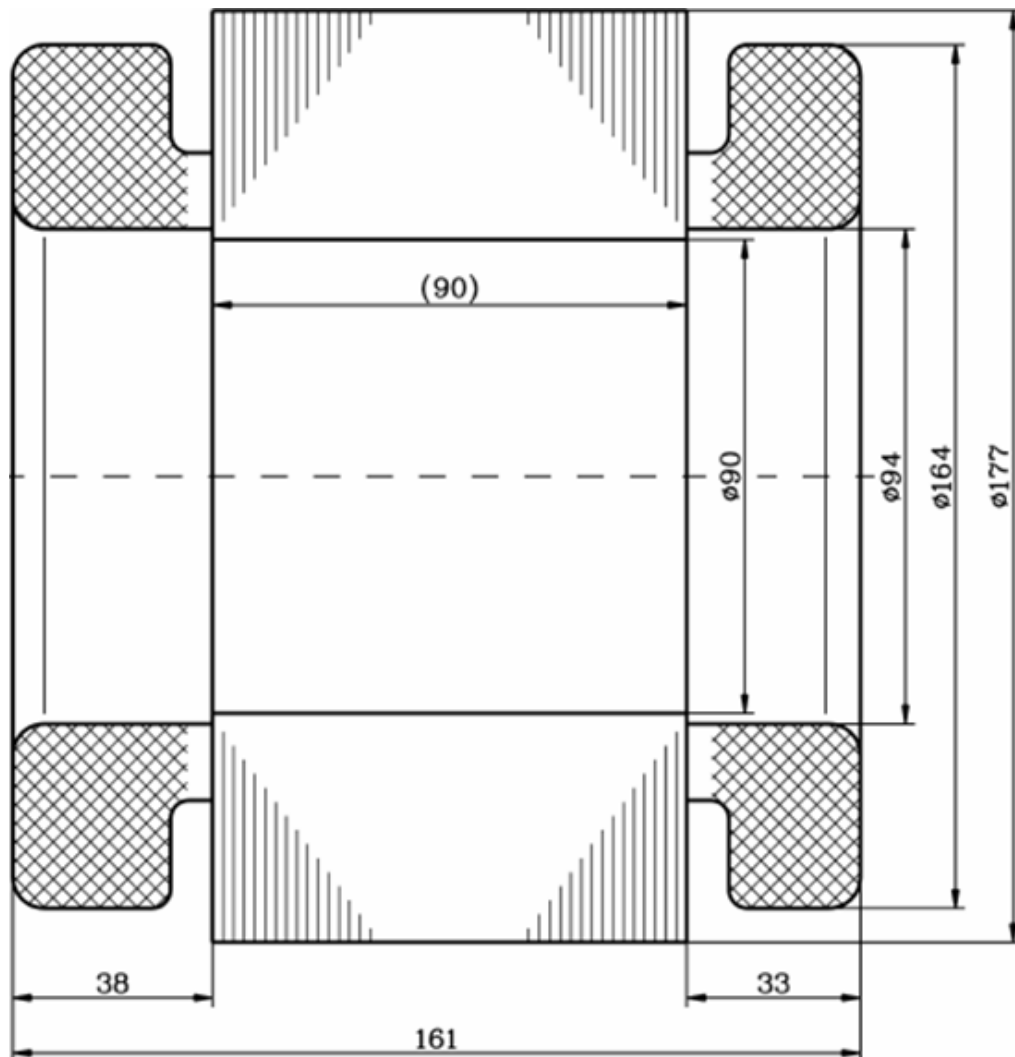


Figure A.2: Stator core with the winding for the 2-pole SRIM

Appendix B

Rotor Constructions

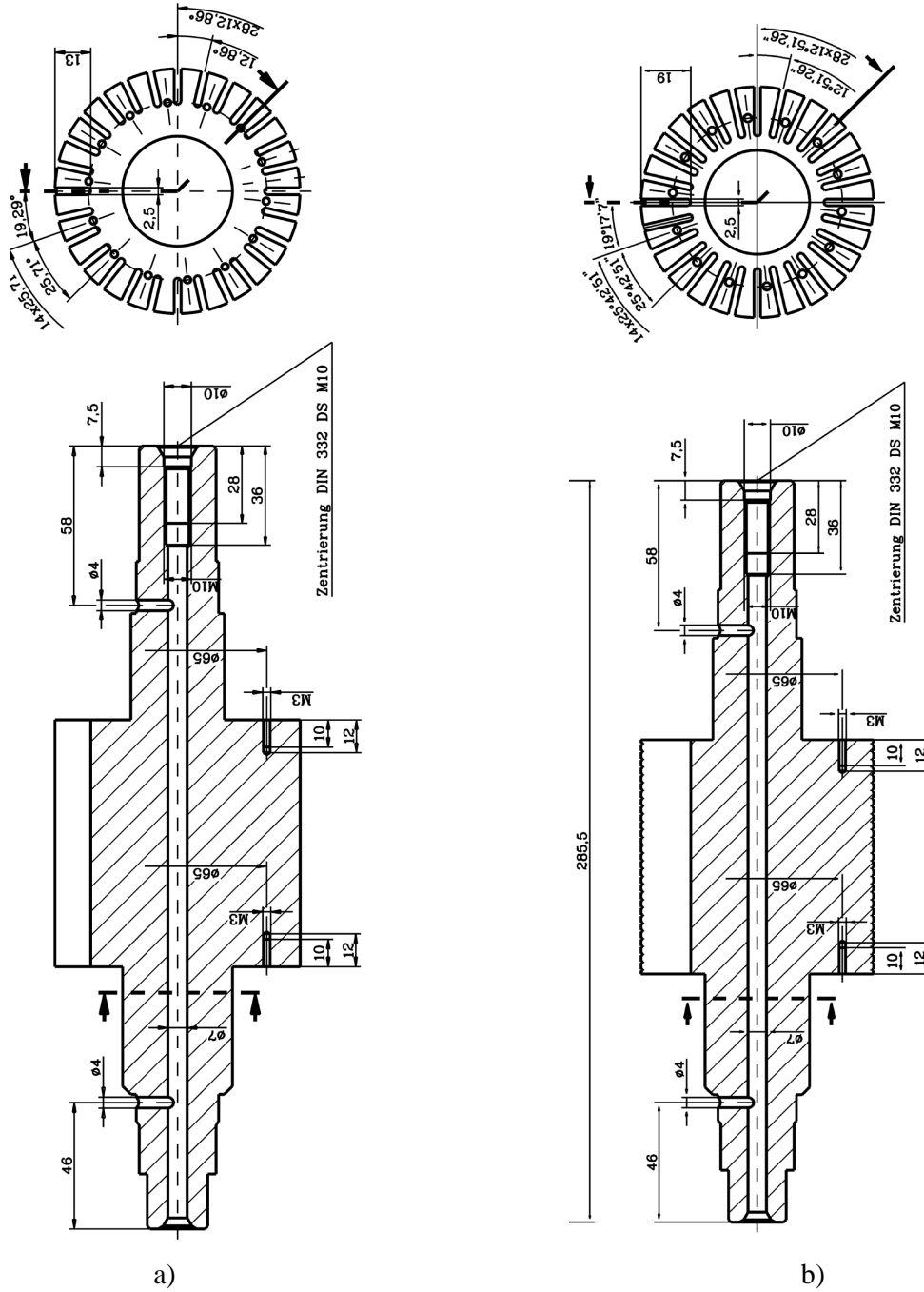


Figure B.1: Constructional detail of the rotors: a) Rotor A, and B) Rotor B

Appendix C

Implemented Torque Sensor

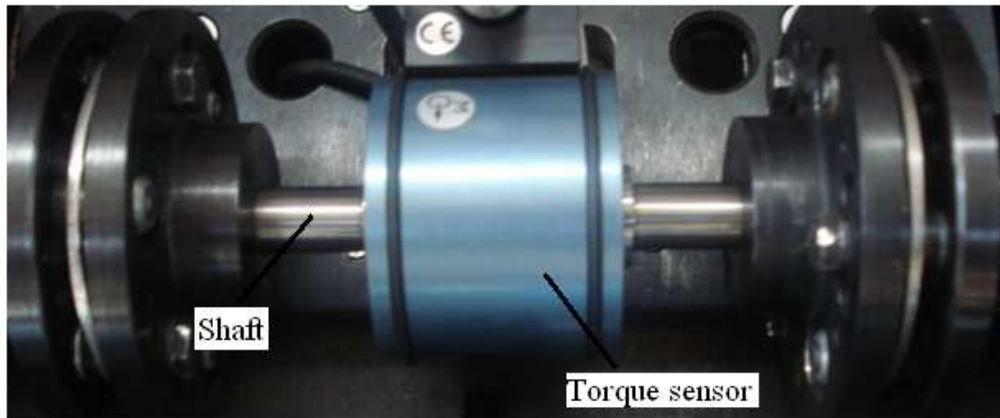
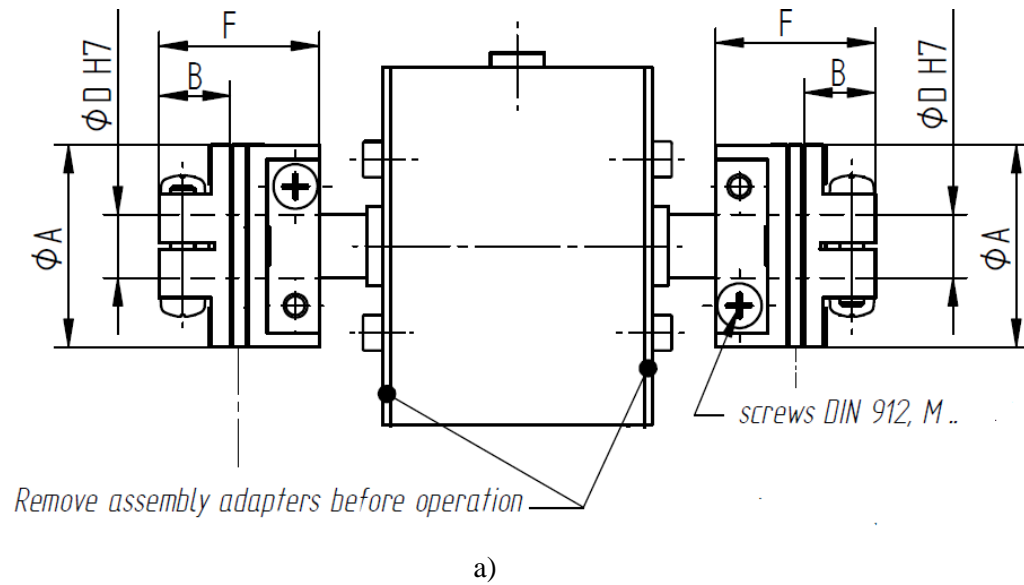


Figure C.1: Implemented *Lorenz* torque sensor: a) geometrical dimensions (see Table C.1), and b) view of the mounted device at the test bench.

The torque sensor from *Lorenz Messtechnik GmbH* is implemented to measure the torque M and the rotor speed (n). From the product of these quantities, the shaft power output (P) is calculated as in (C.1).

$$P = 2\pi n \cdot M \quad (C.1)$$

The torque sensor consists of the stator and the rotating part. The bearingless design of the torque sensor is the advantage, having less preventive maintenance and no lubrication work necessary. Measuring signal distortion caused by friction losses, dusts and heating effects can be occurring. The main technical data of the given torque sensor is listed in Table C.1. The maximum axial allowable misalignment is 0.8 mm. The accuracy of the torque sensor is high (0.1 %) with the rated voltage 12...28 V DC and output signal $\pm 0...5$ V. The speed sensor is characterized with a maximum frequency 6 kHz and an output signal 5V TTL.

Table C.1 Technical data of the implemented torque sensor

Measuring range (Nm)	Size	Max. Speed (min ⁻¹)	Dimensions (mm)						
			ϕA	B	ϕD	F	L _A	M	M _A (Nm)
20	62	30000	57.4	16.1	13	36.6	130.8	M5	6.1

The two-channel digital display is a versatile measuring device which was used to display the measured parameters (Fig. C.2). The measuring device with its rigid housing has been well proven in application to display the measuring torque and rotating speed. The device is either being programmed by a personal computer or by 5 keys directly. Additional functions such as Min.-Max, memory, tare, delete buffer, can be carried out by the keys or two programmable inputs.



Figure C.2: Two channel measuring parameters displaying device for the torque sensor (in front).

REFERENCES

- [1] Aho, T.: *Electromagnetic design of a solid steel rotor motor for demanding operation environments*, PhD thesis, Lappeenranta University of Technology, Finland, 2007.
- [2] Ahrens, M.; Bikle, U.; Gottkehaskamp, R.; Prenner, H.: *Electrical Design of high Speed Induction Motors of up to 15MW and 20000 rpm*, Power Electronics, Machines and Drives Conference, Bath, 16-18 April 2002, Publication No. 487, p. 381-386.
- [3] Al-Zahawi, B.A.T.; James, B.P.; and Starr, F.: *High speed turboalternator for domestic combined heat and power unit*. Proceedings of the 8th Int. Conf. on Electric Machines and Drives, Cambridge, UK, September 1997, p. 215-218.
- [4] Andresen, E.; Racinowski, B.; Szymanski, G.: *Numerical Simulation of High Speed Induction Machine with Solid Rotor*, ISEF'95, Thessaloniki, Greece, p. 183-187.
- [5] Angst, G.: *Polyphase Induction Motor with solid rotor; Effects of saturation and finite length*, IEEE Transactions on Power Apparatus and Systems, vol. PAS-81, 1962, p. 902-909.
- [6] Ansys user's manual: *ANSYS Classic in Version 11*, Jan. 2007, Canonsburg, USA
- [7] Arkkio, A.: *Analysis of induction motors based on the numerical solution of the magnetic field and circuit equations*, PhD Thesis, Helsinki University of Technology, Finland, 1987.
- [8] Arkkio, A.; Jokinen, T.; Lantto, E.: *Induction and Permanent Magnet Synchronous Machines for High-Speed Applications*, 8th Int. Con. on Electr. Machines and Systems, 27-29 Sept. 2005, Nanjing, China, 6 pages, CD-ROM.
- [9] Bertotti, G.: *General Properties of Power Losses in Soft Ferromagnetic Materials*, IEEE Trans. Magnetics, Vol.24, No.1, p. 621-630, 1988.
- [10] Binder, A.; Schneider, T.; Klohr, M.: *Fixation of buried and surface mounted magnets in high-speed synchronous machines*, IEEE Trans. on Ind. Appl. 2006, Vol. 42, no. 4, p. 1031-1037.

- [11] Binder, A.: *Analytical calculation of eddy current losses in massive rotor parts of high-speed permanent magnet machines*, Proc. of the International Symposium on Power Electronics, Electrical Drives, Automation and Motion, SPEEDAM, 13-16 June 2000, Ischia, Italy, 2000, p. C2-1 – C2-6.
- [12] Binder, A.; Schneider T.: *High-Speed Inverter-Fed AC Drives*, International Aegean Conference on Electrical Machines and Power Electronics, Electromotion 2007, Bodrum, Turkey, Sept. 10-12, 2007, p. 9-16.
- [13] Cedrat: *Users guide of FLUX-2DTM*, (version 9.10) finite element program, 2006, Meylan, France.
- [14] Chalmers, B.J.; Wooley, I.: *General Theory of Solid-Rotor Inductions Machines*. Proc. IEE, Vol.119, No. 9: p. 7-14, 1972.
- [15] Christoph, C.: *Zur Theorie der Drehstrom-Asynchronmaschine mit massivem Läufer*, ETZ-Archiv, 87: p. 137-144, 1966.
- [16] Cogent: *Electrical Steel*, Data Sheet Elektrobleche, Newport, UK, 2002.
- [17] Dorairaj, K.R.; Krishnamurthy, M.R.: *Polyphase Induction Machine with a slitted Ferromagnetic Rotor: I- Experimental Investigations and a novel Slipmeter*, IEEE Transactions on Power Apparatus and Systems, vol. PAS-86, No.7 July 1967, p. 835-843.
- [18] Dorairaj, K.R.; Krishnamurthy, M.R.: *Polyphase Induction Machine with a slitted Ferromagnetic Rotor: II- Analysis*, IEEE Transactions on Power Apparatus and Systems, vol. PAS-86, No.7 July 1967, p 844-855.
- [19] Eckhardt, H. : *Numerische Verfahren in der Energietechnik*. Teubner Studienskripten, Stuttgart 1978
- [20] Ertan, H.B.; Leblebicioglu, K; Avenglu B.; Pirgaip M.: *High-frequency loss calculation in a smooth rotor induction motor using FEM*, IEEE Transactions on Energy Conversion, Vol.22, no.3 September 2007, p. 566-575.
- [21] Finlayson, P. T.: *Output filters for PWM drives with induction motors*, IEEE, Industry Applications Magazine, Vol. 4, no. 1, Jan. /Feb. 1998, p.46-52.
- [22] Glidcop: North American Höganäs, <http://www.hoganas.com/en/Products-Applications/GLIDCOP/>

- [23] Gottkehaskamp, R.: *Nichtlineare Berechnung von Asynchronmaschinen mit massiveisernem Rotor und zusätzlichem Käfig im transienten Zustand mittels Finiter Differenzen und Zeitschrittrechnung*, Phd thesis, VDI-Fortschritts-Berichte, Reihe 21: Elektrotechnik, Nr.131, 1993.
- [24] Greifenstein, E.: *Entwurf, Konstruktion und experimentelle Untersuchungen von hochtourigen Drehstrommaschinen mit Käfigläufer und mit Permanentmagnetläufer*, Dissertation TU Darmstadt, Shaker Verlag, 2000.
- [25] Huppunen, J.: *High-speed solid-rotor induction machine - electromagnetic calculation and design*, PhD thesis, Lappeenranta University of Technology, Finland, 2004.
- [26] Hütte (Hrsg.: W. Böning unter Mitarbeit von E. Alwers u.a.): *Elektrische Energietechnik*, Band 1: Maschinen, 29. Auflage, Springer-Verlag, Berlin, 1978.
- [27] IEC60034-1: *Rotating electrical machines- Part I, Ratings and performance*, Geneva, Switzerland, 2004.
- [28] Ikeda, M.; Sakabe, S.; Higashi, K.: *Experimental study of high speed induction motors varying rotor core construction*. IEEE Trans. on Energy Conversion, Vol. 5, No.1, 1990, p. 98-103.
- [29] ISO 1940/1: *Balance Quality Requirements of Rigid Rotors*, International Organization for Standardization, Mar. 2009, Louisville USA.
- [30] Jokinen, T.; Arkkio, A.: *High-Speed AC motors*, Proc. of the International Symposium on Power Electronics, Electrical Drives, Automation and Motion, SPEEDAM, Capri, Italy, p. B5-9-B5-14, June 1996.
- [31] Jordan, H.; Taegen, F.: *Über das Strom- und Drehmomentverhalten von Drehstromasynchronmotoren mit massiven Eisenläufern*, E u. M 80 (1963) p.326-334.
- [32] Lateb, R.; Enon, J.; Durantay L.: *High Speed, High Power Induction Motor Technologies for Integrated Compressors*, 12th Int. Con. On Electr. Machines and Systems, 15-18 November 2009, Tokyo, Japan, 5 pages, CD-ROM.
- [33] Lu, T.: *Weiterentwicklung von hochtourigen permanenterregten Drehstromantrieben mit Hilfe von Finite-Element-Berechnungen und experimentellen Untersuchungen*, Dissertation TU Darmstadt, Shaker Verlag, 2004.

- [34] Lähteenmäki, J.: *Design and Voltage Supply of high-speed Induction machines*, PhD Thesis, Helsinki University of Technology, Finland, 1991.
- [35] Mc Connel, H.; Sverdrup, E.: *The induction machine with solid rotor iron*, AIEE Trans. on Power Apparatus and Systems, Vol. PAS-74, 1955, p. 343-349.
- [36] Mekhiche, M. ; Kirtley, J.L. ; Tolikas, M. ; Ognibene, E. ; Kiley, J. ; Holmanský, E. ; Nimblett, F. : *High speed motor drive development for industrial applications*, in Int. Electric Machines Drives Conf., (IEMDC), Seattle, WA, May 1999, pp.244-248.
- [37] Pasquarella, G.: *Über die Entwicklung einer schnelllaufenden Asynchronmaschine für magnetgelagerte Hochgeschwindigkeits-Antriebe erhöhter Leistung*, PhD thesis, ETH Zürich, No.10452, Switzerland, 1993.
- [38] Peesel, H.: *Über das Verhalten eines Asynchronmotors bei verschiedenen Läufern aus massivem Stahl*. Dissertation Technische Hochschule Braunschweig, 1958.
- [39] Preston, T. W.; Reece, A.B.J.; Sangha P. S.: *Induction motor analysis by time stepping techniques*, IEEE Transactions on Magnetics, Vol. 24, no. 1, 1988, p. 471-474.
- [40] Pyrhönen, J.; Jokinen T.; Hrabovcova V.: *Design of Rotating Electrical machines*, John Wiley & Sons Ltd, 2008, Chichester, UK.
- [41] Pyrhönen, J.: *The high-speed induction motor: Calculating the effects of solid-rotor material on machine characteristics*, PhD Thesis, Lappeenranta University of Technology, Finland, 1991.
- [42] Pyrhönen, J.; Nerg, J.; Kuronen, P.; Lauber, U.: *High-speed 8 MW solid-rotor induction motor for gas compression*, 18th Int. Conf. on Electr. Machines IECM'08, Vilamoura, Portugal, Sept. 6-9, 2008, 6 pages, CD-ROM
- [43] Rajagopalan, P.K.; Balarama M.V.: *Effects of axial slits on the performance of inductions machines with solid rotors*. IEEE Trans. on Power Apparatus and Systems, Vol. PAS 88. 1969, p. 1695-1709.
- [44] Richter, R.: *Elektrische Maschinen, Band IV: Die Induktionsmaschinen*. Birkhäuser, Basel, 1954.
- [45] Russell, R. L.; Norsworthy, K.H.: *Eddy current and wall losses in screened rotor induction motors*, Proc. of IEE, Vol.105A, no. 20, April 1958, p.163-173.

- [46] Sadowski, N.; Lefevre, Y.; Lajoie-Mazenc, M.; Cros, J.: *Finite element torque calculation in electrical machines while considering the movement*, IEEE Transactions on Magnetics, Vol. 28, No.2, March 1992, p.1410-1413.
- [47] Saari, J.: *Thermal Analysis of high-speed Induction machines*, PhD Thesis, Helsinki University of Technology, Finland, 1998.
- [48] Saari, J.; Arkkio A.: *Losses in high-speed asynchronous motors*, 10th Int. Conf. on Electr. Machines ICEM'94, Paris, France, p. 704-708.
- [49] Salon, S. J.: *Finite Element Analysis of Electrical Machines*, Kluwer Academic Publishers, Norwell, Massachusetts, 1995
- [50] Sarma, M. S.: *Electromagnetic fields in solid-rotor induction motors*, IEEE Tras. Aerosp. Electron. Syst. AES-12, Vol.5, p. 572-576, September 1976.
- [51] Simodrive 611U: *User's manual*, <http://www.automation.siemens.com>, Siemens AG, Berlin / Munich, March 2006.
- [52] SKF: *SKF Genauigkeitslager*, Katalog 3700/IT, Schweinfurt, 1987.
- [53] Soong, W. L.; Kliman, G. B.; Johnson, R.N.; White, R. A.; Miller, J. E.: *Novel High-Speed Induction Motor for a Commercial Centrifugal Compressor*, IEEE Trans. on Ind. Appl., Vol. 36, no.3, May/June 2000, p. 706 – 713.
- [54] Sozer, Y.; Torrey D. A.; Reva, S.: *New inverter output filter topology for PWM motor drives*, IEEE Trans. on Power Electronics, Vol. 15, no. 6, Nov. 2000, p. 1007-1017.
- [55] Toliyat, H. A.; Kliman, G.B.: *Handbook of Electric Motors*, Marcel Dekker Inc. 30. April 2004, Boca Raton, USA.
- [56] Tärnhuvud, T.; Reichert, K.: *Accuracy problems of force and torque calculations in FE-Systems*, IEEE Transactions on Magnetics, Vol. 24, No.1, January 1988, p. 443- 446.
- [57] Vacuumschmelze GmbH: *Weichmagnetische Werkstoffe*, 4. Auflage Verlag Siemens AG, Berlin/ München 1990.
- [58] Vogt, K.: *Berechnung elektrischer Maschinen*, VCH Verlagsgesellschaft, Weinheim, 1996.
- [59] Wilson, J.C.: *Theory of Solid Rotor Induction Machine*. Dissertation. University of Colorado, 1969.

- [60] Wood, A.; Concordia, C.: *An Analysis of solid rotor machines: Part I, Operational impedance and equivalent circuits*. AIEE Trans. on Power Apparatus and Systems, Vol. PAS 78, 1960, p.1657-1665.
- [61] Wood, A.; Concordia, C.: *An Analysis of solid rotor machines: Part II, The effects of curvature*, AIEE Trans. on Power Apparatus and Systems, Vol. PAS 78, 1960, p.1666-1672.
- [62] Yamazaki, K.: *Induction Motor Analysis Considering both Harmonics and End Effects using Combination of 2D and 3D Finite Element Method*, IEEE Transactions on Energy Conversion, Vol. 14, No. 3, September 1999, p.698-703.
- [63] Yee, H.; Wilson, T.: *Saturation and finite length effects in solid rotor induction machines*, Proc. IEE, Vol.119, No.7, 1972, p. 877-882.
- [64] Zaim, M.E.: *Non-linear models for the design of solid rotor induction machines*, IEEE Transaction on Magnetics, Vol.35, No.3, 1999, p. 1310-1313.

Publications in international conference proceedings during this project work:

- [65] Gessese, Y.; Binder, A.: *Axially slitted, High-Speed, Solid-Rotor Induction Motor Technology with Copper End-Rings*, Proc. of 12th Int. Conf. on Electr. Machines and Systems, (ICEMS) 15-18 November 2009, Tokyo, Japan, 6 pages, CD-ROM.
- [66] Gessese, Y.; Binder, A.: *Design and analysis of specific high speed solid rotor induction motor with copper end rings*, Proc. of the 14th IEEE Conference on Electromagnetic Field Computation, CEFC, 9-12 May 2010, Chicago IL, USA, 1 page, CD-ROM.
- [67] Gessese, Y.; Binder, A.; Funieru, B.: *Analysis of the effect of radial rotor surface grooves on motor losses of high speed solid rotor induction motor*, Proc. of the International Symposium on Power Electronics, Electrical Drives, Automation and Motion, SPEEDAM, 14-16 June 2010, Pisa, Italy, p.1762-1767.

Curriculum Vitae

Personal Information:

Name Yoseph Gessese Mekuria
Date & Place of Birth 3rd April 1970, in Addis Ababa, Ethiopia

Education:

09.1986 - 09.1988 General Wingate Technical and Vocational School,
Addis Ababa, Ethiopia
09.1988 - 06.1990 College Diploma in Electrical Technology
Addis Ababa University, Addis Ababa, Ethiopia
09.1990 - 06.1996 Diploma (Master of Science), Electrical Engineering,
Specialised in Electrical Machines, Odessa State Polytechnic
University, Odessa, Ukraine
11.2006 - 03.2011 PhD study at the Institute for Electrical Energy Conversion,
Darmstadt University of Technology, Darmstadt, Germany

Trainings:

06.2000 - 07.2000 Curriculum development for Technical Instructors, GTZ and
Adama University, Adama, Ethiopia
03.2002- 07.2002 German Language Course, Carl-Duisburg Centre,
Groß-Gerau, Germany
04.2002- 04.2003 Advanced Professional Training in Electrical Control
Systems, *Inwent* Capacity Building International,
Groß-Gerau, Germany

Work Experience:

09.1996- 08.2006 Lecturer, Electrical Machines and Drives, Adama University,
Adama, Ethiopia.
Since 04. 2011 Development Engineer at AREVA Wind GmbH
Bremerhaven, Germany